Title
Room Temperature Gas Sensing using Graphene FET

Author
Liu, Yumeng

Publication Date
2017

Peer reviewed|Thesis/dissertation

Room Temperature Gas Sensing using Graphene FET

by

Yumeng Liu

A dissertation submitted in partial satisfaction of the
requirements for the degree of
Doctor of Philosophy

in

Engineering – Mechanical Engineering

in the

GRADUATE DIVISION

of the

UNIVERSITY OF CALIFORNIA, BERKELEY

Committee in charge:

Professor Liwei Lin
Professor Costas Grigoropoulos
Professor Ana Arias

Fall 2017

Abstract

Room Temperature Gas Sensing Using Graphene FET
by
Yumeng Liu
Doctor of Philosophy in Mechanical Engineering
University of California, Berkeley
Professor Liwei Lin, Chair

In the modern age of gas sensing technologies for broad applications such as internet of things, the capability to make selective, small form factor, and highly responsive sensors for applications such as wearable devices and cell phones could revolutionize the fields of gas sensing systems and fabrications. This thesis aims at developing a millimeter-sized and microwatt-powered sensor prototype using graphene field effect transistors (FETs) by exploring various DC and AC modulation techniques to realize the critical gas sensing features of selectivity and fast recovery speed at room temperature for practical applications.

For the DC modulation, we applied the DC gate voltage on the graphene FET during the gas sensing events, and developed the concept of linear factor and the bandwidth enhanced noise method for improving graphene gas sensing performance at DC conditions. Specifically, we have experimentally demonstrated the label-free gas selectivity directly using a single graphene FET for NO_2, NH_3, H_2O and CH_3OH by measuring the linear factor parameter. Furthermore, we demonstrated the boosted sensing speed and linearity of the graphene resistance signal using the bandwidth-enhanced method to select the most gas sensitive frequency domain of the noise power density spectrum.

For the AC modulation, we applied a hybrid AC+DC gate voltage on graphene FET, and studied the scattering effect and the speed of charge transfer of the gas-graphene interaction for improving the gas selectivity and sensing recovery speed, respectively. Particularly, we measured the scattering strength of the gas adsorbents on graphene and directly resolve the scattering strength spectrum of water, methanol and ethanol adsorption on graphene, achieving the label-free gas sensing using a single graphene transistor. On the other hand, the studies of charge transfer speed between the gas and graphene inspired us to develop the phase-sensitive scheme on graphene FET, achieving the ultrafast baseline recovery speed (~10s) on a defect-rich, chemical vapor deposition (CVD) grown monolayer graphene FET - almost ten times faster than the previous report

Acknowledgement

First and foremost, I would like to thank my Ph.D. advisor, Professor Liwei Lin, for his generous support and guidance during my time at Berkeley. Back to 2011, I was an undergraduate intern in his lab; six years later, I still admire and get inspired from him whenever we talked – on topics of both research and personal development. It was my great fortune to have a visionary advisor like him who is knowledgeable, resourceful, reasonable, and likeable. Along the time we spent together, he became the James Marshall Wells Academic Chair of ME Department and the directors of several world-class research institutes, yet his continuous and dedicated commitment to the students have never faded, which is an invaluable treasure to my Ph.D. study at UC Berkeley.

I would also thank Professor Jiyoung Chang and Professor Yong Cui for guiding me into the field of nano manufacture and parameter characterization. I would like to thank Professor Ana Arias and Professor Costas Grigoropoulos for offering me with both ambitious encouragements and insightful advices. I would thank my lab mates in the Linlab: Takeshi Hayasaka, Huiliang Liu, Yao Chu, Yoshihiro Kubota, Xiaoqian Li, Danyang Li, Dr. Nirav Joshi, Dandan Wen, Emmeline Kao, Dr. Hyun Sung Park, and Dr. Sina Akhbari. It was a great pleasure to work with you all. I would like to thank Kim Ly, Richard Lossing, Dr. Mike Cable and John Huggins from BSAC for their professional support in each year's IAB research review. It is my great honor to become a member of the BSAC family.

It has been a pleasure to work with many great collaborators outside Berkeley as well. I would like to thank Dr. Luu Nguyen from Texas Instrument and Dr. Steve Wu from Midea Inc for collaborating on the graphene sensor project. I would like to thank Professor Arnel Salvador for teaming up on the PCARI project together.

I would like to thank Dr. Chen Yang, Dr. Qian Zhang, Dr. Li Chen and Dr. Ken Yang for taking care of me during my summer intern at Analog Devices. I am also grateful for the numerous support received from my fellow graduate school friends. I would like to thank Dr. Zhongyuan Lu, Dr. Kevin Chen, Yongjun Li, Sen Lin, Tianshi Wang, Yubei Chen, Feng Chun, Bo Hu and Cheng Ren for being great life buddies during my time at Berkeley.

And I give sincere thanks to my family for their unconditional caring and support during my study overseas. I can't thank my wife enough for her being such a supportive anchor in my life. Thank you, my loved ones, for teaching me how to become a lovely person and a better myself every day.

Finally, I would like to thank the funding supports from NSF, DARPA, TI, Midea, PICARI, BSAC, TBSI, TRF, and ME Department during my PhD studies.

Contents

List of Tables

List of Figures

Introduction

In the modern age of sensing technologies for broad applications such as internet of things, the capability to make low power, small form factor, and versatile gas sensors for applications such as wearable devices and cell phones could revolutionize the fields of gas sensing systems and fabrications. Over the past decade, a great number of miniaturized physical sensors, such as light, motion, heart rate, altitude, have been successfully developed in the mobile devices to deliver reliable sensing tasks to revolutionize the user experiences. The potential future growth area could be chemical interfaces to sense surrounding environmental conditions, such as gases, biomarkers, and explosives. These miniaturized chemical sensors are predicted to have a 32% share of the total mobile sensor market in the next decade. Specifically, gas sensors may monitor critical volatile chemicals (CO, VOC etc.) to determine living conditions from comfort to health threatening and even the possibilities of diagnosing lung related diseases by analyzing exhaled gas from breath.

In recent years, low-dimensional materials (graphene, MoS_2 and others) offer good characteristics as the base sensing structures, such as large surface to volume ratio, low electrical noise, low power consumption and process compatibility with integrated circuits [1,2]. Previously, researchers have reported the ability to detect molecule-level detections using a graphene FET for high sensitivity [3-7] as the emerging platform for chemical sensors [8-10]. However, the practical application of graphene-based gas sensors need to overcome two major hurdles: selectivity and recovery speed before massive commercialization.

1.1 Motivation

The motivations and goal of this thesis are to demonstrate the selectivity of the graphene gas sensor without extrinsic functionalization; to address the critical issue of all gas sensors in slow response time and long-term drift by using the phase changes under different AC driving frequencies; and to develop fabrication process to reduce size and manufacturing cost. These will result in ultra-low power, low form-factor sensors with good sensitivity, stability, response time and gas selectivity – all desirable features for current and future mobile gas sensing applications in wearable devices and cell phones.

1.1.1 Improving sensing selectivity

Extensive amount of research has discussed the sensitivity of graphene gas sensors without addressing the issue of sensing selectivity. Previously, a couple of approaches have been proposed for gas sensing selectivity with a tedious AFM (Atomic Force Microscope) setup [11], or complicated noise measurements

schemes [12]. However, these approaches are not feasible for practical applications in cell-phone based devices.

On the other hand, the current state-of-art standard in gas detectors is to use a gas chromatograph (GC) to separate gas spices and a mass spectrometer (MS) to detect them such as the very bulky and expensive Agilent Model-7890B Gas Chromatograph and Model 6560 MSD/DS Mass Spectrometer. Small-size and low-cost electrochemical sensors, on the other hand, have improved over the years for a wide range of applications but a high temperature sensing platform is required with metal oxides as the sensing materials for good sensitivity which results in high power consumption.

1.1.2 Improving the response/recovery speed

In order to detect specific molecules of low concentration, it may take a long time for molecules to diffuse onto the tiny one-dimensional sensors. Several methods have been proposed to speed up the response time including the utilization of high fluid flow to increase the contact opportunity between the molecules with the sensor with limited success [13-14]. The fundamental dilemma comes from the nanometer geometry of the sensor, which provides high sensitivity but limits the response time.

On the other hand, the recovery time of the gas sensor is often limited by the interaction strength between the gas adsorbent and graphene during the desorption process. Specifically, the defects on the graphene are one of the key factors to strengthen the gas adsorption. These defects, created during the synthesis and transfer process of graphene [14], can bond strongly with the gas molecules as reactive sites [15], causing the drift of the baseline signals. To address this issue, previous efforts were made to: (1) speed up the desorption reactions by exposing the sensor under UV light; and (2) reduce the intensity of defects on the graphene by improving the quality of graphene [16]. Unfortunately, the high sensitivity of a functionalized surface usually promotes the strong adhesion of gas molecule, resulting in difficult desorption and a long recovery time

1.2 Contribution and Thesis Outline

The major technical and conceptual contribution of this thesis can be concluded as follows:

- The proposed approach of a quasi-static method on graphene FETs to enable the evaluation of carrier density and field effect mobility of graphene at quasi-static work function for the first time.

- The introduction of scattering strength, "*S",* for the gas adsorption process to differentiate the defect-induced and the intrinsic gas adsorption processes on graphene using the *S* parameter, and the demonstration of the selective

identification of gas adsorption process on graphene surface without chemical functionalizations.

- A phased sensitive and a bandwidth enhanced noise sensing scheme enabling the selective sensing of the weakly adsorbed molecules on graphene for a boosted gas recovery speed by 10 times.

As shown in Figure 1.1, we explored several types of gas-graphene interaction under a couple states to investigate the topics of gas selectivity and recovery speed of graphene FET gas sensor. In particular, we studied the responses of graphene FET gas sensing under the charge transfer, the scattering, and the adsorption/desorption effects, and explore whether it is possible to probe these effects from the electrical signal of graphene FET, and if such measurements can help to improve the gas sensing performance like strong selectivity and fast recovery speed. Regarding the interaction state, we aimed at sensing (monitoring Dirac Point) and modulate (tuning gate voltage) the graphene FET in the following states: equilibrium (static) and non-equilibrium states (quasi-static and random). Such modulating and sensing of graphene FET actually creates a "virtual array" of graphene sensors operating at different AC frequency, DC work functions, and noise bandwidth, potentially helpful for exacting gas-selective feature in a label-free manner (no functionalization needed on graphene surface).

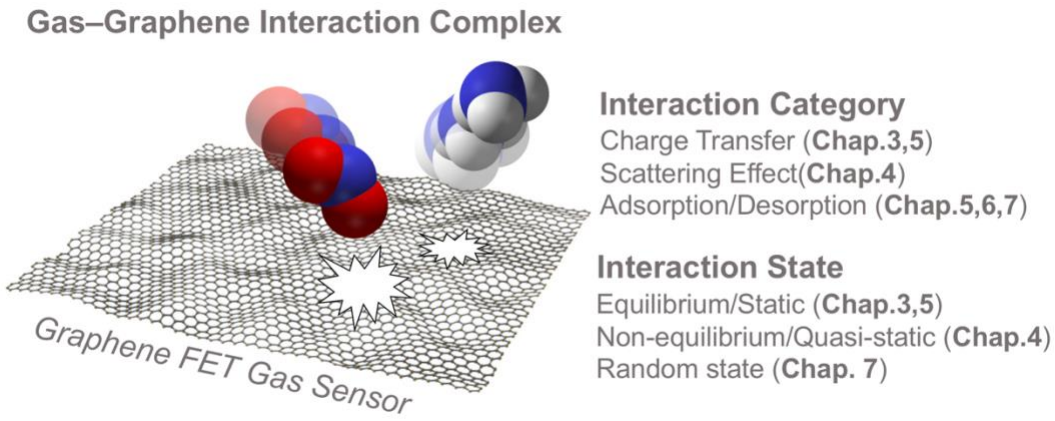

Figure 0.1 Overview of the investigation dimensions for the gas-graphene interaction

Chapter 2 briefly reviews the technical background of the current gas sensor solutions, and provides the related knowledge in solid state physics and device physics to pave the road to understand the design works covered in this thesis.

Chapter 3 explains the principle of the charging and scattering effect associated with gas adsorption process on graphene and their corresponding effects on the electrical parameters of graphene transistors. We introduced the concept of linear factor in this chapter, and demonstrated the usage of such concept to achieve 4 gas selectivity on a single graphene transistor. The content of this chapter is primarily based on [16]

Chapter 4 demonstrates the quasi-static measurement scheme for the linear factor introduced in chapter 3. The advanced technique enables the direct observation of defect-induced and intrinsic adsorption mode of gas on graphene surface. We further introduced the normalization concept called "scattering strength" to discriminate and evaluate the average number of charge transferred per gas adsorbent over a period of time. The content of this chapter is primarily based on [17]

Chapter 5 introduces a new sensing scheme based on the phase of charge transfer between gas adsorbents and graphene. We provided the detailed electrical characterization of the phase signal on graphene, and demonstrated the chemical sensitivity of the phase sensitive scheme. In particular, we highlighted the superior recovery speed of the phase signal as compared to the DC resistance signal of graphene. The content of this chapter is primarily based on [18]

Chapter 6 covers the in-depth analysis, modeling, and application of the phase-sensitive scheme introduced in Chapter 5. In particular, we explained the possible origins of the observed accelerated baseline recovery speed, and envisioned the future application of 3D gas sensing on a 2D surface using this phase sensing technology. The content of this chapter is primarily based on [19]

Chapter 7 discusses the noise based method for gas sensing on graphene, and particularly focuses on the bandwidth enhanced technique to improve the response and recovery speed of the graphene FETs. We compared the noise results from physical cleaved graphene and CVD graphene and analyzed the possible origins. The content of this chapter is primarily based on [20]

Chapter 8 discusses the non-conventional fabrication process (flexible transfer and direct-write) for the emerging application of graphene transistors. The content of this chapter is primarily based on [21,22].

Chapter 9 discusses the future work for graphene gas sensors at room temperature.

Background

In this chapter, we begin with the discussion of the current state of art on the gas sensors, and then dive into the sensing principle of graphene transistors. This chapter prepares readers with the general background knowledge of the state-of-art gas sensors and the necessary physics of graphene related to the works covered in this thesis.

1.3 Current State of Gas Sensors

1.3.1 The Golden Standard for Gas Detection: GC+MS

The golden standard for gas detection is to use both the gas chromatography to separate the gas mixtures together with the mass spectroscopy to differentiate gas species. "A gas chromatograph (GC) uses a flow-through narrow tube known as the *column*, through which different chemical constituents of a sample pass in a gas stream (carrier gas, *mobile phase*) at different rates depending on their various chemical and physical properties and their interaction with a specific column filling, called the *stationary phase*.". After traveling a very long distance, gas with lighter mass will travel faster than those of heavier gas species such that they are separated at the end of the long tube. On the other hand, mass spectrometry (MS) "is an analytical technique that ionizes chemical species and sorts the ions based on their mass to charge ratio." [23]. However, both instruments are very bulky, expensive and consume high power such that they are not suitable for wearable or cell-phone systems.

Various efforts have been working on the miniaturizations of these systems. For example, micromachined GC has been proposed and demonstrated all the way back in 1979 as shown in Figure 2.1 on a whole 2-inch silicon wafer [24]. There have been continuous efforts and new results using more advanced fabrication technologies over the years [25-27]. Figure 2.2 shows the optical photo of a 2008-version of silicon micromachined GC column with a total length of 3 meters of microcolumn with cross sectional area of $100\times100\ \mu m^2$ (the whole area is 3.2 cm^2) driven by the helium gas at 20 cm/s [28]. Although the very long microchannel can be fitted into a relatively small area of 3.2 cm^2, suitable for wearable and cell phone applications, the system is still missing a detector, a pump to provide 20 cm/s of pressure, and the storage tank for the helium gas. As such, the miniaturized GC system is still big and consumes high power – not likely to be the gas sensing solution for the wearable or cell phone applications. On the other hand, there have been efforts in making miniaturized mass spectrometer [29]. For example, Figure 2.3 is a mass analyzer based on the "time of flight" principle for peptides and proteins [29]. Although laser sources, detectors and reflectron devices may already have miniaturized versions, "high voltage" (10kV in this case) and "the requirement of vacuum operations" (open to place samples and close for detections) are not easy for miniaturizations. As such, it has been difficult, if not impossible, to make

miniaturized GC+MS systems and the high power consumption and pumping and vacuum requirements pretty much prevent them for consumer-level cell phone or wearable systems.

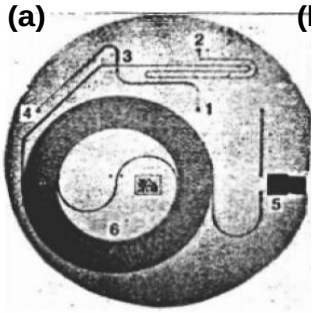

Figure 0.1 GC micro column on a 2-inch wafer [29]

Figure 0.2 GC micro column fabricated on 3.2cm^2 silicon [28]

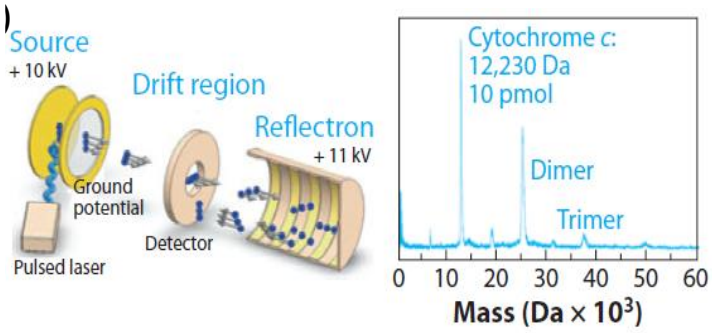

Figure 0.3 Schematic of "time of flight" mass spectrometer [29]

1.3.2 Other Macro Scale Gas Sensors

In addition to the efforts on the GC and MS for miniature gas detectors, there have been many research projects on various types of gas sensors, typically targeting a specific gas detection via principles ranging from electrochemical, optical (infrared), pellistor to chemical resistor based gas sensors in commercial products with good performances but large package size (10 cm^2) and high power consumptions (100 mW) [30-32]. Specifically, electronic nose is an active area

attracting many efforts over the past decades toward the capability of reproducing the senses of smell similar to the human nose [33, 34]. The typical structure of the electronic nose has three parts: a sample delivery system, a detection system, and a computing system to realize the complex functions of smell as illustrated in Figure 2.4 [35]. The computation system may involve complicated artificial neural network, machine learning or other means [36, 37] which are out of the scope of this work. Our goal focuses on the detection/sensor mechanisms and hardware using electrically tunable graphene gas sensor arrays toward the complex electronic nose system. From prior works, one of the most commonly used gas sensors in the electronic noses is based on metal oxide [38, 39] such as the one with a schematic diagram in Figure 2.5 [40], including many nanostructure-based metal oxide sensors such as nanowires, nanofibers, and nanotubes [41]. Although it is well known that sensor selectivity can be fine-tuned by varying metal oxide crystal structure and morphology, dopants, contact geometries, operation temperature or mode of operation [42,43], gas selectivity is still the key problem in these gas sensing devices. Practical systems may have a filter (such as charcoal) to avoid unwanted gases such as organic volatiles [42]. Nevertheless, it is clear that even the start-of-art metal oxide based gas sensors have performance issues in selectivity.

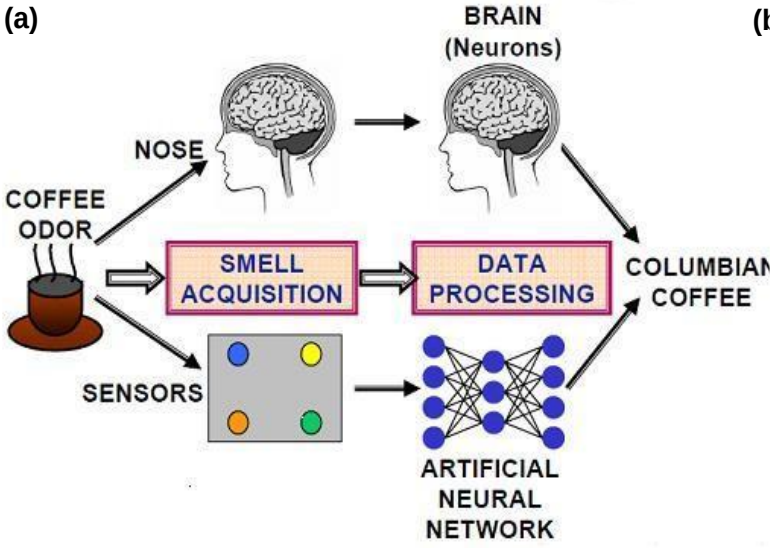

Figure 0.4 Analogy between the human olfactory system and sensor based on neuron network [35]

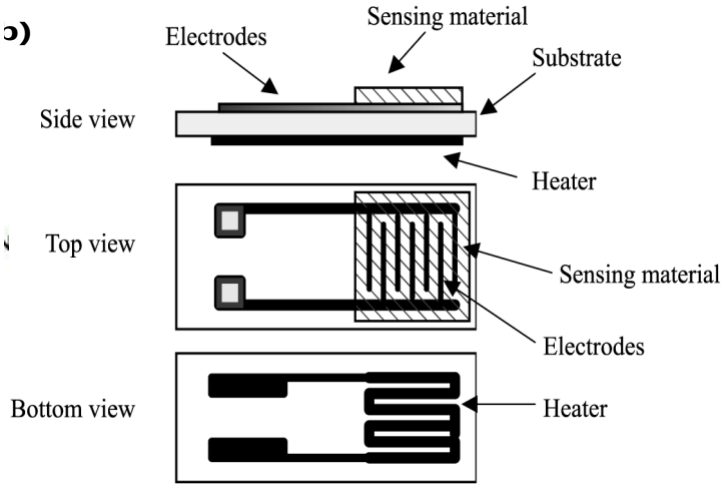

Figure 0.5 Metal oxide based gas sensor with heater [40]

1.4 Gas Sensing on Graphene

Recent advances in nanomaterials and manufacturing processes have led to new engineering designs and approaches in exploring new gas sensors. Graphene, a 2D-semimetal material with zero bandgap [44] can be an excellent sensing material for many gasses. Specifically, graphene-based gas sensors have drawn great interests due to its ultra large surface to volume ratio and semiconducting properties. It has been reported that the resistance of graphene FET is very sensitive to the exposure of several types of gases, i.e. NH_3, NO_2 and H_2O [45], and the corresponding limit of detection (LOD) can reach the single molecular level [46]. Figure 2.6 is a graphene FET structure, including a monolayer of graphene as channel; source, drain, and a bottom gate electrode; and the gate oxide. The key sensing mechanism is the surface charge transfer in Figure 2.7 of two types: electron-doping and hole-doping. For example, electrons of NH_3 will hop from the highest occupied molecular orbital (HOMO) to the Fermi level E_f of graphene, and holes of NO_2 will hop from the lowest unoccupied molecular orbital (LUMO) to the Fermi level of graphene as: $E_{LUMO\_NO2}^{hole} > E_f^{hole}$, where $E_f^{electron} = - E_f^{hole}$. The adsorbed molecules act as temporary external doping sources to affect the majority carrier density in graphene and change the sensor resistance. Since the charge transfer process can take place at room temperature, graphene FET based gas sensors are not required to operate at an elevated temperature with very low power consumption around the microwatt range [47]. Existing research on graphene gas sensing has established a large data base for different gases with one unsolved issue - gas selectivity.

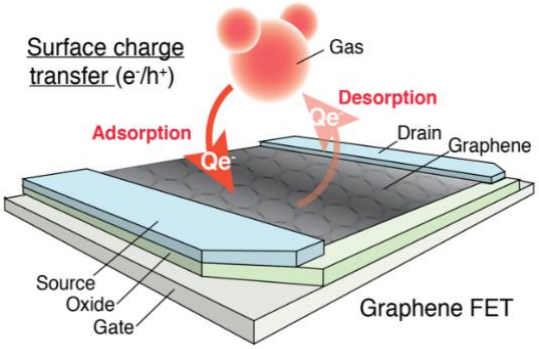

Figure 0.6 Schematic of the surface charge transfer effect on graphene device.

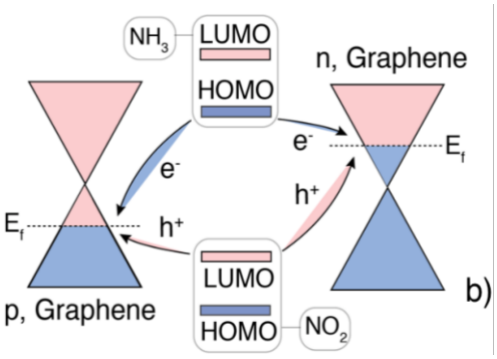

Figure 0.7 Band diagram of the surface charge transfer effect on graphene.

The conduction band and the valence band of graphene contact each other at a single point, and the E-k relation is linear. Applying an electrical field, or equivalently having chemical/bio molecules attached onto the graphene layer, can change its Fermi energy level and thus alter the carrier concentration. Compared to other solid-state sensors, graphene is an exceptionally low-noise material electronically [48] and the high signal to noise ratio gives graphene-based sensors the capability to resolve even a few extra electrons induced by chemical dopants. Low electrical noise in graphene comes from its special 2D structure. First, the structure makes graphene a highly conductive material, hence low Johnson noise even in the limit of no charge carriers [47, 49-51]. Second, graphene has few crystal defects [49-51], which ensures a low level of excess (1/f) noise caused by their thermal switching [52]. Third, four-point probe measurements on a single-crystal graphene can be integrated to the as-fabricated device in this proposal, where the electrical contacts only contribute negligible noise to the total signal. Furthermore, Graphene-based sensors can have linear response when electrically biased to higher carrier concentration region, away from the neutrality point [36]. At this region, extra carrier concentration Δn depends linearly with the concentration of the chemical to be examined. Thus the electrical conductivity, which equals $\sigma = ne\mu$ (e is the electron charge and μ is the mobility) also varies linearly with the concentration of the chemical substances. However, the gas selectivity issue needs innovative solutions.

Selective Gas Sensing on a Single Graphene FET

In this chapter, we discuss the principles and experimental results of selective detection of gas molecules on the pristine graphene surface via the charged impurity scattering effect. We firstly reviewed the analytical model of graphene transistor working at DC condition and explained the role of charged impurity in affecting the carrier density and field effect mobility of graphene, and then we proposed the method to extract "linear factor" from the electrical measurements to differentiate four different gases. Compare to the state-of-art, there are three distinctive contributions demonstrated in the work: (1) first demonstration of selective gas sensing (NO_2, NH_3, H_2O and CH_3OH) using a single graphene FET; (2) experimental proof of linear dependence between the inverse of the field effect mobility and the carrier density (proportional to the measurement of Dirac Point voltage) upon gas molecule exposure; (3) utilizations of such linear characteristic for selective gas sensing. At the end, we also examined the sensing repeatability of such method, and explored using "linear factor" to achieve gas selectivity in the binary mixture environment. This chapter proposes a new sensing scheme which could open up a different class of graphene-based, selective gas sensing devices for practical uses as well as fundamental scientific research.

1.5 Introduction

Previously, it was shown that the resistance of graphene FET is very sensitive to the exposure of several types of gases, i.e. NH_3, NO_2 and H_2O, and the corresponding limit of detection (LOD) can reach the single molecular level [53]. Extensive amount of research efforts have been focused on the approaches to improve the sensitivity of graphene gas sensors by introducing external defects and junction structures, yet few efforts were dedicated to address the critical challenges of gas sensing selectivity given the complex nature of this problem. Although graphene is considered as an inert material which is chemically stable in air up to 400^{o}C, mild charge transfers can take place between graphene and several families of chemicals, resulting in a severe issue of sensing selectivity when used as a chemical sensor. Previously, a couple of approaches have been proposed for gas sensing selectivity with a tedious AFM (Atomic Force Microscope) setup [54], or complicated noise measurements schemes [55]. These approaches are not feasible for practical usages. Therefore, graphene can be very useful to detect sub-ppm level of gas given its sensitivity, yet it is problematic for massive scale application given the poor selectivity when various types of gas are present in the typical environment.

Such dilemma motivated us to explore new methods to differentiate gas adsorptions on graphene using the electrical properties change of graphene. Specifically, the surface charge transfer effect between gas molecule and graphene, which can

change both the carrier density and the field effect mobility of graphene upon gas adsorption, is often characterized only by the electrical resistance change of graphene without further in-depth studies. As mentioned above, the electrical resistance signal of graphene is not enough for selective gas sensing, but using the signals of the carrier density and field effect mobility of graphene can probably help reveal finer and in-depth information regarding the gas dopant, thus achieving improved gas selectivity. For example, an ammonia molecule adsorbed on graphene FET can act as a unique dopant to donate certain electrons and lower the channel resistance by increasing the carrier concentration; at the same time, the positively charged ammonia molecule (after doping its electron to graphene) can become an special charged impurity sitting on pristine graphene scattering the transport of carriers and alter the field effect mobility of graphene. The combination of such two effects collaboratively affect the electrical resistance of graphene and reveals in-depth physiochemical information for gas differentiation. In this work, we demonstrate the feasibility to distinguish four types of gases (NO_2, NH_3, H_2O and CH_3OH) by measuring the incremental change of graphene carrier density (proportional to the measurement of Dirac Point voltage) and the field effect mobility (proportional to the measurement of conductance ~ gate voltage slope) of a single graphene FET at room temperature. By exploring the linear dependence between the reciprocal of the field effect mobility limited by the long-range scattering and the Dirac Point voltage of a graphene FET, we experimentally demonstrate such linear factor is unique for the differentiation and selective sensing of gases.

1.6 Charged Impurity Scattering Effect

Unlike the bulk semiconductor (silicon) or other 2D materials (such as MoS_2) where the phonon scattering is the major limiting factor for field effect mobility [56], it is previously reported that the field effect mobility of graphene at room temperature is mostly limited by the population of the charged impurities, scattering the carriers through the Coulomb effect. Since the gas adsorbents become charged centers after the doping events, this unique mobility-sensitive property of graphene provides a new dimension to detect and possibly differentiate gas molecules. For example, a gas molecule on the top surface of graphene becomes an α (positively) charged impurity after donating α electrons from its molecular orbital to graphene. This effect will further change the Dirac Point voltage and the carrier mobility of the graphene FET due to the change in: 1) the carrier concentration, n, of graphene, and 2) the charged impurity concentration, n_{imp}, on top of graphene, respectively.

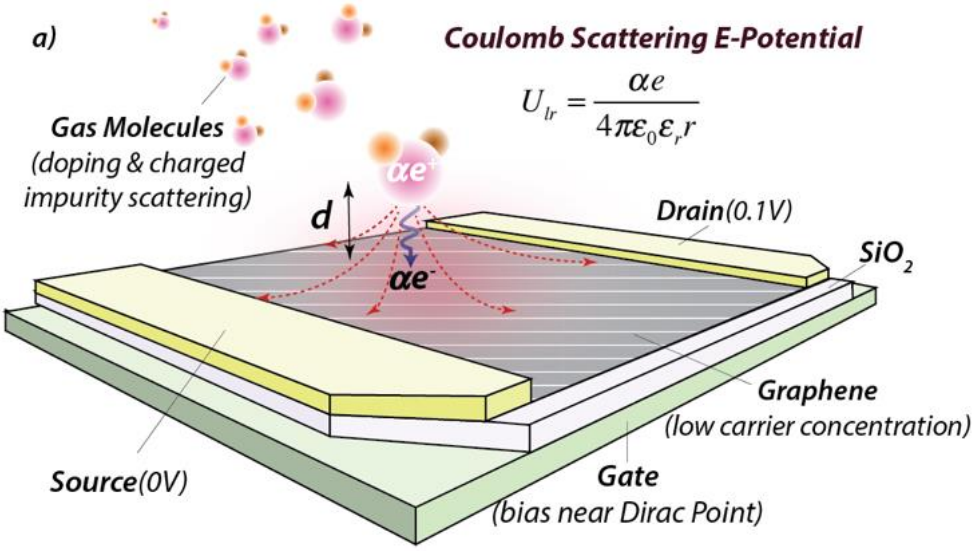

Figure 0.1 Coulomb Scattering Effect (Long range).

In principle, there are two major scenarios after the gas molecule becomes charged impurity (carrier scattering center) on graphene: 1) the electrical scattering potential of the gas adsorbent is long-range, or the "Coulomb scattering potential" - when the screening effect is weak due to the low carrier concentration in graphene; and 2) the electrical scattering potential is reduced into short-range, or the "delta scattering potential" - when the screening effect is strong due to the high carrier concentration in the graphene channel. Therefore, the charged impurity can behave differently depending on the screening environment provided by the carriers in graphene. Figure 3.1 shows a single charged impurity which scatters the carriers in a long-range manner with the electrical scattering potential following Coulomb's law. This happens when the carrier concentration is small as compared with the charged impurity concentration, or the gate voltage is biased near the Dirac Point. On the other hand, Figure 3.2 shows a single charged impurity which scatters the carriers in a short-range manner with the electrical scattering potential being a delta function, where r_0 is the position of the charged impurity. This happens when the carrier concentration is high as compared with charged impurity and the Coulomb scattering potential is completely screened by the carriers in graphene. In the illustration, *d* is the equilibrium distance between the gas molecule and graphene surface, and *r* is the distance between charged molecules and scattered carriers. For the fabricated transistors using CVD graphene, such charged impurities can be found on top surface (by gas dopant) and bottom surface (substrate defect dopants) of graphene.

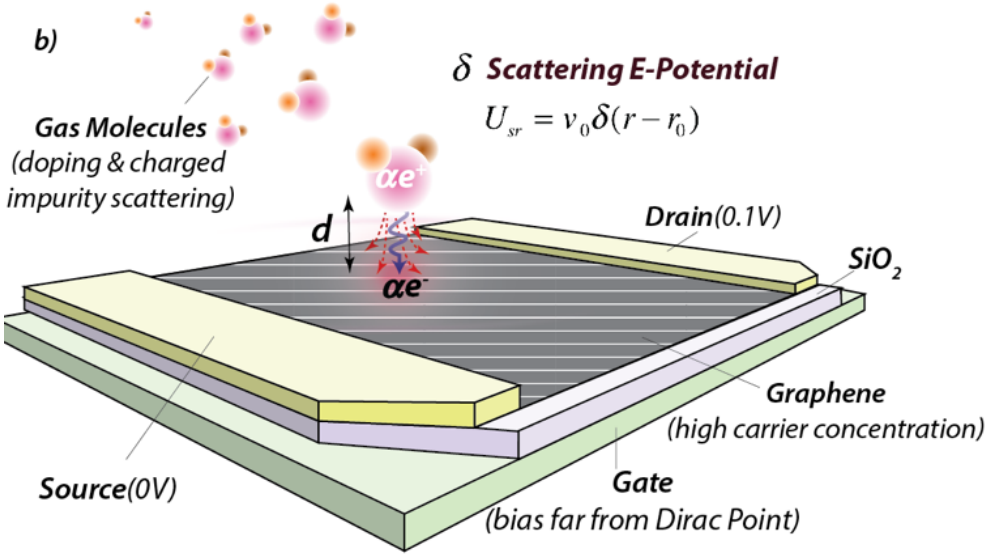

Figure 0.2 The short-range scattering effect due to the point defects on graphene.

Analytically, it is known that for short-range scattering, the mean free path $l_{sr} \sim 1/\sqrt{n}$, where n is the carrier concentration, and for long-range scattering the mean free path $l_c \sim \sqrt{n}$ [56]. The carrier concentration of graphene FET can be modulated by the gate voltage,

$$n = c_g(V_G - V_{G,Dirac}) \tag{3.1}$$

where V_G is the gate voltage, c_g is the gate capacitance per unit area, or 1.2×10^{-4} Fm^{-2} for the 300 nm SiO_2 gate dielectric material used in the prototype devices. At low carrier concentration of $n \approx n_{imp}$ in the order of 10^{11} cm^{-2}, one can estimate that l_{sr} ~1,000 nm and l_c ~50 nm. Therefore, when the gate voltage is biased near to the Dirac point (lowest carrier concentration), graphene transport is dominated by the long-range scattering, with carrier mobility:

$$\mu_e = \mu_{e,c} = \frac{C_e}{n_{imp}} \tag{3.2}$$

$$\mu_h = \mu_{h,c} = \frac{C_h}{n_{imp}}$$

where μ_e and μ_h are the electron and hole field-effect mobility, $\mu_{e,c}$ and $\mu_{h,c}$ are electron and hole long-range scattering limited field-effect mobility, C_e and C_h are gas-unique constants that are only relevant to the band structure of graphene, c_g, α and d (see Figure 3.1). If the channel length in the graphene FET (~um) is much larger than the typical mean free path (~nm), the diffusive Drude-Boltzmann model can be adopted to derive the conductance $\sigma(V_G)$ of graphene [57]:

$$\begin{cases} \sigma(V_G) = \mu_e c_g (V_G - V_{G,Dirac}) + \sigma_{Dirac} & V_G > V_{G,Dirac} \\ \sigma(V_G) = -\mu_h c_g (V_G - V_{G,Dirac}) + \sigma_{Dirac} & V_G < V_{G,Dirac} \end{cases} \quad (3.3)$$

where σ_{Dirac} is the residual conductance at the Dirac Point. The Dirac Point voltage is the gate voltage at the minimum point of the conductance, and the majority carrier is electron/hole if the gate voltage V_g is bigger/smaller than $V_{g,Dirac}$.

When exposed to a particular gas, it is assumed that gas molecules adsorb on graphene surface gradually, namely the gas molecule per unit area on graphene, $N_{gas}(t)$, increases linearly with respect to the exposure time, t, in the initial stage. As such, both n and n_{imp} also vary linearly with time, or $\Delta n(t) \sim N_{gas}(t)$ and $\Delta n_{imp}(t) \sim N_{gas}(t)$. According to Eq. (3.1) and (3.2), one can observe that the Dirac Point voltage and the inverse of long-range scattering limited mobility will also vary with time linearly, or $\Delta V_{G,Dirac}(t) \sim N_{gas}(t)/c_g$ and $\Delta[1/\mu_{e/h,c}(t)] \sim N_{gas}(t)/C_{e/h}$. Interestingly, the ratio between the two quantity, $\Delta[1/\mu_{e/h,c}(t)]/\Delta V_{G,Dirac}(t) \sim c_g/C_{e/h}$, which is a gas related constant and will not change with the exposure time. Therefore, we can parameterize the above-mentioned ratio as the "linear factor" and use it to label different gas molecules on the graphene FET. As such, a single graphene FET can be used to detect different types of gas molecule selectively by characterizing the linear factor from real time measurements

1.7 Experiment Setup

In this section we briefly introduce the device and setup used in the experiments. Figure 3.3 shows the gas sensor package installed on a breadboard, and the microscopic optical picture of the as-fabricated graphene FETs. The monolayer graphene channel can be seen on the SiO_2 substrate. The transfer length method [58] is used to determine the contact resistance between the source/drain electrode and the monolayer graphene as ~100Ω. The "Hall bar" structure in Fig. 3.3 is used to measure the pristine (before exposure to gas molecules) of the carrier (electron/hole) mobility of graphene by the hall effect mechanism [52] and a representative mobility value for the prototype device is around 1000 cm^2/Vs.

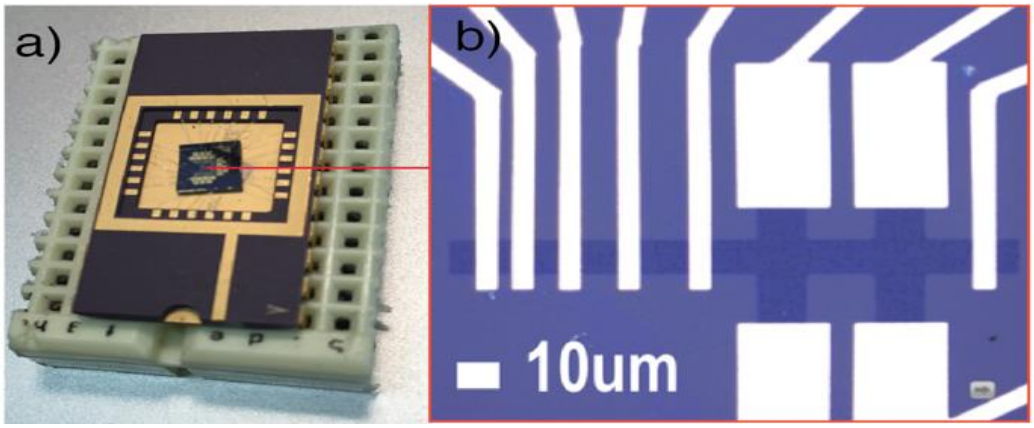

Figure 0.3 Devices fabricated for gas sensing experiments.

Figure 3.3 shows the optical photo of the gas sensing test setup. The graphene FET was sealed in the chamber, under ambient atmosphere and room temperature. A microliter pump (New Era Pumping Systems NE-300) is used to pump into the liquid chemicals to produce gas vapors into the sensing chamber, while water vapors were extracted out by using the drying agent. This system can control gas vapor inputs at the level of 100 ppm/s. A semiconductor parameter analyzer (Agilent 4145B) is used to measure the graphene channel conductance versus gate voltage (-40V<V_g<40V), while the voltage between the source and drain electrode is V_{DS}=0.1V throughout the experiment. The semiconductor analyzer is controlled with a Labview program, while the characteristics of the graphene FET are calculated using a Matlab program afterwards.

The sensing cycle starts from measuring the conductance versus gate voltage curve of the sealed graphene FET in its idle state (without gas). The microliter pump was turned on manually at a desired pumping speed and the gas vapor starts to enter the chamber. The semiconductor parameter analyzer measures the conductance versus gate voltage curves for several times to characterize the concentration changes of the input gas. The conductance versus gate voltage profiles were then used to generate the change of carrier density (through tracking the Dirac Point shift) and the change of field effect mobility (through tracking the slope shift as shown in Equation 3.3). In the prototype tests, the interval between these measurements is set at 15 seconds. After the pump is turned off, the gas sensor is released to the ambient atmosphere by opening the chamber lid.

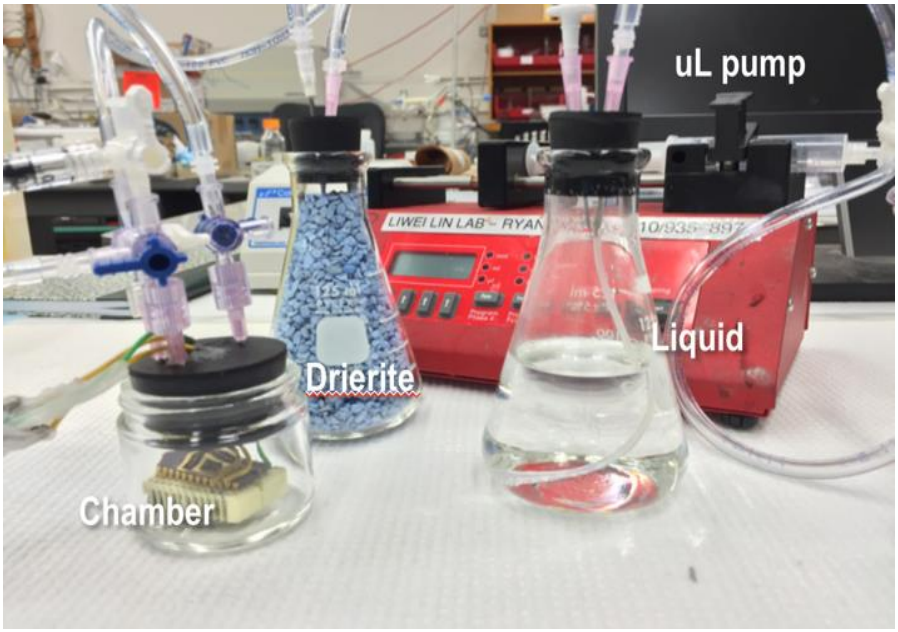

Figure 0.4 The gas sensing setup.

1.8 Results

Figure 3.5 shows the-real time conductance versus gate voltage of graphene FET measurements during the exposure of NO_2, NH_3, H_2O and CH_3OH vapors, respectively. The solid curves are the idle state (before gas vapor exposure), and the dashed curves are doped states. The gas vapor flow rate in the chamber is set at a constant value around 750 ppm/s. As shown in the Figure 3.5 that NO_2 vapor accepts electrons from graphene such that the Dirac Point voltage shifts positively as $\Delta V_{G,Dirac}(t)/\Delta t>0$. In the case of NH_3, H_2O and CH_3OH, these vapors donate electrons to graphene such that the Dirac Point voltage shifts negatively, as $\Delta V_{G,Dirac}(t)/\Delta t<0$.

One can derive $\mu_{e/h}(V_g)$ for each conductance ~ gate voltage profile using Eq. (3-3), and derive the long-range limited mobility $\mu_{e/h,c}= \mu_{e/h}(V_G)$ at gate voltage V_G nearby the Dirac Point. In this work, we choose $V_G = V_{G,Dirac}\pm 2V$ to derive the corresponding real time long-range scattering limited mobility $\mu_{e/h,c}(t)$. It is important to note that the calculation of $\mu_{e/h,c}(t)$ does not rely on the choice of V_G because the long-range scattering limited mobility is relevant to the concentration of charge impurity and not sensitive to the carrier concentration, or the choice of V_G. If the applied gate voltage is far away from the Dirac Point, the scattering potential goes into the short-range scattering regime.

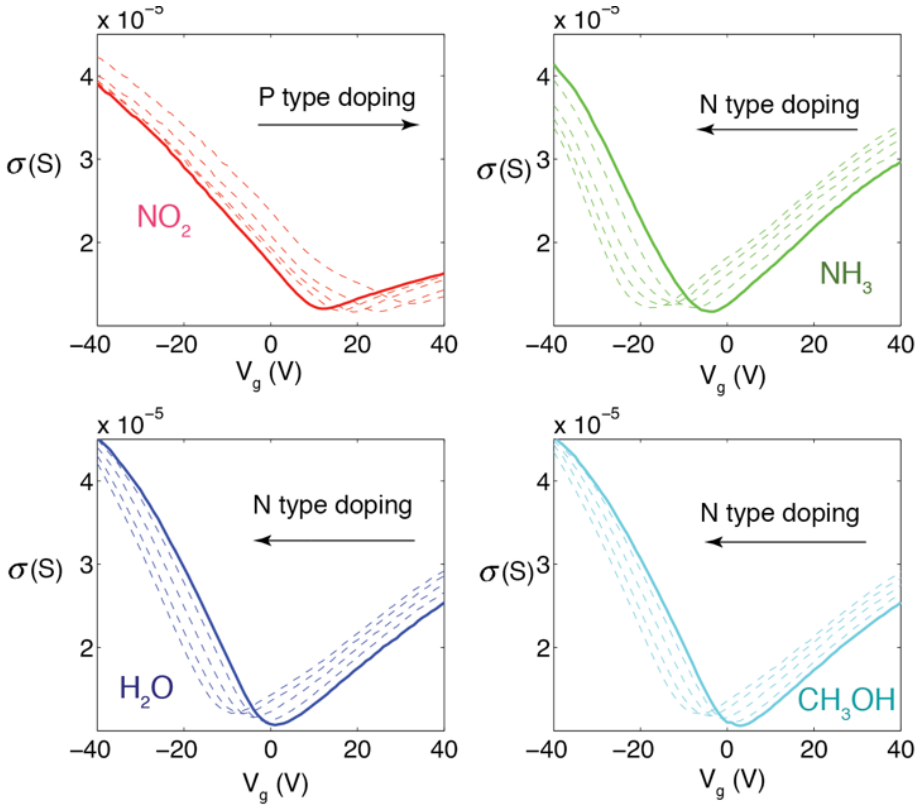

Figure 0.5 The conductance v.s. gate voltage profiles under different gas adsorptions

Figure 3.6 shows the as-calculated real time inverse of the field effect mobility $\Delta[1/\mu_{e/h,c}(t)]$ versus the Dirac Point voltage $\Delta V_{G,Dirac}(t)$ for the electron and hole regimes, respectively. Each data point represents a specific exposure time of graphene FET to a particular gas. The linear dependence between $\Delta[1/\mu_{e/h,c}(t)]$ and $\Delta V_{G,Dirac}(t)$ is expected but not well demonstrated in the prototype measurements. This is due to the measurement errors as well as the noises in the testing system. In order to reduce the randomness for better linearity presentation, we took the summations of the data points as (x_i', y_i') as defined by:

$$x_i' = \sum_{j=1}^{i} x_j \qquad (3.4)$$

$$y_i' = \sum_{j=1}^{i} y_j$$

The bottom two figures in Figure 3.6 shows the summation results have better linearity presentation with the linear factors at different gas exposure time and clearly different between the four gases.

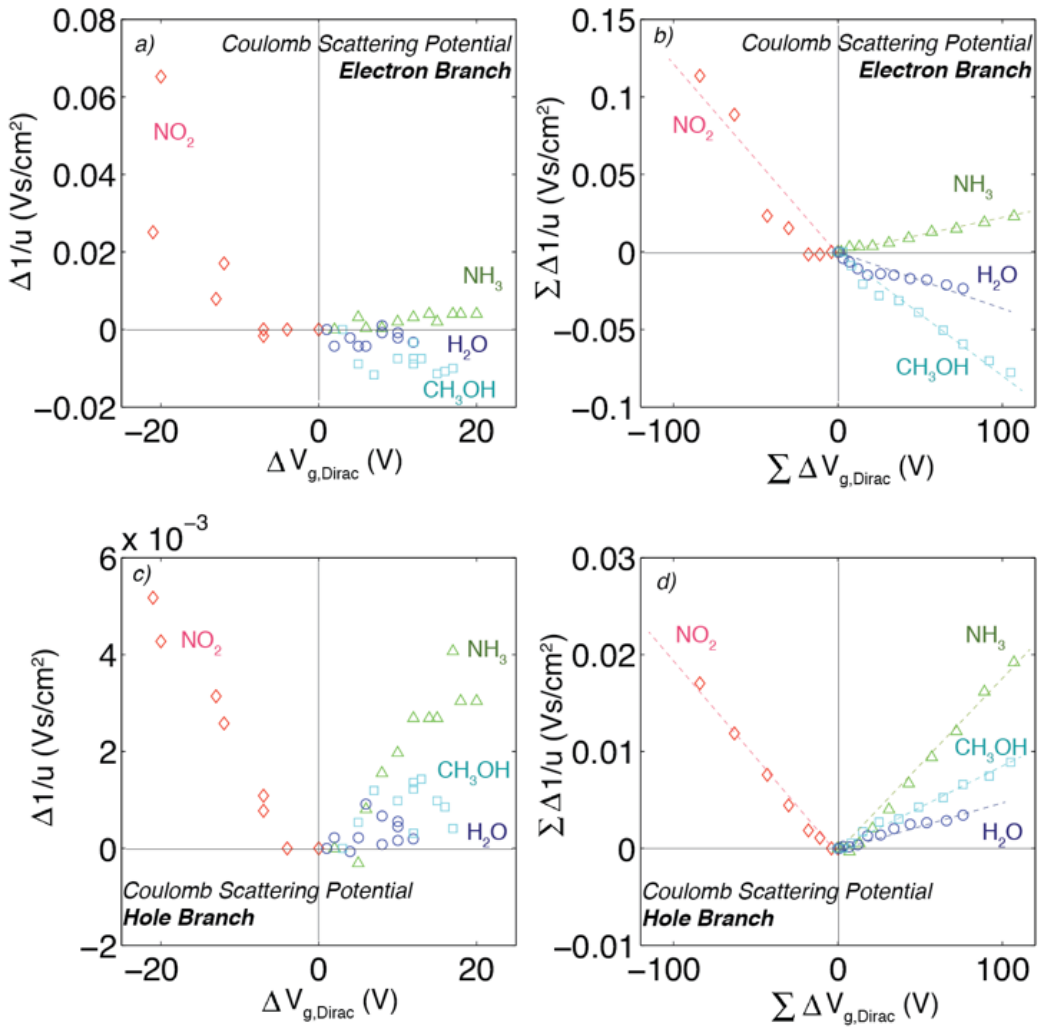

Figure 0.6 Linear factor extraction from conductance v.s. gate voltage profiles.

The linear factor of each gas vapor is further fitted using the data points in Figure 3.6 and the fitting results and the norm of residuals are shown in Table 3-1. It is observed that the norm of residuals for NO_2 in the electron regime is larger than results in the other regime. This is because less data was collected in the prototype tests (see Figure 3.5) as the maximum applied gate voltage (40V) is close to the Dirac Point of NO_2 doped graphene FET. The problem can be alleviated by extending the applied gate voltages to higher values.

Table 0-1 Linear Factor Fitting Results (norm of residuals)

Gas	Hole Regime $\times 10^{-4}$ (norm of residuals)	Electron Regime $\times 10^{-4}$ (norm of residuals)
NO_2	-1.975 (0.0023)	-12.94 (0.0436)
NH_3	1.870 (0.0021)	2.113 (0.0023)
H_2O	0.465 (0.0008)	-2.763 (0.0099)
CH_3OH	0.796 (0.0011)	-7.088 (0.0120)

1.9 Discussion

1.9.1 Repeatability of Gas Sensing on Graphene

We further investigated the repeatability of the devices and gas sensing under multiple gases – these are often neglected in published papers in the literature but vital in practical applications. First, Figure 3.7 shows some of the real-time results using the prototype graphene FET sensors for the repeatability tests on NH_3 and different water vapor concentrations, respectively. In both cases, N_2 is used as inert gas to allow graphene sensors to return back to the original states and the V_G versus time results are plotted and the values of channel resistance are represented in different colors. In the ammonia test, it is observed and expected that the channel resistance would decrease when 2000 ppm of ammonia was introduced (white dashed lines) and stead state was reached after about 100 seconds.

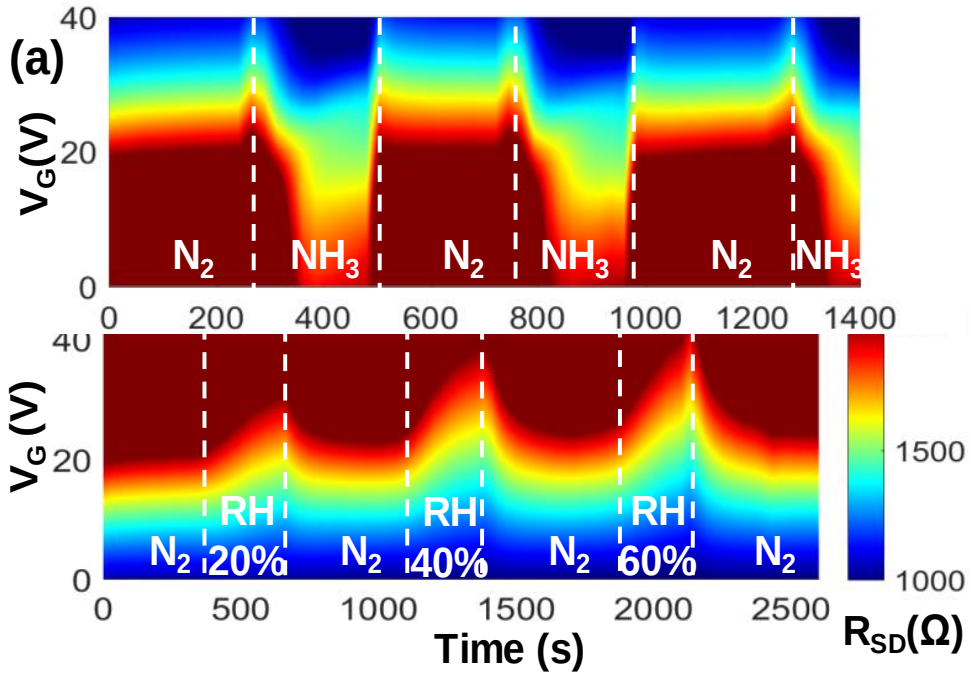

Figure 0.7 Real-time resistance v.s. gate voltage profile.

Furthermore, specific V_g values in around 20 Volts (close to the Dirac point of the device) result in better variations (sensitivity) of the graphene channel resistance changes. If V_G is far away from 20 Volts, such as 0 or 40 volts, there is little changes in graphene channel resistance. The repeatability of the sensor is clearly observed here as well. Similar repeatability results are also observed in the water vapor tests under different relative humidity from 20%, 40% to 60% as shown. First, N_2 can bring the sensor back to initial state but with a slower speed than those in the NH_3 responses. This implies that it is easier for NH_3 to be detached from the graphene. Second, the graphene channel resistance increases as water vapor is introduced and increases linearly with respect to the water vapor concentration.

1.9.2 Selectivity in Binary Gas Mixture

In addition to the experimental proof of a label-free approach to differentiate different gases as shown in section 3.4, we further explored the possibility of achieving gas selectivity in binary gas mixture using a similar protocol. As shown in Figure 3.8, the schematic diagram shows the principle of using the linear factor measured by a single graphene sensor for the reading of multiple gas concentration (in this case, binary mixture of O_2 and H_2O) gas environment. With the known (or measured) linear dependence values between $\Delta 1/\mu_{e/h,c}(t)$ and $\Delta V_{G,Dirac}(t)$ as illustrated in Figure 3.8, the responses of the mixture of O_2 and H_2O are plotted in the blue lines under three conditions: 10% O_2 and 20% H_2O, 10% O_2 and 10% H_2O, and 20% O_2 and 10% H_2O. Analytically, any gas combination can be resolved if the sensing system has infinite high resolution and experimental results are falling on the straight lines. The preliminary results are also plotted in Figure 3.8 in the basic characterizations of O_2 and H_2O gases in green and red color lines, respectively. It is observed that the sensor responses increase linearly with respect to the concentration. Furthermore, when a mixture of 10% O_2 and 10% H_2O is placed into the chamber, the testing results are shown in the blue dotes – matching well with the analytical predictions to differentiate both the individual gas types and concentrations in the mixture.

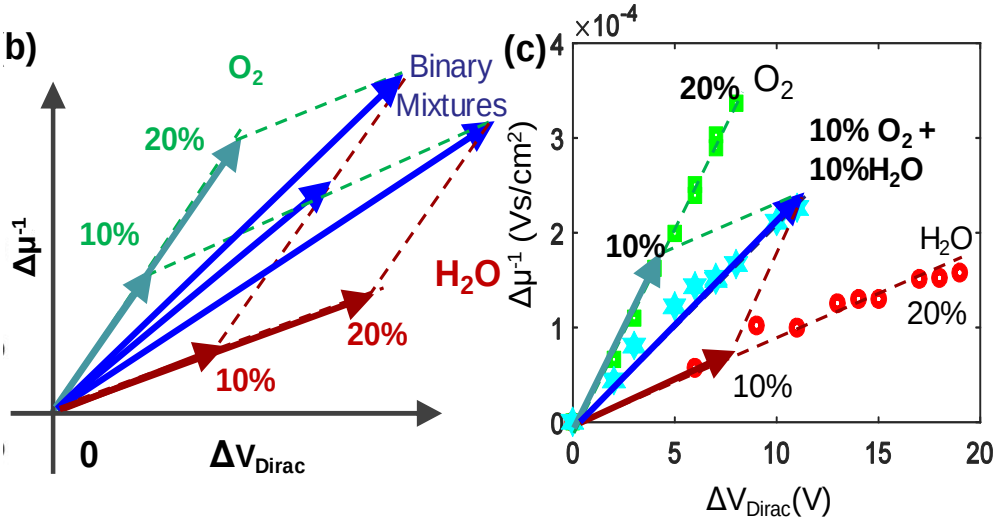

Figure 0.8 Principle and experimental results of gas selectivity based on linear factor.

1.10 Conclusion

In conclusion, we have successfully demonstrated the technique to detect multiple vapors selectively using a single graphene FET gas sensor in this chapter. By measuring the conductance versus gate voltage of a graphene FET, one can derive the unique long-range scattering limited carrier mobility $\mu_{e/h,c}(t)$ and the Dirac Point voltage $V_{g,Dirac}(t)$ for each gas in real time. Experimentally, we have validated that different types of gases have their own specific ratio of $\Delta[1/\mu_{e/h,c}(t)]/\Delta V_{g,Dirac}(t)$, defined as the linear factor. As such, a single graphene FET can be used to detect

a particular type of gas molecule selectively by measuring the linear factor. We also examined the possibility of using the "linear factor" method in resolving multiple gas concentrations directly in their mixture environment.

The Quasi-static Method for Graphene Gas Sensing

In chapter 3, we introduced the DC sensing technique based on charged impurity scattering effect to selectively detect several gases. In this chapter, we extended our discussion of gas-induced scattering effect on graphene with focus on the quasi-static measurement technique. Compared with the DC measurement technique introduced in Chapter 3, the quasi-static approach aims at probing the charging and scattering effect of gas molecules without sweeping a wide range of the gate voltage of graphene transistor. As such, the electrical environment and the work function of graphene can be minimally changed during the entire gas adsorption/desorption process. Furthermore, we defined a new concept called the "scattering strength", similar to the "linear factor" explained in Chapter 3, to quantitatively describe the number of electrons transferred per gas adsorbent in an averaged time period. We also explored the possibilities to modulate the scattering strength by compensating the graphene impurities via the gate voltages and gas adsorptions, and discussed the possible modulations to improve the selectivity of a graphene transistor. These findings reveal new understanding in gas-induced charge transfer effects on graphene to advance the design of the selective platform for gas sensing application.

1.11 Introduction

The charge transfer effect associated with gas adsorption is highly dependent on the physical and chemical environment around the graphene surface. Key sensing parameters, including the work function, temperature, and surface electric field strength, need to be carefully monitored for the characterization of the charge transfer process. However, previous methods [59,60] in obtaining the carrier density $n(t)$ and field effect mobility $\mu(t)$ of graphene transistor introduced in Chapter 3 require sweeping the gate voltage V_G across the charge neutral point (CNP) [61] to track the incremental changes of the CNP voltage, ΔV_{CNP} ($\Delta n = C_G \Delta V_{CNP}/e_c$, where C_G is the gate capacitance per unit area of the graphene FET; $e_c = 1.6\times10^{-19}$C is the elementary charge; and Δn is the change of carrier density). Furthermore, the range of the sweeping gate voltage needs to be large enough to cover the linear region of the graphene FET to extract $\mu(t)$ [62], which often inevitably causes non-trivial changes of charge transfers, such as the fluctuation of the graphene work function [63] (a few hundred meV) and the flipping of the electric field direction at the graphene surface[64].

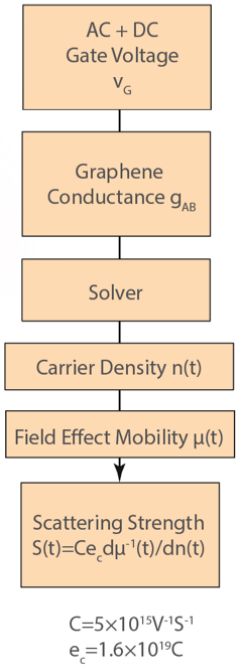

Figure 0.1 The signal process flow for measuring the scattering strength.

Here, we propose a new method to probe $n(t)$ and $\mu(t)$ without sweeping the gate voltage as shown in Figure 4.1. By adding a serial small AC voltage v_g on the static DC gate voltage, one can analytically solve both $n(t)$ and $\mu(t)$ from the graphene conductance g_{AB}. For simplicity, we use the hole branch of graphene as the example as most devices are naturally p-doped in air [65] after fabrication, such that $n(t)$ represents the density of holes. The DC gate voltage of the FET is kept at V_G=-10V (V_{CNP}=20V) and the AC gate voltage $|v_g|$=1V is oscillating at 50Hz to slightly fluctuate the work function of graphene by a few meV while keeping the work function quasi-static. The carrier density variation, $n(t)$, and the inverse of the field effect mobility variation, $\mu^{-1}(t)$, can be extracted from the channel conductance of graphene in real time. As such, the electrical environment and the work function of graphene can be preserved quasi-statically during the gas adsorption/desorption process, which can provide a platform for characterizing the gas charging and scattering effect.

1.12 Probing Charging and Scattering of Gas Quasi-statically

The applied DC gate voltage V_G is at least 15V away from the V_{CNP} to avoid the effect of quantum capacitance of graphene [66] such that the gate capacitance per unit area C_G can be viewed as a constant (C_G=1.15×10^{-4} F/m^2 for 300nm SiO_2). One can then solve $\mu(t)$ and $n(t)$ as two unknowns from the following two independent equations from measurements: the DC component (after low-pass filter f_c=5Hz) of graphene conductivity $G_{AB}(t)=\mu(t)n(t)e_c$; and the AC component of the graphene conductivity $g_{ab}=\mu(t)C_G v_g$. In order to focus on the field effect mobility change associated with the gas adsorption (charged impurity scattering

effect), we subtracted a constant resistance R_{sr}=150Ω from the graphene channel resistance to eliminate other gas-irrelevant scattering effects [67].

As shown in the Figure 4.3, a lock-in amplifier is used to measure the graphene conductivity $g_{AB}=I_D/(v_{AB}\ W/L)$ by measuring the voltage between electrodes A and B under $I_D=1\ \mu A$. The DC component and AC component of v_{AB} are derived using low pass filters and FFT techniques, such that the transient signals of carrier density and field effect mobility can be evaluated as: $n(t)= C_G/e_c|v_g|(|V_{AB}|-I_DR_{sr})/(|v_{ab}|)$ and $\mu^{-1}(t)=C_G|v_g|(|V_{AB}|-I_DR_{sr})^2/(|v_{ab}|I_D)W/L$ where $W/L=3/5$ is the geometry factor of the graphene channel in this work. The detailed derivation is explained in the section 4.2.1 with the preliminary experimental results provided in section 4.2.2.

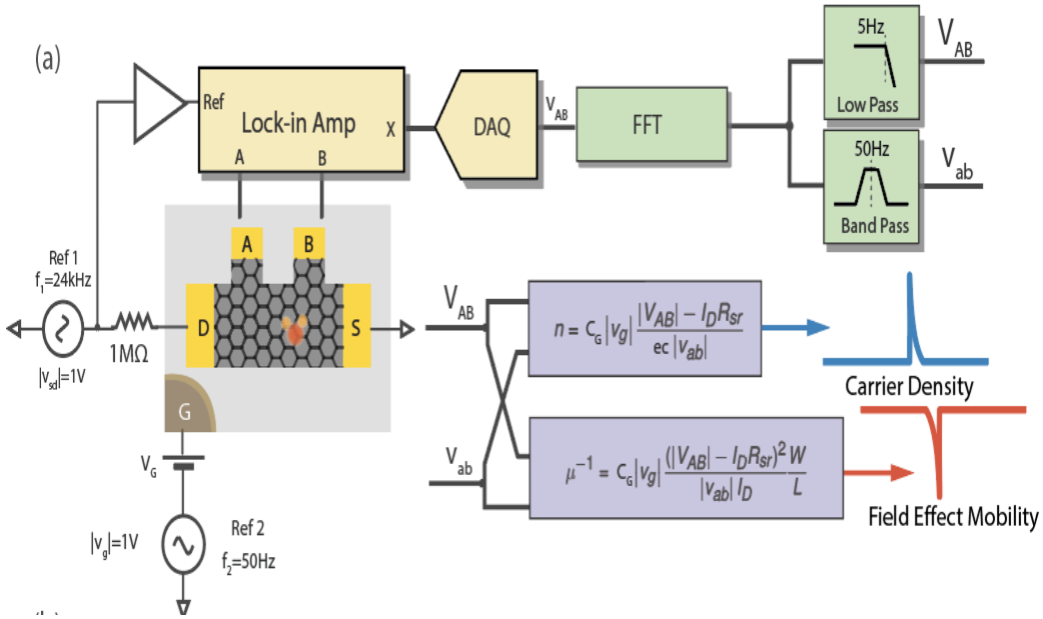

Figure 0.2 Schematic of the sensing signal flow in the experiment.

1.12.1 Derivation of the *n(t)* and *μ(t)* from quasi-static measurement

It is important to note that $\mu(t)$ and $n(t)$ are generally not independent to each other in the electric transport system, but the field effect mobility of graphene at room temperature is dominated by the charged impurity scattering effect, which is independent to the carrier density. We also assume that the inverse of the field effect mobility dominated by the short-range scattering effect is negligible during the gas sensing process, given that the dominating scattering sources are the point defects which are unlikely to be altered by the mild gas adsorption and desorption process. The resistivity of graphene due to charge impurity scattering can be derived by subtracting the resistivity limited by the short-range scattering from the total resistivity:

$$R_{tot} - R_{sr} = \frac{1}{n\mu\frac{W}{L}}, \quad n = C_G(V_G - V_{CNP}) \tag{4.1}$$

where n is carrier density of graphene and μ is field effect mobility; W and L are width and length of the graphene FET channel; R_{tot} is the total resistance; R_{sr} is the

resistivity due to short range scattering which is independent with carrier density; C_G is the gate capacitance; and V_{CNP} is the Charge Neutral Point. When an AC voltage v_g is applied to the gate electrode in addition to V_G, the resistivity can be derived as:

$$R_{tot} - R_{sr} = \frac{1}{c_g(V_G - V_{CNP} + v_g)\mu\frac{W}{L}} = \frac{1}{C_G\mu\frac{W}{L}}\frac{(V_G - V_{CNP} - v_g)}{(V_G - V_{CNP})^2 - (v_g)^2} \quad (4.2)$$

When the AC voltage v_g is much smaller than the offset between gate voltage and the voltage of Dirac Point $|v_g| << |V_G - V_{CNP}|$, we can further introduce the approximation as:

$$R_{tot} - R_{sr} \cong \frac{1}{C_G\mu\frac{W}{L}}\frac{(V_G - V_{CNP})}{(V_G - V_{CNP})^2} - \frac{1}{C_G\mu\frac{W}{L}}\frac{v_g}{(V_G - V_{CNP})^2} \quad (4.3)$$

which gives the DC and AC components of the resistivity as limited by the long-range scattering (charged impurity scattering):

$$R_{dc} - R_{sr} = \frac{1}{C_G\mu\frac{W}{L}}\frac{1}{V_G - V_{CNP}} \quad (4.4)$$

$$R_{ac} = -\frac{1}{C_G\mu\frac{W}{L}}\frac{v_g}{(V_G - V_{CNP})^2} \quad (4.5)$$

Combining Eqs. (4.4) and (4.5) above, we can rewrite V_G-V_{CNP} as

$$V_G - V_{CNP} = -v_g\frac{R_{dc} - R_{sr}}{R_{ac}} \quad (4.6)$$

Therefore, the carrier density can be written as

$$n = C_G(V_G - V_{CNP}) = -C_G v_g\frac{R_{dc} - R_{sr}}{R_{ac}} = -C_G v_g\frac{V_{AB} - R_{sr}I_D}{v_{ab}} \quad (4.7)$$

and the field effect mobility can be written as

$$\mu^{-1} = -C_G\frac{W}{L}v_g\frac{(R_{dc} - R_{sr})^2}{R_{ac}} = C_G|v_g|\frac{(V_{AB} - R_{sr}I_D)^2}{|v_g|I_D}\frac{W}{L} \quad (4.8)$$

In summary, the transient signals of carrier density and field effect mobility can be evaluated as: $n(t)=C_G/e_c|v_g|(|V_{AB}|-I_DR_{sr})/(|v_{ab}|)$ and $\mu^{-1}(t)=C_G|v_g|(|V_{AB}|-I_DR_{sr})^2/(|v_{ab}|I_D)W/L$.

1.12.2 The preliminary experimental proof of the quasi-static method

Figure 4.3 shows the field effect mobility measurements at various applied DC gate voltages, and the results are independent to the overall V_G modulation as previously reported for the charged impurity scattering effect [62]. Further, the experimental result shows that the carrier density measured at a range of DC gate voltages, where the ratio between n and V_G is constant and agrees well with the linear dependency of $n=C_G|V_G-V_{CNP}|/e_c$, indicating the carrier density is evaluated correctly. The experimental results of the carrier concentration n and the inverse of field effect mobility μ^{-1} of graphene FET measured at a range of quasi-static work functions show good agreement with the theoretical model (dashed lines).

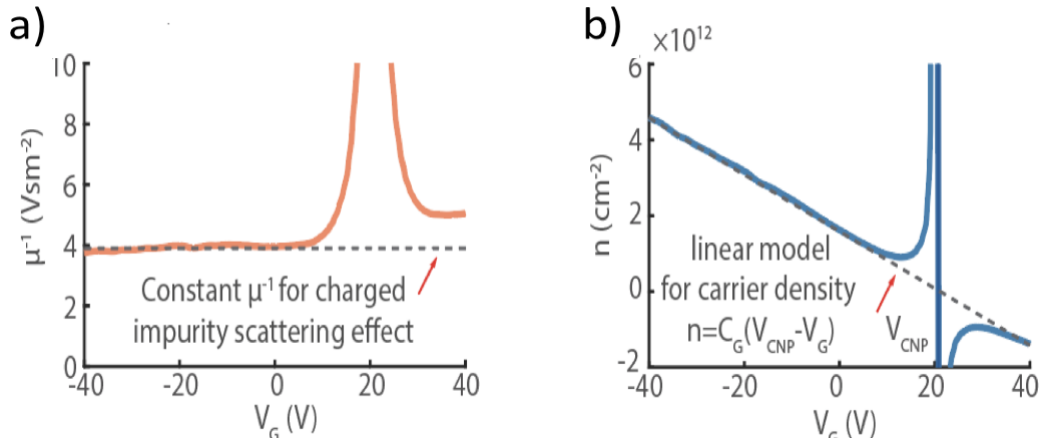

Figure 0.3 Calibration of the measured carrier density and field effect mobility from the hybrid gating method: (a) the measured results for the inverse of filed effect mobility and (b) the measured results for the carrier density.

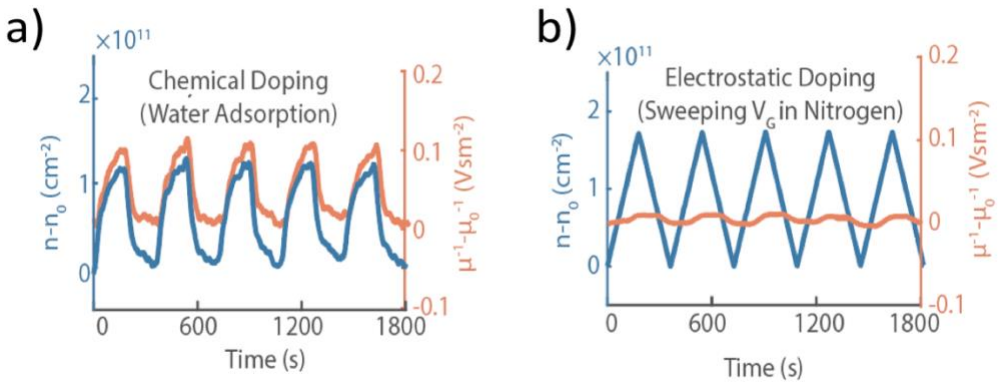

Figure 0.4 Chemical doping v.s. electronic doping: (a) chemical doping using water vapor and (b) electrostatic doping in nitrogen environment

As *n(t)* tracks the doping effect and $\mu(t)$ tracks the scattering effect, we further demonstrate the feasibility of monitoring these two effects under two different doping scenarios: 1) upon chemical doping (water adsorption) as shown in Figure 4.4, both *n(t)* and $\mu(t)$ changed their values due to both doping and scattering effects associated with water molecules adsorbed on graphene; 2) upon electrostatic doping (sweeping V_G in nitrogen) as a clear contrast shown in the electrostatic doping, only *n(t)* was responsive to the electrostatic doping effect by ramping the DC gate voltage V_G in nitrogen, while no additional change in $\mu(t)$ was observed, indicating there was little change in the scattering effect or density of charged impurities on graphene during the electrostatic doping process.

Figure 4.5 shows the gas sensing results using the quais-static method. It is clearly observed that the carrier (holes) density increases upon the adsorption of three p-type doping gases - ethanol, methanol, and water, respectively. For the inverse of field effect mobility, it is observed that $\mu^{-1}(t)$ can both increase or decrease depending on the gas types. In order to normalize the scattering effect associated with individual gas adsorbent on graphene, we introduce the concept of the scattering strength: $S(t)=Ce_c d\mu^{-1}(t)/dn(t)$, where $C=5e^{15}$ $V^{-1}s^{-1}$ is an intrinsic constant of graphene FET [68] to describe the equivalent number of electrons transferred by a gas adsorbent on graphene.

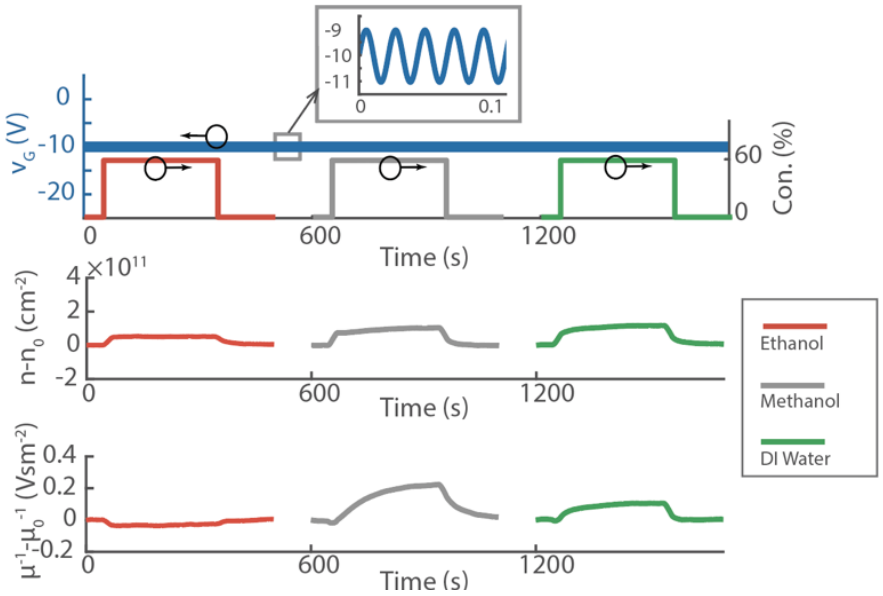

Figure 0.5 Experimental results of carrier density, inverse of mobility, and scattering strength for ethanol (red lines), methanol (grey lines), and DI water (green lines), respectively, using the quasi-static method with a small applied AC bias gate voltage.

1.13 Normalization of the Scattering Effect

In order to normalize the scattering effect of gas adsorbent on graphene, we developed a new concept called scattering strength $S(t)=Ce_cd\mu^{-1}(t)/dn(t)$, to describe the equivalent number of charges per individual gas adsorbents on graphene. Analytically, the adsorption event of p-type dopants onto p-type graphene will help to increase the carrier density of graphene by $\Delta n=Z_{gas}\Delta N_{gas}$, where ΔN_{gas} is the incremental change of gas adsorbent over the unit area on graphene and Z_{gas} is the number of electrons transferred per gas adsorbent. Simultaneously, the inverse of field effect mobility of graphene is changed by $\Delta\mu^{-1}=Z_{imp}^2\Delta N_{imp}/C$ due to the charged impurity scattering effect associated with gas adsorbents [62], where ΔN_{imp} is the induced incremental change of charged impurities density on graphene and Z_{imp} is the number of charges possessed per unit density of charged impurities [68]. Therefore, the scattering strength of a single gas adsorbent can be derived as $S(t)=Ce_cd\mu^{-1}(t)/dn(t)=e_c(\Delta N_{imp}/\Delta N_{gas})(Z_{imp}^2/Z_{gas})$. Here, the ratio of $\Delta N_{imp}/\Delta N_{gas}$ and Z_{imp}^2/Z_{gas} are highly dependent on the adsorption sites on graphene. Previously, it was reported in theory [61], [69] that the scattering effect of charged gas adsorbates on graphene will take a two-step process: firstly to improve the field effect mobility by compensating the oppositely charged impurities, and then to deteriorate the field effect mobility by becoming added scattering centers after oppositely charged impurities are fully compensated. Therefore, the scattering effect we measured is strongly dependent on the charges carried by the gas adsorbents as well as the existing charged impurities on graphene. For example, in the compensation adsorption mode (Figure 4.6), the gas is adsorbed

onto the existing charged impurities (positively charged existing impurities will attract negatively charged gas adsorbents as the preferred adsorption site).

During the compensation adsorption process, the scattering strength of a single gas adsorbent is determined by the neutralization process of the existing impurity as $S=Z_{imp}e_c$, because the number of existing impurity is neutralized by $\Delta N_{imp}=-\Delta N_{gas}Z_{gas}/Z_{imp}$. On the other hand, after existing impurities are fully compensated by the adsorbents, the scattering strength of gas adsorbent adsorbed on pristine graphene is determined by the additional scattering process of the charged gas adsorbent as $S=Z_{gas}e_c$, because the number of charged impurity is increased by $\Delta N_{imp}=\Delta N_{gas}$ with $Z_{gas}=Z_{imp}$. It is important to note that the scattering strength measured within the superposition adsorption process ($S=Z_{gas}e_c$) can be directly used as an indicator of the number of charges carried by single gas adsorbents - a powerful indicator for gas discrimination.

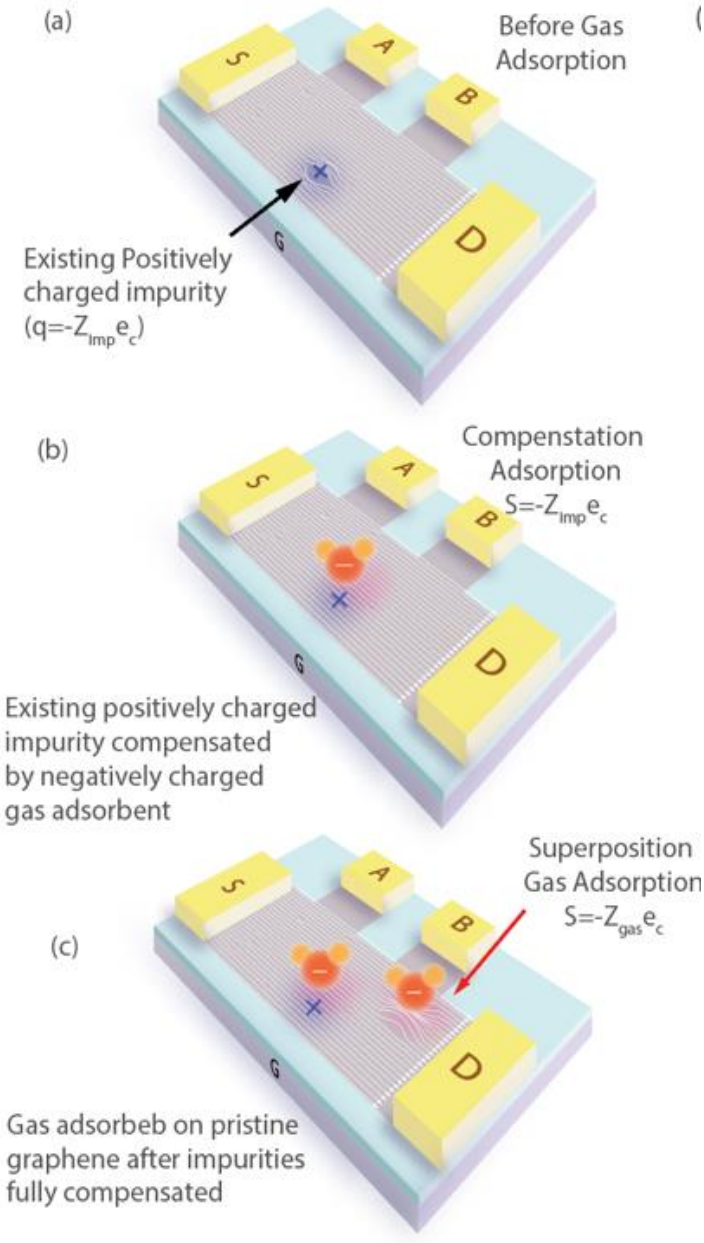

Figure 0.6 Schematic of two adsorption modes (a) before adsorption, (b) compensation adsorption, and (c) superposition adsorption on graphene

Figure 4.7 shows the *transient* plot of the *scattering strength S(t)* and *charging rate density I(t)=dn/dt*, denoted as the TSI plot in this work, for the three gases with the color bar indicating the adsorption (I>0, reddish), the equilibrium (I=0, greenish), and desorption (I<0, blueish) processes. These results reveal important patterns of gas adsorbents in terms of the scattering strength ~ time relationship in the TSI plot which are further studied in this work.

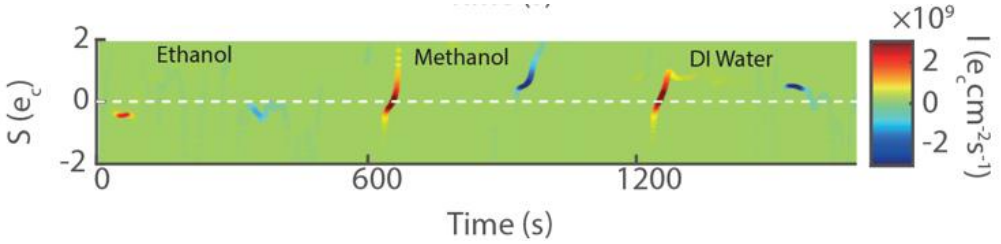

Figure 0.7 Transient scattering strength ~ charging rate plot (TSI) plot

1.14 Experiments

1.14.1 Gas Sensing Chamber Setup

All gas sensing measurements were carried out in a sealed nylon chamber with a waste gas recovery system. High purity nitrogen (>99.998%) from Praxair was used with 4 mass flow controllers (Omega Inc.) to control the total flow rate (300 sccm) and vapor concentration into the camber. Using the split-stream method, the dry nitrogen was divided into two parts: one of these was saturated with chemical vapor by pumping into liquid chemicals (ethanol, methanol and water); the other dry nitrogen was mixed to achieve the desired gas concentration. Finally, the vapor with desired concentration was flowed to the chamber with a constant flow rate. A mass flow meter (Omega Inc.) was used to measure the total flow rate at the waste gas port before each experiment to detect possible leakages in the gas sensing system.

1.14.2 Sensing Signal Conditioning

The DC component of the gate voltage was used to set the carrier concentration in the graphene channel, while the AC component provides an oscillating component of the carrier concentration with a much smaller amplitude (1V) as compared to the DC gate voltage from the Dirac Point. A lock-in amplifier (SR 860, Stanford Research Systems) was used to monitor the voltage v_{AB}. The AC component v_{ab}, at 50Hz, was isolated from v_{AB} through the Fast Fourier Transformation, while the DC component V_{AB} was isolated from v_{AB} by passing through a low pass filter at 5Hz.

1.15 Results

1.15.1 Scattering Strength Measurements

To verify the value of the scattering strength for different adsorption processes, we conducted charge transfer analysis for three p-type dopants ($Z_{gas}>0$): ethanol, water and methanol at various concentrations (from 10% to 90% saturated in nitrogen) with the graphene FET kept at quasi-static work function, and the corresponding $I(t)$ and $\mu^{-1}(t)$) are shown in Figures 4.7 – 4.9, and the TSI plots are shown in Figures 4.10 – 4.12 for the three gases respectively. Similar to our analysis above, we observed all adsorption process ($I(t)>0$, reddish) shown in the TSI plots started from the negative scattering strength for the compensation absorption process

($S=Z_{imp}e_c<0$), indicating the initial stage of gas adsorption is to compensate the existing charged impurities on graphene that is oppositely charged as compared to the p-type gas adsorbents. Then the scattering strength started to become positive as the adsorption process proceeded into the superposition adsorption process ($S=Z_{gas}e_c>0$).

Interestingly, there are different concentrations for the transition point from the compensation to superposition process among the three p-type doping gases: $S=0e_c$ scattering strength first emerged at concentration of 60%, 20%, and 40% for ethanol, water, and methanol vapor, respectively for the same graphene FET device. This might be explained as the amount electrons carried by each gas molecule is different to fully compensate existing charge impurities on graphene. In general, positive scattering strength can be observed for all three vapors for concentrations 60% or higher, indicating the superposition adsorption process was reached. Besides, we further observed the descending *S ~ Time* relationship in the desorption periods for ethanol and water as shown in the representative cycles of Figure 4.11 and Figure 4.12 (white arrows as examples). However, such dependency was reversed for the methanol desorption process as shown in Figure 4.13, where the scattering strength with time relationship was ascending in both the adsorption and desorption processes (white arrows). This can be explained as the methanol molecules adsorbed with stronger scattering strength ($S\sim2e_c$) were more difficult to escape the graphene surface during desorption process as compared to water and ethanol molecules adsorbed with lower scattering strength ($S\sim1e_c$) on graphene[70].

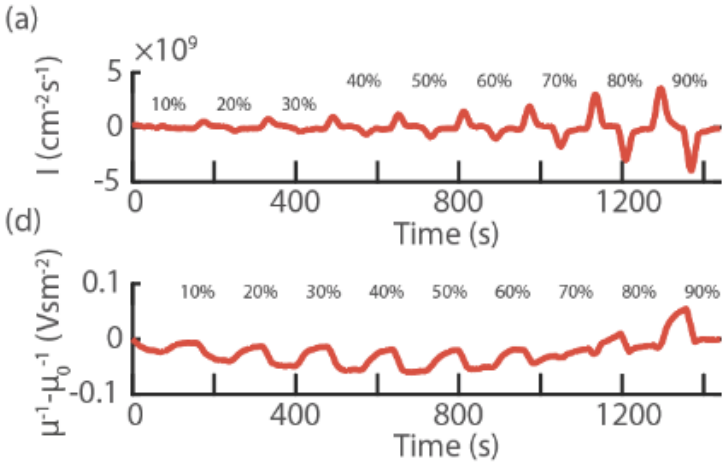

Figure 0.8 Charging rate and the inverse of mobility signals for ethanol vapor: (a) charging rate and (b) inverse of field effect mobility.

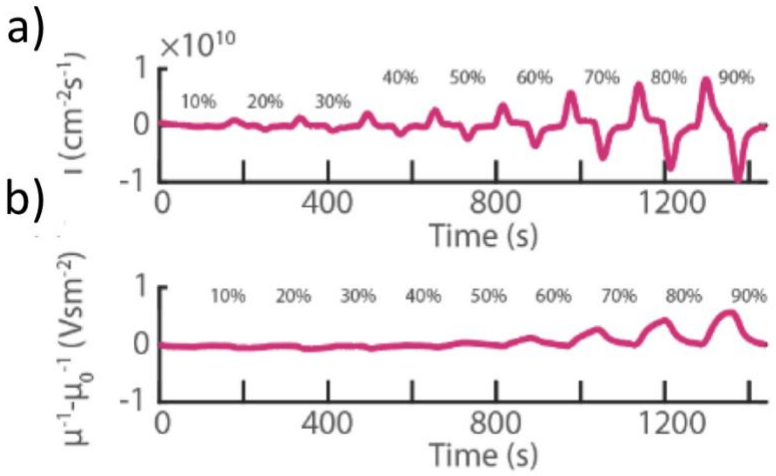

Figure 0.9 Charging rate and the inverse of mobility signals for methanol vapor: (a) charging rate and (b) inverse of field effect mobility.

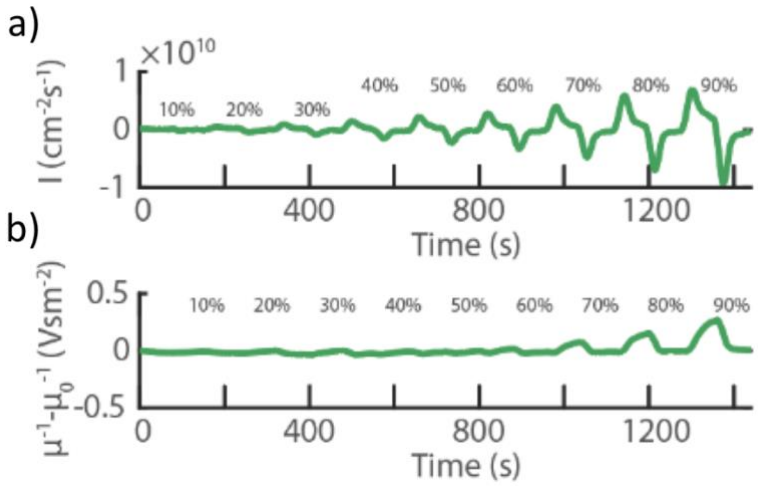

Figure 0.10 Charging rate and the inverse of mobility signals for water vapor: (a) charging rate and (b) inverse of field effect mobility.

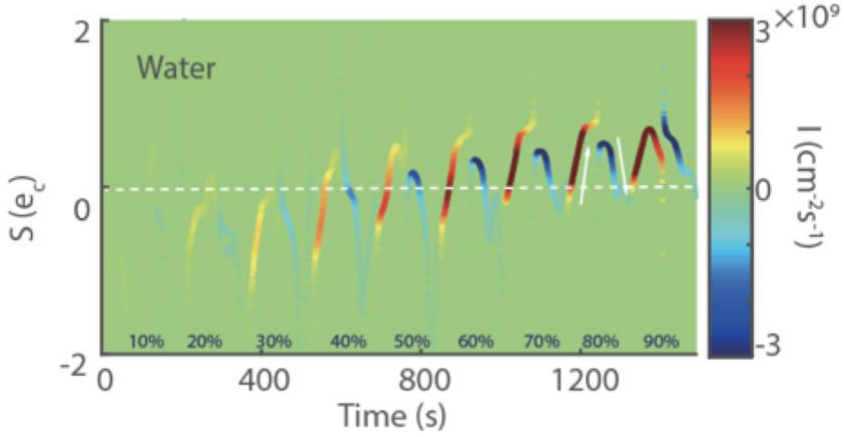

Figure 0.11 The scattering strength of water adsorption and desorption on graphene.

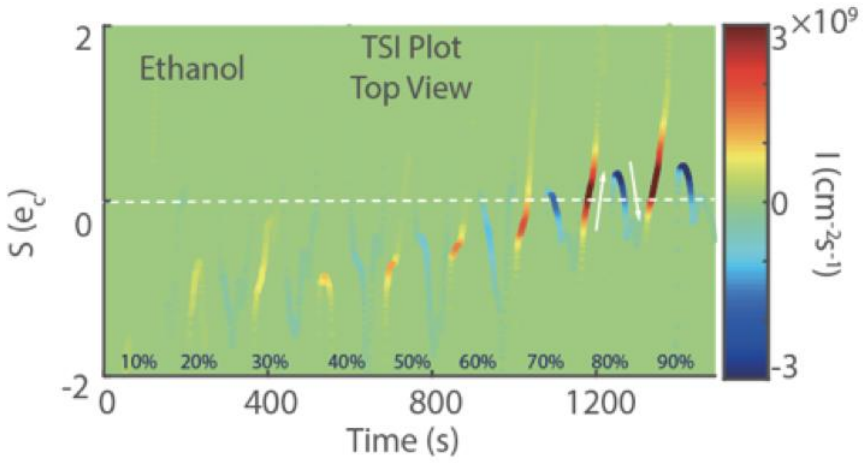

Figure 0.12 The scattering strength of ethanol adsorption and desorption on graphene.

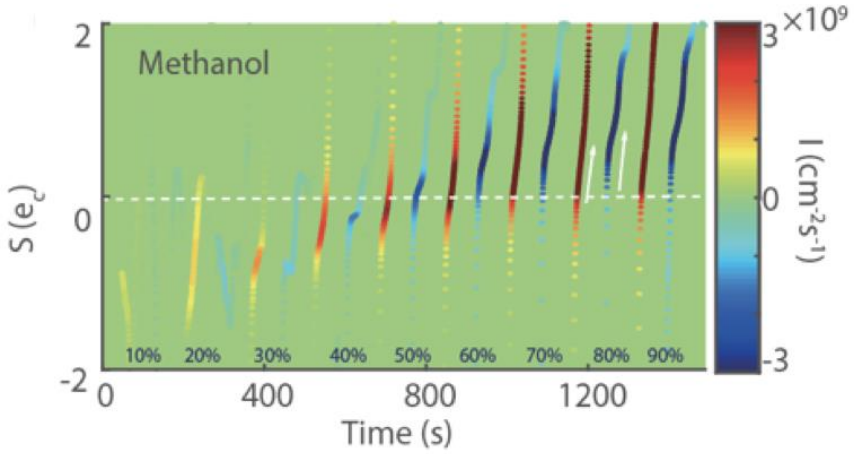

Figure 0.13 The scattering strength of methanol adsorption and desorption on graphene

Nevertheless, we found that measuring the scattering strength of gas adsorbents can help to improve the gas selectivity for graphene FET. As shown in Figure 4.14, we integrated the gas charging speed $I(t)$ over time Δt and divided by ΔS to derive n_S, describing the charge transfer distribution over scattering strength, where the shaded area of the n_S bar plot indicates the amount of total charge transfers during a specific integration period. We compared the corresponding n_S of the scattering strength for the adsorption periods for the three p-doping gases. For example, the n_S of ethanol, methanol and water adsorption at 60% concentration are plotted in Figure 4.15, respectively, where the unique distributions over the scattering strength can be used to differentiate the three p-type doping gases on graphene.

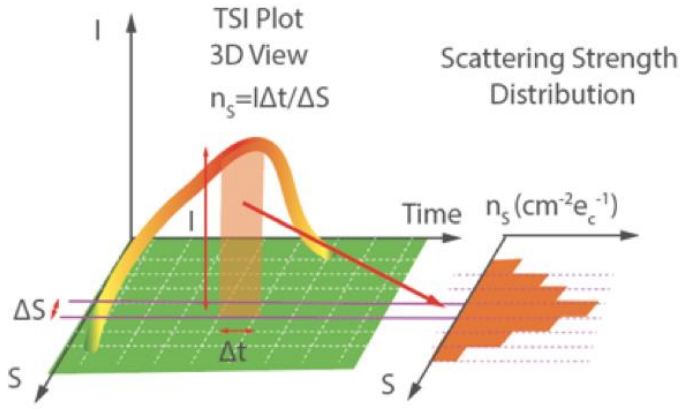

Figure 0.14 Schematic of scattering strength distribution projection scheme.

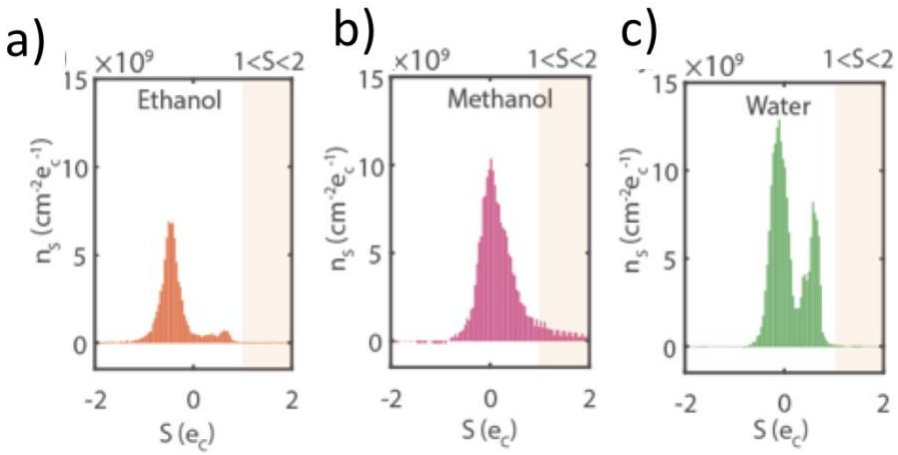

Figure 0.15 Scattering strength distribution for (a) ethanol, (b) methanol and (c) water vapors

For the demonstration of such selectivity over various gas concentrations, we summed the charge transfer amount over the specific scattering strength region as shown in Figure 4.16. We found that the scattering strength region $1e_c<S<2e_c$, denoted as $n_S|_{1<S<2}$, has the maximum selectivity over the three gases. We calculated $n_S|_{1<S<2}$ and plotted such signal dependency with gas concentration in the adsorption period and desorption period in Figure 4.17 respectively. Strong and selective dependency between $n_S|_{1<S<2}$ and the methanol concentration from 40% to 90% can be easily identified as compared to those of water and ethanol, indicating the superior power of the scattering effect in boosting gas selectivity out of a single pristine graphene FET.

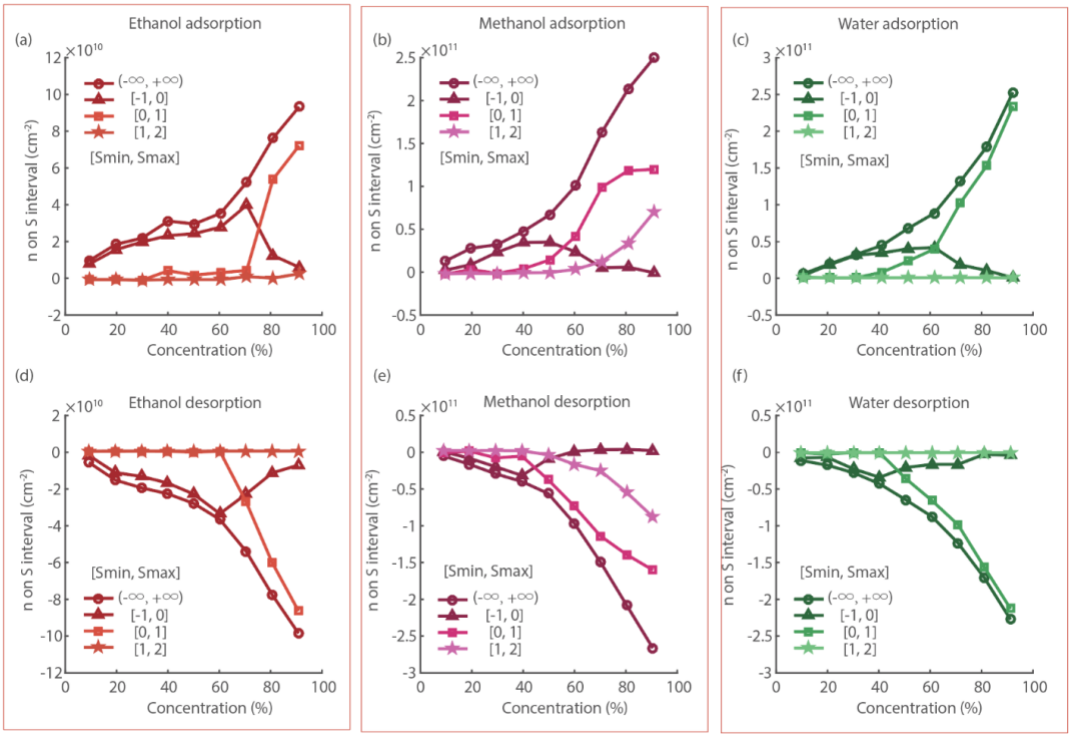

Figure 0.16 Charge transfers summation over specific scattering strength region in the (a) ethanol adsorption period, (b) methanol adsorption period, (c) water adsorption period, (d) ethanol desorption period, (e) methanol desorption period, and (f) water desorption period.

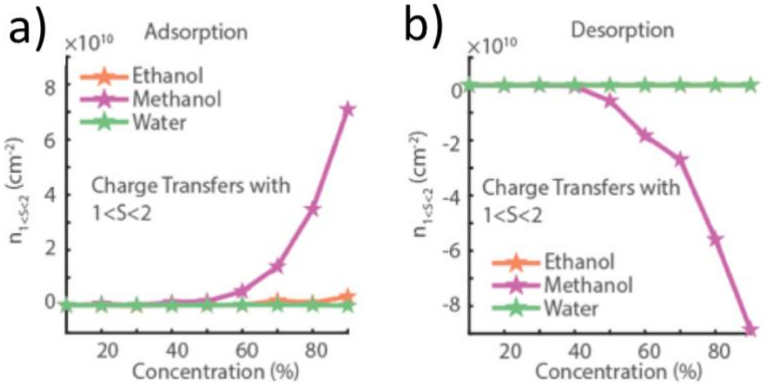

Figure 0.17 nS|1<S<2 under various concentrations within (a) adsorption period and (b) desorption period.

1.16 Discussion

1.16.1 Tuning Gas Scattering Strength on Pre-compensated Graphene

As the origin for compensation adsorption process comes from compensating the existing charged impurities on graphene, we further explored if the impurities can be fully pre-compensated by one type of gas adsorbents such that a second type of gas adsorption process afterwards can be taken as solely superposition adsorption process for the number of charges carried per gas adsorbate. The schematic of pre-compensation scheme is future illustrated in Figure 4.18.

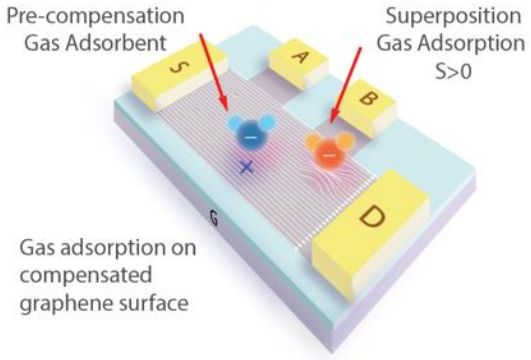

Figure 0.18 Schematic of pre-compensation.

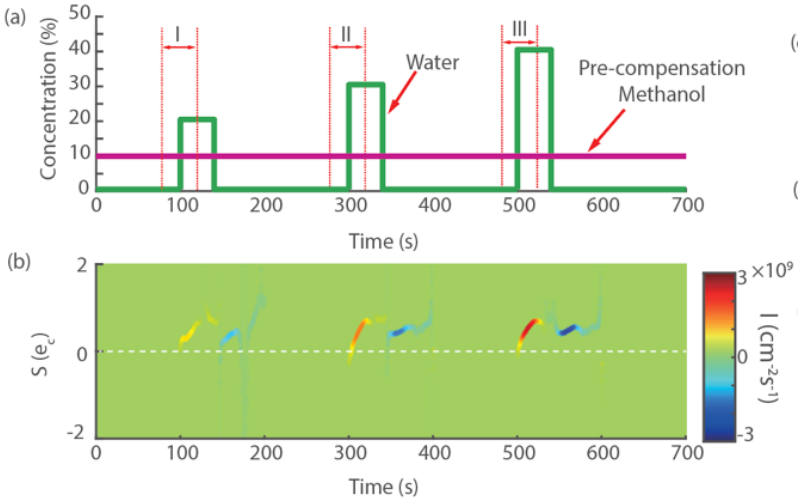

Figure 0.19 Schematic and TSI plot for water adsorption on methanol compensated graphene: (a) schematic of time series, and (b) TSI plot measured

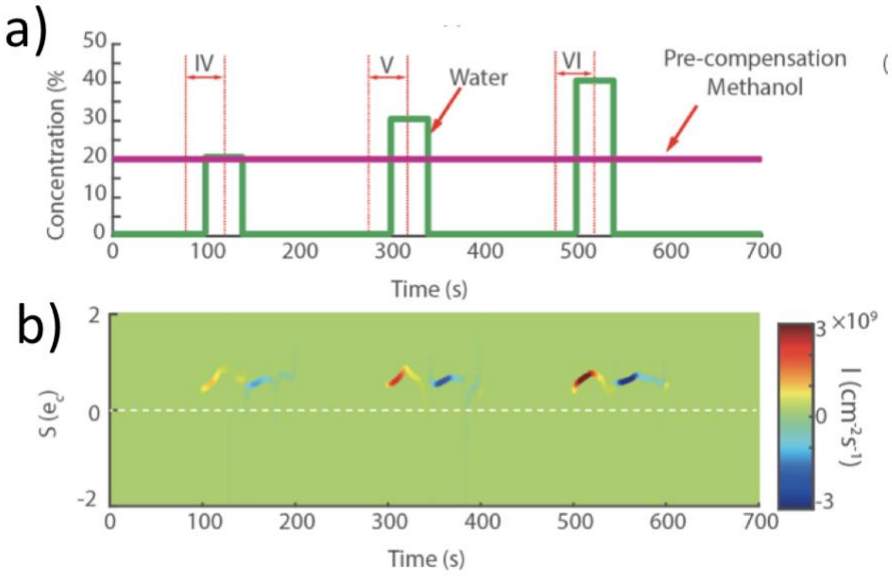

Figure 0.20 Schematic and TSI plot for water adsorption on increasingly compensated graphene: (a) schematic of time series and (b) TSI plot measured

To confirm this, we characterized the scattering strength of water vapor on pre-compensated graphene by different concentrations of methanol. As shown Figure 4.19 and Figure 4.20, the constant pre-adsorbed background methanol with 10% & 20% concentrations, respectively, was tested by increasing water vapor concentrations of 20, 30 and 40%. It is found that the positive scattering strength emerged for low concentration water adsorptions (i.e. 20%) as shown in the corresponding TSI plots, which was not observed previously on pristine graphene. In general, the charge transfers of water adsorption move towards positive direction along the scattering strength axis as the concentration of background pre-compensating gases increases. This implies that the superposition adsorption process can become the dominating adsorption process after the existing charged impurities on graphene are pre-compensated, and the corresponding scattering strength $S = Z_{gas} e_c$ can be directly used to evaluate the number of electrons transferred per gas adsorbent as discussed previously.

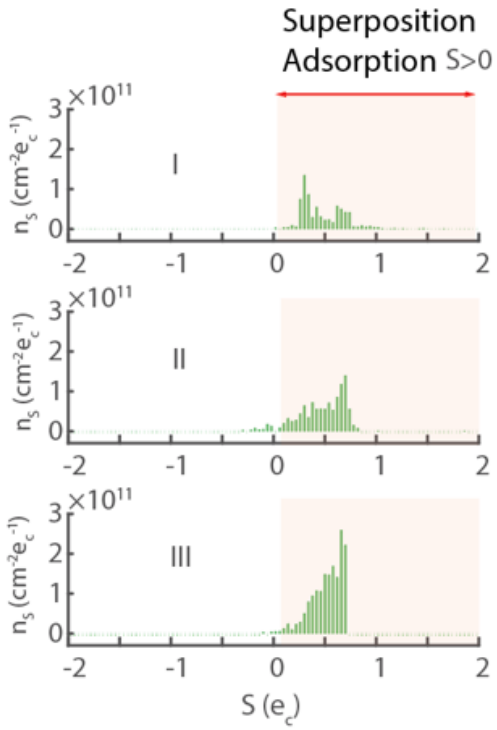

Figure 0.21 Charge ~ scattering strength distribution for the I, II and III adsorption periods in Figure 4.19.

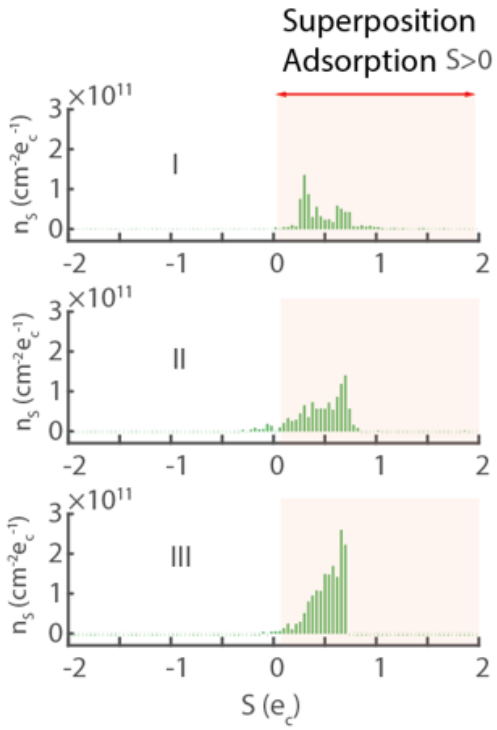

Figure 0.22 Charge ~ scattering strength distribution for the IV, V, VI adsorption periods in Figure 4.20.

Specifically, the charge transfer ~ scattering strength distributions (Figure 4.21 and Figure 4.22) of water adsorption on pre-compensated graphene indicate the number of charges transferred by each unit density of water adsorbents is much larger than that predicted in the first principle simulations of about $0.02e_c$ [65]. This implies that the nature of the water doping on pre-compensated graphene FET is likely electrochemical [71] which is induced by the interactions between water molecule and the oxygen defects/dangling bonds commonly found on graphene-SiO_2 interface. Furthermore, the sums of charge transfers over scattering within the positive scattering strength range of $0e_c<S<2e_c$ are plotted in Figure 4.23 to illustrate the effectiveness of pre-compensation to promote the superposition adsorption process. It is found that pre-compensation with 40% of methanol can result in linear responses of water vapor from 10 to 50% as shown which implies fully-compensated graphene surface to sense linearly the superposition adsorption of water vapor.

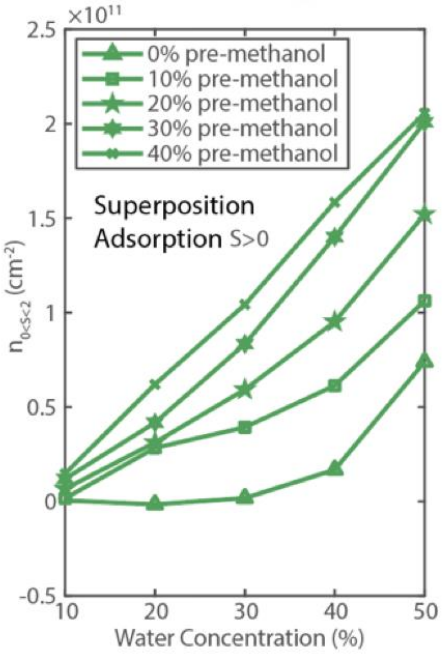

Figure 0.23 n|0<S<2 of water adsorption on various pre-compensated graphene substrate

1.16.2 Tuning Gas Scattering Strength with Graphene Work Function

Besides the modulation of gas scattering strength through the pre-compensation method, we also explored to tune the scattering strength of gas adsorbents using the DC gate voltage V_G, since the electrically tunable work function of graphene is one of the key factors for the charge transfer process [72]. Experimentally, we characterized the dependency between the scattering strength of gas adsorbents and the quasi-static work function of graphene by performing measurements at various DC gate voltages. As the DC gate voltage decreases in the hole branch, the carrier (holes) density of graphene will increase. Analytically, this will results in two opposite dependency of the compensation- and superposition-adsorption process to the DC gate voltage: 1) the scattering strength of the compensation adsorption process $S=Z_{imp}e_c<0$ will increase (reduced amplitude) and approach to zero, because the charged impurities Z_{imp} being screened by more carries and becoming less attractive to the gas adsorbents [73], and 2) the scattering strength $S=Z_{gas}e_c>0$ of the superposition adsorption process will decrease and approach to zero, because the work function of graphene increases and approaches to the work function of the p-type dopants to reduce the work function differences in between. This analysis indicates that the scattering strength of both compensation- and superposition-adsorption processes will be sensitive to the DC voltage tuning, but their dependency to the DC gate voltage tuning is opposite. Furthermore, as the positive scattering strength $S=Z_{gas}e_c$ of the superposition adsorption process is determined by the number of charges carried by the gas molecule, we expect the tuning of

charge transfer with positive scattering strength to be uniquely depending on the gas dopants.

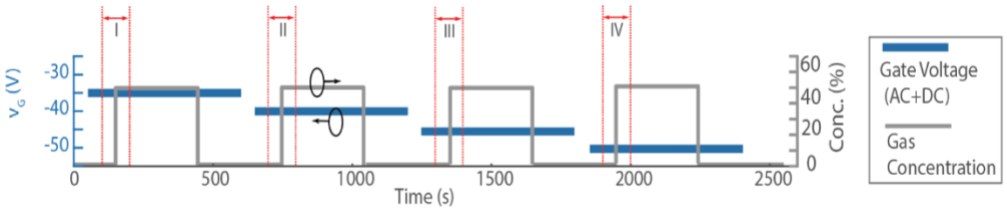

Figure 0.24 Schematic of work function tuning by gate voltage

To verify the change of scattering strength with respect to the DC gate voltage tuning, we sent identical cycles of three gas vapors, methanol (50%), a binary mixture of water (25%) & methanol (25%), and water (50%), onto graphene at 4 static DC gate voltages from -35V to -50V. Here the corresponding DC gate voltage during gas adsorption was labeled as "I"~"IV" in Figure 4.24. As previously explained, we projected the 3D TSI plot of the adsorption process onto 2D charge transfer distribution over the scattering strength n_S by integrating the relationship of $I(t) \sim S(t)$ over time. The distribution of n_S over the scattering strength measured at different DC gate voltages are plotted Figures 4.25 – 4.27, where the relationships between S, V_G and n_S for are recorded, respectively. It is observed that two bulges of charge transfers, likely representing the compensation (left bulge) and superposition (right bulge) adsorption processes, respectively, can be clearly observed for all three types of gases, as highlighted with dash lines using Gaussian distributions and outlined with solid lines for clear illustration. For methanol and the binary mixture in Figures 4.26 – 4.27, the bulges with higher scattering strength (right bulge) gradually shift leftwards as the DC gate voltage decreases, while the bulge with low scattering strength (left bulge) shift rightwards as the DC gate voltage decreases. This right-shift and left-shift behavior of the scattering strength of the superposition and compensation adsorption agree well with the DC gate voltage dependency analyzed above.

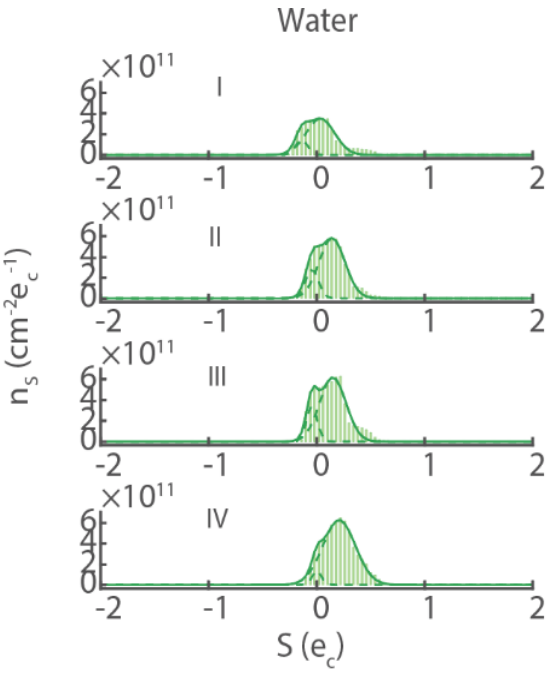

Figure 0.25 Charge ~ scattering strength distribution for water vapor adsorption

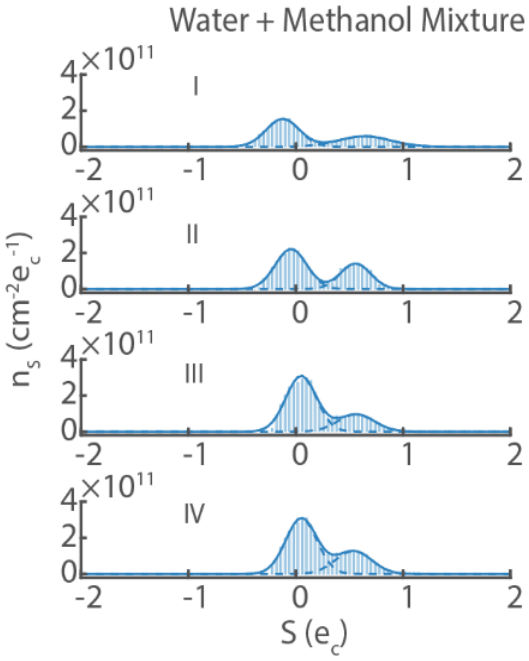

Figure 0.26 Charge ~ scattering strength distribution for methanol and water vapor mixture.

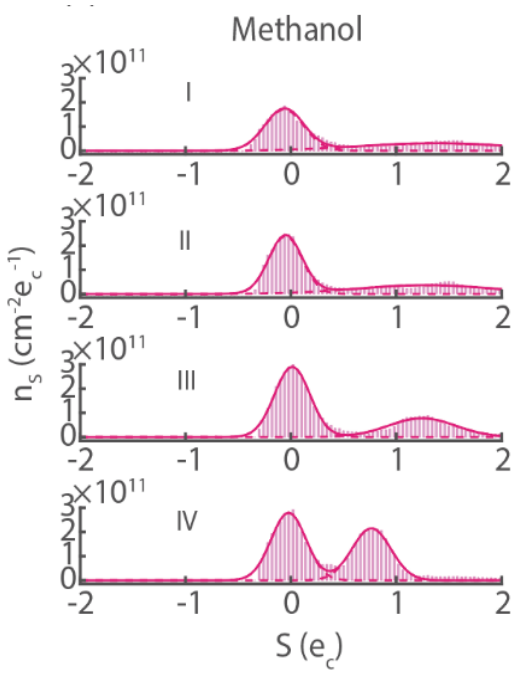

Figure 0.27 Charge ~ scattering strength distribution for methanol vapor adsorption.

To analyze the results, the scattering strength of the left and right bulge at various DC gate voltages fitted through Gaussian Distribution for water (50%), water (20%) + methanol (25%), and methanol (50%) adsorption, respectively, and we plotted the results in Figure 4.28 with the error bar indicating the range of *S* within 90% confidence. The results for water vapor (Figure 4.25) have similar trends but difficult for visual inspections. The results also show that the charge transfer bulge of methanol associated with the superposition adsorption is more sensitive to the DC gate voltage bias than that of water. Qualitatively, we also compared the diagram of the density of state of graphene (left), and the redox system (right) in Figure 4.29, where the work function of graphene can be tuned around 0.2eV by the gate voltage (0-50V). We adopt the Gaussian density of state (DOS) as described previously to model the charge transfer complex between the vapor adsorbates and graphene [74], and calculate the charge transfer strength between graphene and the redox pair over a range of gate voltage offset (assume σ=8kT E_{fv}=4.9eV). The calculated number of electrons transferred (per unit area) between the redox pair and graphene at specific gate voltage bias (V_{CNP}-V_G) is shown in Figure 4.30, where V_{CNP} is the voltage of the Charge Neutral Point (Dirac Point). The scattering strength associated with the superposition adsorption (right bulge) from calculation is in qualitative agreement with the experimental results of methanol, a reasonable value within the range of 4.8~5.6eV as previously reported redox of hydroxyl group on the surface of graphene[68],[67].

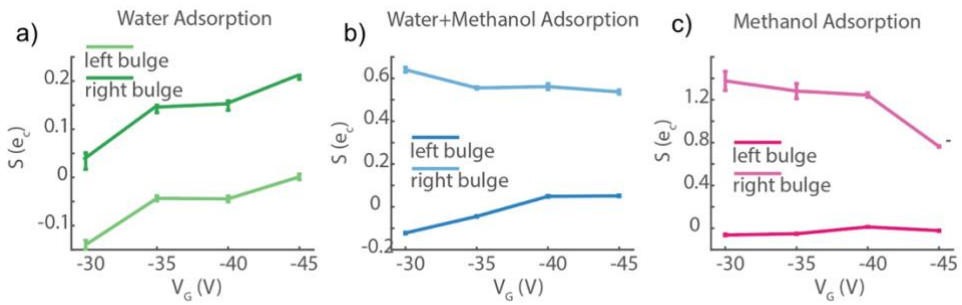

Figure 0.28 Bulges position extracted from the charge ~ scattering strength distribution: (a) water, (b) water + methanol mixture, and (c) methanol

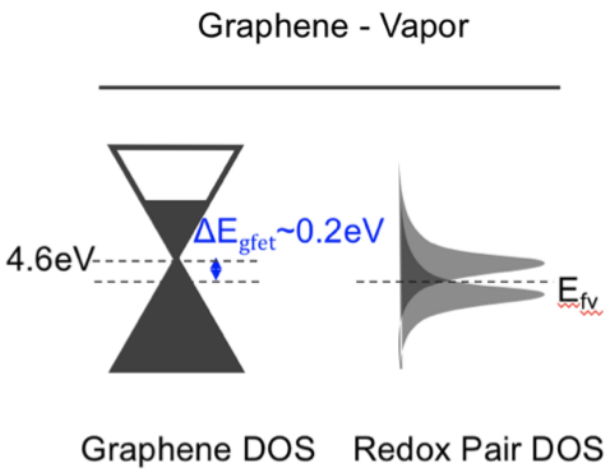

Figure 0.29 Band diagram of graphene and redox pair system

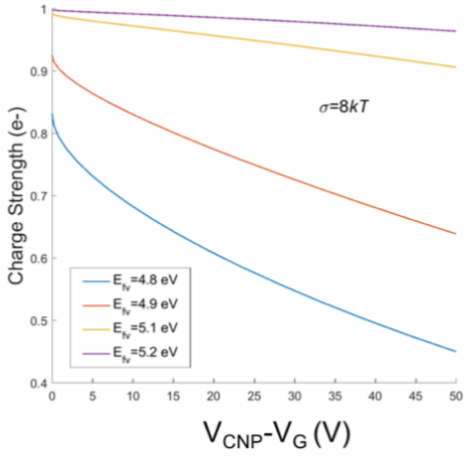

Figure 0.30 The calculated charge transfer per molecule

1.17 Conclusion

In this chapter, we introduced a new method to conduct transient charge transfer analyses on graphene at quasi-static work function with a fixed DC gate voltage under small AC voltage modulations, and explored the scattering effect of gas adsorbents during the transient adsorption and desorption processes. A new terminology called "scattering strength" is introduced to normalize the scattering effect associated with single gas adsorbent, and we found it to be strongly dependent to both the gas types as well as the graphene properties including adsorption sites and work function. We observed interesting patterns in the 3D plot of the transient scattering strength v.s. charging rate density (the TSI plot) during gas adsorption and desorption and provide detailed analysis of the possible origins of the patterns. These findings reveal new opportunities to design gas sensing platform using the charged scattering effects on graphene for selective characterization. Nevertheless, the measurement approach proposed in this work can be readily applied to other gas types for characterizing their charge transfer process, scattering strength, and reaction speed on graphene.

Phase Sensitive Technique on Graphene Gas Sensor

In this chapter, we proposed a phase sensitive method to measure the charge transfer speed of gas-graphene interaction pair. Not only such phase based method can provide fundamental understanding of the limiting factor of the charge transfer process in terms of reaction speed, but also it provides new insights into improving the response and recovery speed of the graphene gas sensor. The chapter lays the foundation for understanding the application side of the phase sensitive method to be introduced in Chapter 6.

We organize this chapter in the following manner. Section 5.1 give the general introduction and motivation, and Section 5.2 describes the concept of sensing charge transfer in AC mode on a GFET. Section 5.3 presents the fabrication, electrical setup, and section 5.4 provides the characterization results, as well as the gas sensing results. Section 5.4 also compares the response speed between the phase sensing signals and the DC resistance signals, for water vapor. Section 5.5 further discusses the advantage of AC operation in resolving multiple stage of charge transfer processes through in-situ measurements of the field effect mobility and DC carrier concentration on the GFET.

1.18 Introduction

Most GFET gas sensors, when made from the chemical vapor deposition (CVD) method and transferred on a SiO_2 substrate, bear a practical problem of slow charge transfer speed. This is typically limited by the large time constant of a particular charge transfer process. As a result, the sensing signal of the DC electrical resistance can only reset slowly. Usually, it takes more than 1000s for the signals to fully stabilize between each run. This issue is likely due to charge trapping and releasing from the unintentional defects found on the graphene. These defects, or trap states, can have multiple origins from the fabrication process, including cavities on graphene from the CVD growth process, contamination of the graphene from the substrate, and dangling bond at the edge of the graphene from the etching process **Error! Reference source not found.**. To address this issue, several previous efforts were made to speed up the desorption of trapped gases by UV exposures **Error! Reference source not found.**, and to reduce the trap states by improving the interfacial quality between graphene and substrate **Error! Reference source not found.**.

In this work, we propose a phase sensitive approach to probe the charge transfer time constant associated with gas adsorption on graphene: Instead of measuring the DC resistance that is vulnerable to trap states, we used the highly stable phase change of the charge transfers as the new sensing signal. We found that the phase of the charge transfers process on the graphene surface, driven by the applied AC

gate voltage inputs, can collect full spectrum of information associated with both the fast (pristine state) and slow (trap state) adsorption/charge transfer process.

1.19 AC Sensing of Charge Transfer on A GFET

The overall carrier (charge) concentration n_{GFET} of a GFET gas sensor is collectively determined by three parts at a given time: $n_{GFET}= n_G+ n_C+ n_T$, where n_G is the electrostatic charge associated with gate voltage; n_C is the electrochemical charge associated with reactive gas adsorption; and n_T is the trapped charge associated with trap state. In principle, all charges have their DC component (N_{GFET}, N_G, N_C, N_T) and AC component (n_{gfet}, n_g, n_c, n_t). The goal is to filter out n_t through the modulation of gate voltage v_G. At a proper frequency, the gate modulation will allow n_g and n_c to follow but quench n_t, making the AC sensing signal immune to the trap states. After some initial studies and measurements, the phase component of n_{gfet}, $\phi(n_{gfet})$, is chosen as a representative AC sensing signal for its superior stability.

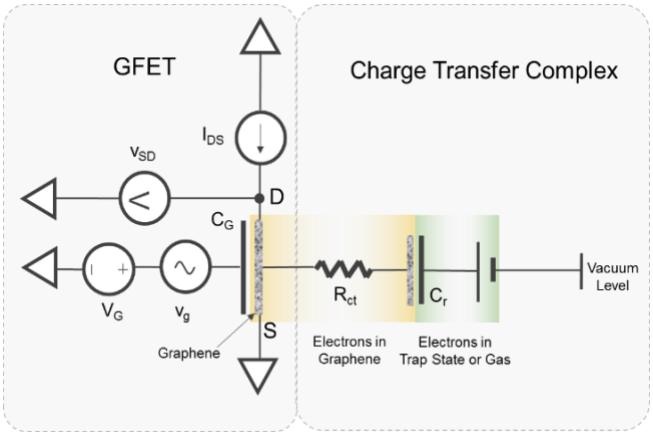

Figure 0.1 Schematic of the charge transfer process on graphene.

To further illustrate the sensitivity of $\phi(n_{gfet})$ towards gas concentration, we adopt the RC model of Faradic process **Error! Reference source not found.** to analyze the charge transfer process on GFET as shown in Figure 5.1. With n_t quenched, the overall phase $\phi(n_{gfet})= \phi(n_g+n_c)$ will approach to $\phi(n_c)$ as the gas concentration increases - $|n_g|=C_G|v_g|$ where C_G being the gate capacitance. In the experiment, the phase signal $\phi(z_{sd})$ was measured as the equivalent signal of $\phi(n_{gfet})$, where z_{sd} is the AC component of the impedance between the source and drain electrodes z_{SD}. All the symbols used in this work are denoted in Table 5.1.

Table 0-1 Symbols Used in this chapter

Symbol	Description
n_{GFET}	Overall charge concentration of a GFET gas sensor
N_{GFET} & n_{gfet}	DC and AC component of n_{GFET}

Symbol	Description
n_G	Electrostatic charge associated with gate voltage
N_G & n_g	DC and AC components of n_G
n_C	Electrochemical charge associated with reactive gas adsorption
N_C & n_c	DC and AC components of n_C
n_T	Trapped charge associated with trap state
N_T & n_t	DC and AC components of n_T
v_G	Gate voltage
V_G & v_g	DC and AC component of v_G
v_{SD}	Source and drain voltage
V_{SD} & v_{sd}	DC and AC component of v_{SD}
i_{SD}	Source and drain current
I_{SD} & i_{sd}	DC and AC component of i_{SD}
C_G	Gate capacitance
z_{SD}	Impedance between the source and drain electrodes
Z_{SD} & z_{sd}	DC and AC component of z_{SD}
μ_h & μ_e	Field effect mobility of hole and electron
$\phi(X)$ & $\|X\|$	Phase and amplitude of an AC signal X

1.20 Experiment Setup

1.20.1 Characterization of GFET with AC Modulation

The admittance between the source and drain electrode, $1/z_{SD}$, was characterized with electron carrier and hole carrier under a nitrogen environment (setting n_C to zero). To switch the carrier polarity, the gate voltage v_G was biased with a DC voltage VG (-50~50V) and an AC small voltage |vg|=1V (peak-to-peak) in serial. We chose the modulation frequency at 50Hz in order to fit in the time constant in charging the gate capacitance (~us) and the gas adsorbates (~ms), and filter out the time constant of trap state (~s). As shown in Figure 5.2, the overall profile of the admittance $1/z_{SD}$ between the source and drain electrode has a "V" shape separating the curve into two parts at the point of minimal conductance (Dirac Point), with the electrical current of the left part carried by holes and the right part carried by electrons. Two regions from each carrier regime were further highlighted: $1/z_{SD}$ oscillates with vg in an opposite manner, while it follows in phase with vg when the carrier in graphene switches from hole to electron. It is important to note that there was a drift in the profile of $1/z_{SD}$, which was likely due to the charging process of the trap states driven by the sweeping V_G.

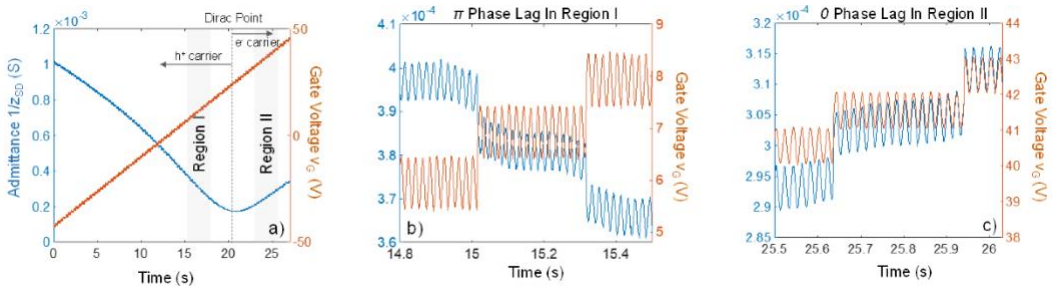

Figure 0.2 Admittance ~ time with hybrid gating scheme: (a) overview across V_G, zoom-in for region I and (c) zoom in for region II

1.20.2 The Stability of Phase Signal ϕ(zsd)

With both AC voltage vg and DC voltage VG applied on the gate, multiple electrical parameters can be measured simultaneously, including the AC impedance $z_{sd}=v_{sd}/i_{sd}$, the DC resistance $Z_{SD}=V_{SD}/I_{SD}$, the DC carrier concentration $N_{GFET}=C_G v_g Z_{SD}/z_{sd}$, as well as the field effect mobility μ. As shown in Figure 5.3, $\phi(z_{sd})$ stabilized at 0 consistently when V_G was between 0V to 25V and jumped to 180 after V_G passing through the Dirac Point (25V), while $|z_{sd}|$ shows a highly nonlinear dependency with V_G. Figure 5.4 illustrates the dependence of the field effect mobility ($1200cm^2/Vs$ for holes and $900cm^2/Vs$ for electrons) and DC carrier concentration with respect to V_G, respectively, where both quantities inevitably diverged from their physical value as z_{sd} vanishes to zero near the Dirac Point.

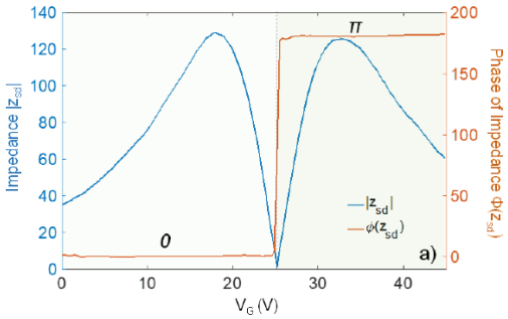

Figure 0.3 Impedance magnitude (blue line) and phase (red line) vs gate voltage results.

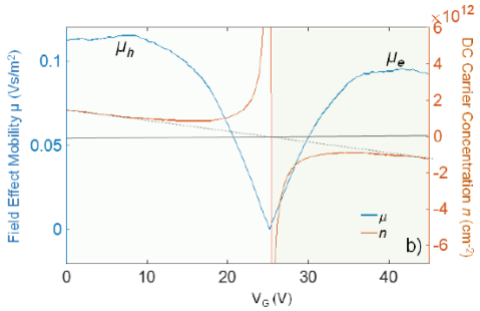

Figure 0.4 Mobility (blue line) and carrier density (red line) vs. gate voltage testing results.

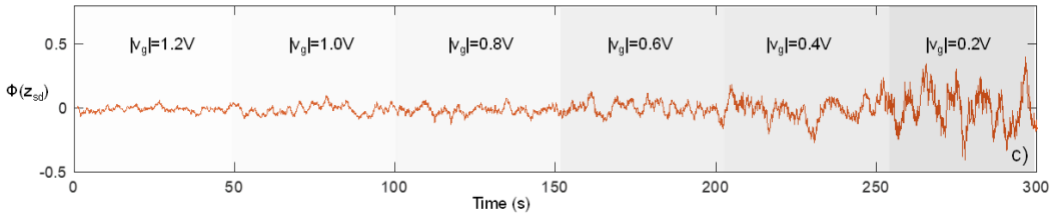

Figure 0.5 Phase stability under various AC gate voltage vs time.

Among these signal candidates for gas sensing, it is found that the phase signal $\phi(z_{sd})$ demonstrated the highest level of stability over V_G tuning and immunity over disturbance from the trap states, therefore we further adopted $\phi(z_{sd})$ as the primary sensing signal in the subsequent sensing event. As expected, even under the influence of a trap state, the phase signal $\phi(z_{sd})$ was only responsible to the charge modulation from the gate electrode and maintained steadily at either 0 or 180, indicating the effectiveness of rejecting the slow charge transfer process with trap state at 50Hz. Furthermore, we found that the SNR of the phase signal in our setup is highly related to the amplitude |vg| as shown in Figure 5.5, therefore we chose $|v_g|$=1V to achieve a measurement noise within 0.2 degree of phase without sacrificing the small signal nature of v_g.

1.21 Results

The gas sensing experiment was carried out by sealing the GFET in a custom-built nylon chamber (1mL), and injecting the moisture vapor at various relative humidities (RH) at a constant flow rate (200sccm). A nitrogen flow (200sccm) was

used to purge away the residual moisture vapor in the recovery stage of the GFET sensor. As shown in Figure 5.6, there were three consecutive periods in a moisture sensing event: GFET exposure to nitrogen (t=0-10s), to RH=60 vapor (t=10-225s), and to nitrogen (t=225s-320s).

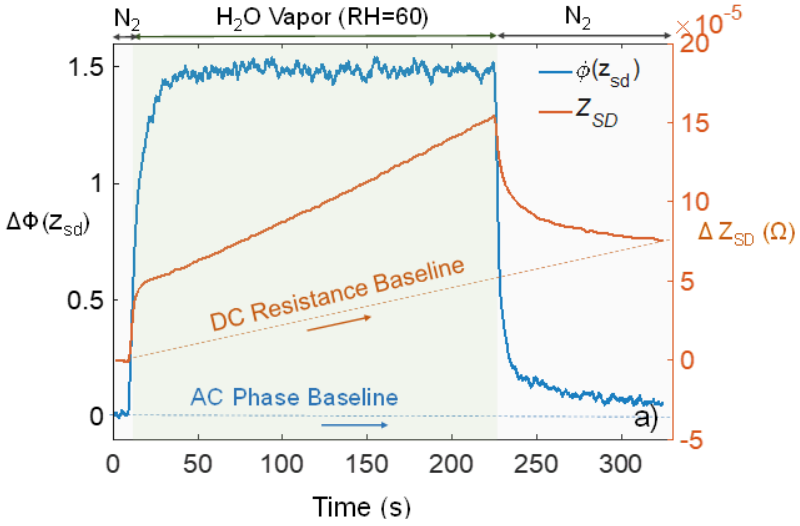

Figure 0.6 Phase signal v.s. resistance signal in gas sensing

By comparing the transient response of the conventional DC resistance signal Z_{SD} and the AC phase signal $\phi(z_{sd})$ in these three stages, two striking differences were found: 1) the phase signal $\phi(z_{sd})$ quickly saturated in moisture vapor starting at t=50s, while the DC resistance signal Z_{SD} kept drifting at a relative constant speed over the second stage; 2) the phase signal $\phi(z_{sd})$ recovered to its baseline within the first 100s after introducing nitrogen into the chamber, while the Z_{SD} failed to recover within the same period. We believe both the slow drift and the stagnant recovery of Z_{SD} was caused by the charge N_T associated with trap states. It is worth noting that the DC resistance signal Z_{SD} was able to recover to its original baseline after sitting in nitrogen flow overnight. We also characterized the sensitivity of $\phi(z_{sd})$ towards different RH levels, and found that the amplitude of phase change was indeed sensitive to the concentration of water vapor in the range of RH=10-60 as shown in Figure 5.7.

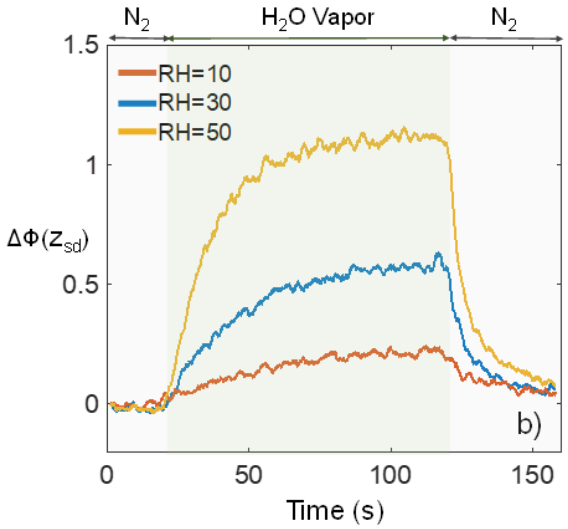

Figure 0.7 Phase signal in sensing gas concentration.

1.22 Discussion

The AC impedance measurement in the GFET gas sensor offers many advantages over the DC resistance signal. Besides the immunity to trap state mentioned above, one of the other advantages is that it enables the in-situ reading of field effect mobility μ and DC carrier concentration N_{GFET} in high definition of time. Previously, the linear slope of the N_{GFET} versus μ^{-1} plot was used to label the charge transfer process from different parties **Error! Reference source not found.**, **Error! Reference source not found.**. Here we used the same method to demonstrate the power of AC sensing by revealing multiple hidden stages of the charge transfer processes embedded in the moisture sensing result.

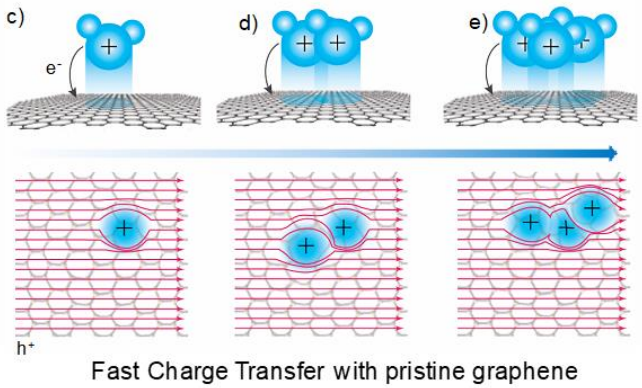

Figure 0.8 Schematic of fast charge transfers.

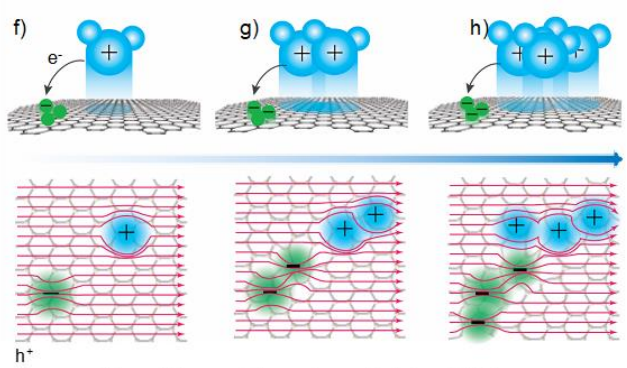

Figure 0.9 Schematic with slow charge transfers.

We plotted the different carrier scattering process when 1) charges are directly transferred from gas molecules to graphene (Figure 5.8), and 2) charges are transferred from gas molecules to trap states (Figures 5.9). Figure 5.10 shows the high resolution (dt=0.1s) transient response of the field effect mobility μ and the DC carrier concentration N_{GFET} measured from the same run shown in Figure 5.6. Multiple peaks and valleys emerged in the two curves in the period of t=10-320s, which were further broken and labeled into five linear slopes in Figure 5.11. For stage I during t=10-12s, we believe the quick jumps of μ and N_{GFET} were due to the rapid changes of the electrostatic screening environment when introducing water vapor in contrast to the nitrogen background. For stage II during t=14-30s, direct charge transfer (p-type doping) between adsorbed water molecule and graphene took place, followed by the charge transfer (n-type doping) between adsorbed water molecule and trap state in stage III (t=30-225s). Obviously, the charge transfer in stage III had a slow but profound impact on μ and N_{GFET}, and it shaped the slope of N_{GFET}- μ^{-1} plot into a dramatically different direction compared to that of stage II. After nitrogen was introduced at t=225s, the water molecules started to desorb. In stage IV (t=225-228s), water molecules that interacted with graphene were fully desorbed from the surface of graphene, while in stage V (t=228-320s), the water molecule that interacted with the trap states were desorbed partially. We further verify that the stages II & IV and stages III & V were of the inverse process pair by plotting the ΔN_{GFET} versus $\Delta\mu^{-1}$ curve in the inset of Figure 5.11, showing each pair sharing similar slope but opposite direction. Interestingly, the inverse process of stage I (screening effect of water molecules on graphene) was missing in the plot, and this was probably due to the fact that there were still water molecules adsorbed on graphene at t=320s.

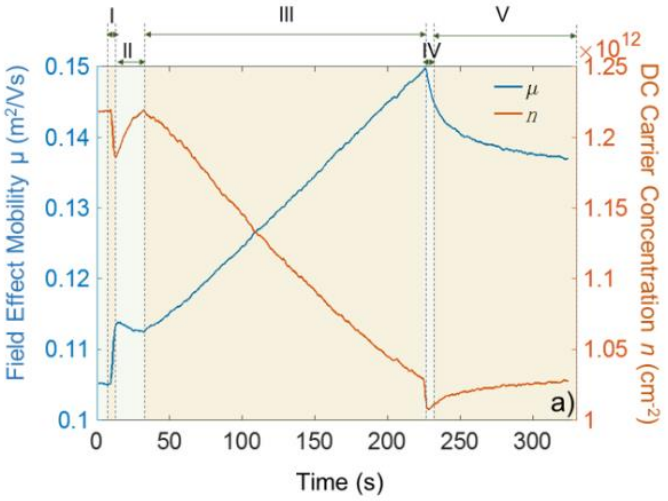

Figure 0.10 Field effect mobility v.s. carrier density signal in gas sensing.

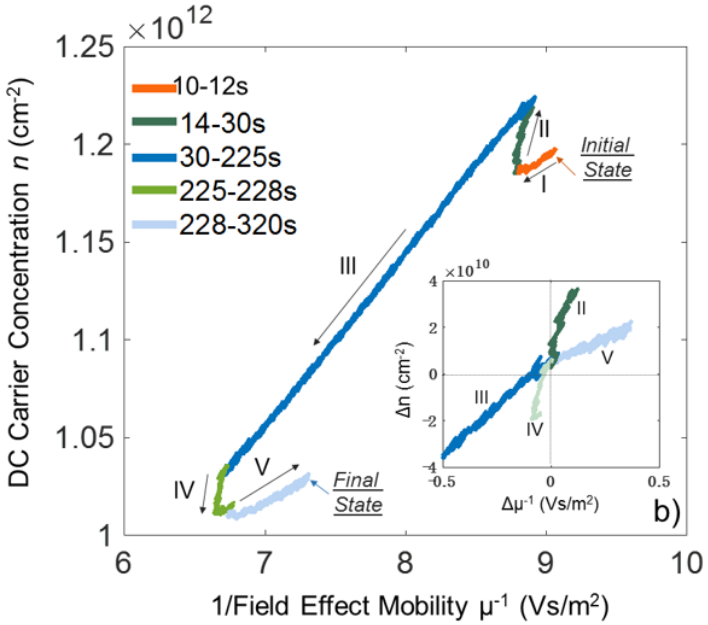

Figure 0.11 XY plot for the inverse of field effect mobility (X) and carrier concentration (Y).

1.23 Conclusion

To sum up, we provided the experimental procedure for the phase based gas sensing solution on graphene transistor, and explained the origin (trap state) of slow recovery found in most GFET gas sensor made from CVD method. Through the experiments with water vapor, we demonstrated that the AC phase signal $\phi(z_{sd})$ of GFET gas sensor featured a faster saturation and recovery speed over the conventional DC resistance signal Z_{SD} due to its immunity to trap state, and further take advantage of the in-situ measurement of field effect mobility μ and DC carrier concentration N_{GFET} to reveal multiple stages of charge transfer in the plot of N_{GFET}-μ^{-1}.

Nevertheless, we observed the SNR of the phase signal was not comparable to that of the DC resistance in our results. We believe this is probably due to the nature of our algorithm to extract $\phi(z_{sd})$ used in the current setup. We are now working on the improvement of the AC approach on the GFET to reach the full potential of ultrahigh sensitivity in gas detection with the phase sensitive method.

Phase Sensitive Technique for Low Baseline Drift

In this chapter, we leveraged the phase sensitive method introduced in Chapter 5, and applied such technique into the applications of boosting the recovery speed of graphene transistors. The motivation of boosting the recovery speed is due to the two key problems of the conventional resistance-based or DC sensing scheme on graphene: (1) the drift issue or the so-called "poison effect", coming from the molecules bonded with the material and difficult to go away. This effect causes the baseline drift of chemical sensors. (2) The slow chemical responses may require a long time to reach steady state. Here, we propose to use the phase signal to reach and sense molecules in the far field of the surface where the molecule-surface interaction is intrinsically weak – easily for gas to come and go for fast sensing responses. Furthermore, since sensing happens away from the surface, the molecules attached to the surface or "poison effect" no longer affect the sensing results to solve the problem of drift. Finally, we extended the discussion of phase sensing at single AC frequency of gate voltage into a spectrum of frequencies and explored the interesting phase ~ frequency patterns measured from several gases.

1.24 Introduction

In this present study, we reported AC phase sensing approach in contrast to the conventional DC resistance sensing for minimal baseline drift and fast responses as illustrated in Figure 6.1. To alleviate the problems stemming from the trap states and defects on graphene, this new scheme takes the advantages of the reversible and stable phase change signals instead of DC resistances. As shown in Figure 6.1, the phase lag between the channel resistance (point A and B between the source and drain of the FET) and the gate voltage is detected when an AC gate voltage at a moderate frequency is applied. Experimental results show the phase lags of different vapors under various concentrations have fast recovery speeds in the ranges of 10-seconds, which are at least 10 times faster than those of DC resistance results with similar setups. Furthermore, the dynamic response of the phase lag is reversible with large dynamic range while the DC resistance tests suffer from baseline drift problems. Figure 6.2 illustrates the key differences between the AC and DC domain measurements, where the AC phase lag results are sensitive to the weak adsorption of vapor molecules above a distance to the graphene surface for fast gas adsorption and desorption processes while the DC resistance results are sensitive to the strong adsorption and desorption process close to the graphene surface. These observations and analyses are explained by an analytical model with good match to the measurements.

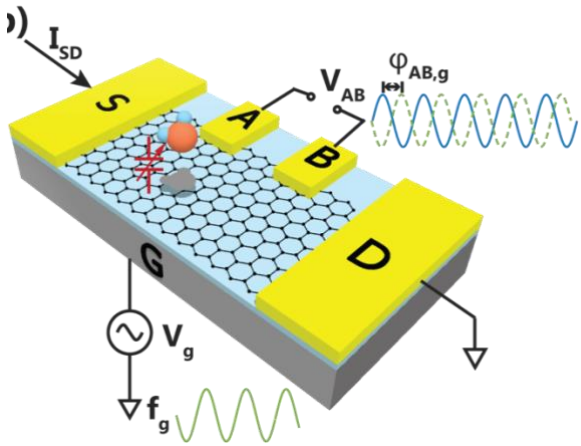

Figure 0.1 Schematic of the phase sensing setup on graphene.

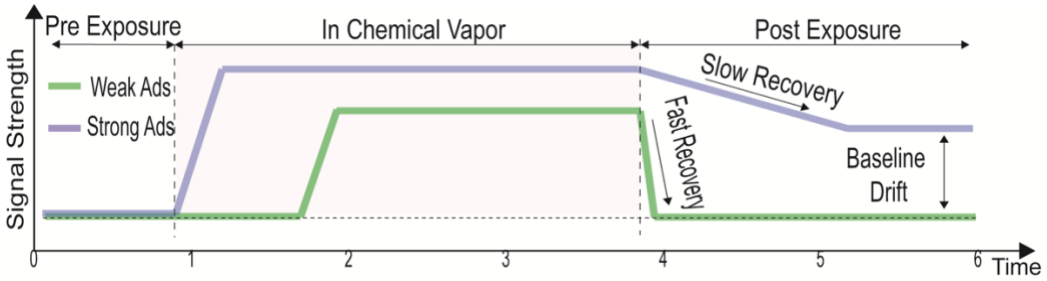

Figure 0.2 Signal comparison between phase and DC resistance signals.

1.25 The Phase of Charge Transfer

Figure 6.3 illustrates the schematic of the sensing principle. Each molecule-surface interaction pair is modeled as a DC voltage source (molecule) and an AC voltage source (sensing surface) connected by a serial of charge transfer capacitor and charge transfer resistor. For simplicity, the charge transfer resistance $R(d)$ is approximated as the tunneling resistance, which scales with distance d exponentially; while the charge transfer capacitance $C(d)$ is approximated as parallel plate capacitance which scales with the reciprocal of distance d^{-1} linearly. As such, the molecule-surface charge transfer time constant $\tau(d)=C(d)R(d)$ varies monotonically with respect to the molecule-surface distance d. As such, the overall phase response is only dominated by a slack of molecules within certain range of distance from the sensing surface. The molecule number profile $c(d)$ is not even, and the phase of charge transfer current $\Phi(\omega,d)$ is proportional to the gas concentration (molecule number) at distance d. Therefore by sweeping the gate modulation frequency ω and monitor the overall charge transfer current, a 3D map of molecular number at different distance can be derived through the overall phase response $\Phi(\omega,d)$.

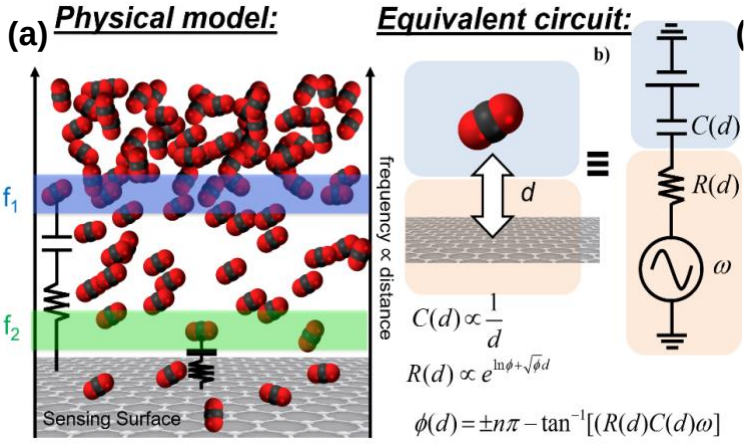

Figure 0.3 The schematic of distance dependent RC time constant of charge transfer.

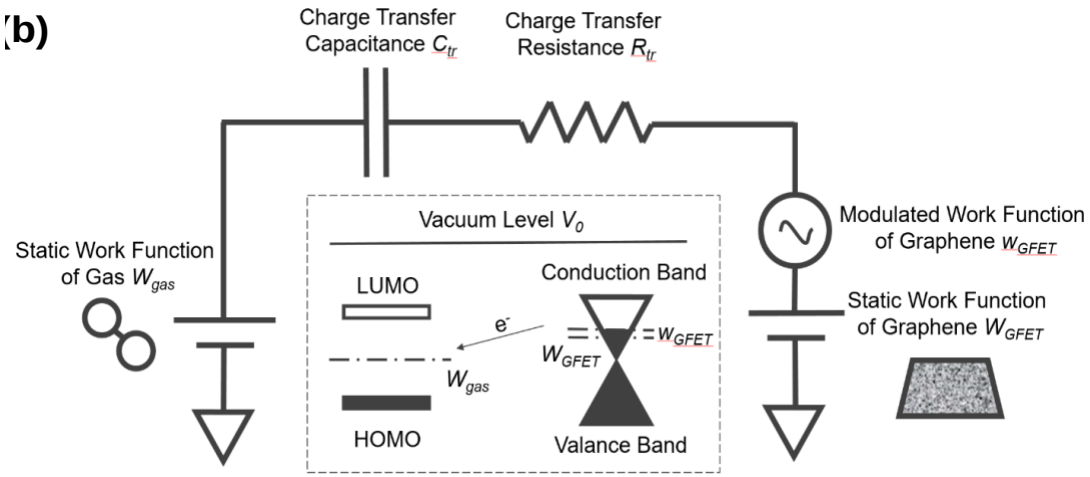

Figure 0.4 The analytical modeling of distance dependent RC time constant of charge transfer.

The charge transfer process between a gas molecule and graphene surface is shown in Figure 6.4. When modulated by an AC gate voltage on GFET (Graphene Field Effect Transistor), the process can be further separated into two parts: 1) the static component Q_{tr} driven by the static work function difference of W_{GFET}-W_{gas}, and 2) dynamic component q_{tr} driven by the modulation w_{GFET},

$$\begin{cases} Q_{tr} = (W_{GFET} - W_{gas})\dfrac{1}{C_{tr}} \\ q_{tr} = w_{GFET}\dfrac{-\frac{j}{\omega C_{tr}}}{R_{tr} - \frac{j}{\omega C_{tr}}} \end{cases} \tag{6.1}$$

where the static and dynamic charge components can be measured through the DC and AC resistance of the GFET channel, respectively. If the phase of w_{GFET} is referenced to zero,

$$\varphi(q_{tr}) = \varphi\left(\frac{-\frac{j}{\omega C_{tr}}}{R_{tr} - \frac{j}{\omega C_{tr}}}\right) \tag{6.2}$$

where the phase carried in q_{tr} has a direct, and measurable description for the charge transfer pathway between the two parties and provides a valuable opportunity to study the fundamental process of charge transfer in different gases – graphene interfaces. Furthermore, both the charge transfer capacitance, C_{tr} and resistance, R_{tr} are subject to change when the gas molecule approaches or leaves the graphene surface, making the phase spectrum of $q_{tr}(\omega)$ a unique tool to reveal distance-sensitive gas concentration during the adsorption or desorption processes (3D gas sensing on 2D surface) – a potential new feature for discriminating different gas responses.

1.26 Device and Experiments

The fabricated device as explained before was purged with nitrogen overnight in the test chamber. Then, a milli-ampere level current was applied through the graphene channel for one minute as the thermal annealing process to remove surface contaminants [82]. The charge neutral point of the fabricated graphene FET was around 25V (p-type doped) due to the unintentional doping of polymer residues during the device fabrication process. Therefore, results in this work were tested in the hole branch of graphene as the DC offset on the gate electrode was kept at 0V. Figure 6.5 illustrates the electrical test setup, where the four-point probe method was used to avoid the influence of contact resistance in the measurement. An AC voltage was applied on the gate electrode with a frequency, f_g, ranging from 50 to 1000 Hz. A lock-in amplifier (SRS 860, Stanford Research Systems) was used to reduce the noise level at the source electrode with a reference of 20 kHz AC current (2μA) through the graphene channel and a 1 MΩ resistor. The voltage between electrode A and B was measured by the lock-in amplifier. A data acquisition device (PicoScope 5242B) was used to collect V_{AB} and V_g simultaneously. With this setup, the phase lag between V_{AB} and V_g can be extracted by fast Fourier transform (FFT).

Figure 6.6 illustrates the gas connections as all gas sensing measurements were carried out in a sealed nylon chamber (2cm×2cm×2 cm) with a waste gas collect system. The concentration of a specific vapor was applied via the split-stream system with dry nitrogen and gas-saturated nitrogen. The flow rates of both gas paths were regulated by mass flow controllers (Omega Engineering) and the total flow rate to the gas sensor was controlled at 200sccm. To ensure no leakage around the seals, the flow rate at the outlet on the chamber was monitored by a mass flow meter (Omega Engineering) and all experiments were carried at room temperature and ambient atmospheric pressure. The chemicals (DI water, anhydrous methanol, and anhydrous ethanol) were purchased from Sigma Aldrich, and inert gas (nitrogen) was purchased from Praxair Inc.

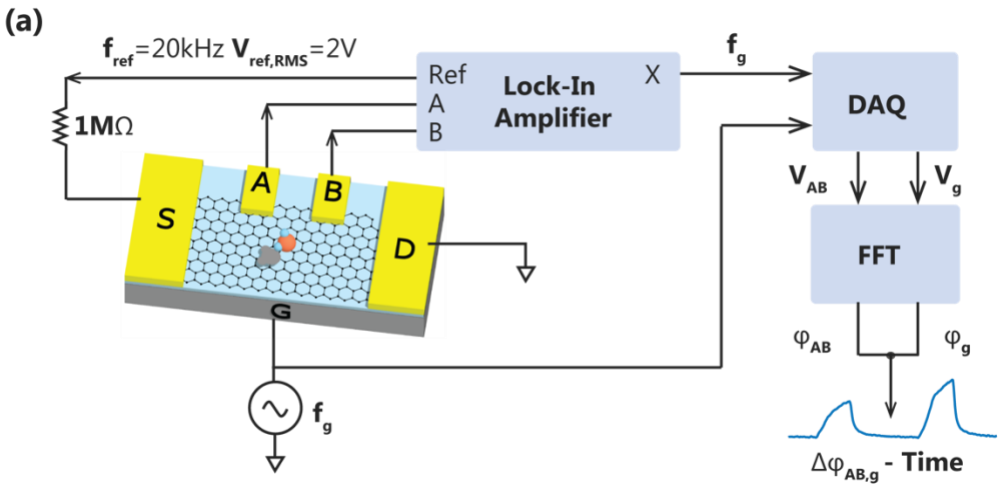

Figure 0.5 Schematic of the AC phase sensing signal flow chart.

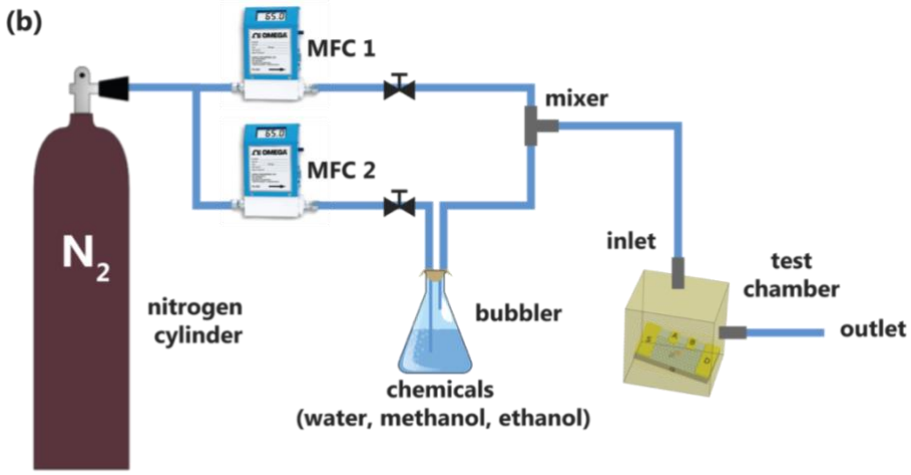

Figure 0.6 Schematic of the experimental setup.

1.27 Results

The responses of the AC phase lag change $\Delta\varphi_{AB,g}$ and the changes of DC resistance $\Delta R/R_0$ are plotted under multiple sensing cycles of water, methanol and ethanol vapors, respectively. Figure 6.7 shows the inputs of vapor concentrations increasing from 10% to 90% stepwise and each cycle includes 40-second chemical vapor feeding following with 160-second nitrogen purging. Figure 6.8 shows the dynamic response of the phase lag at 1000 Hz with minimal drift and the average response time is around 10 seconds. Figure 6.9 shows the DC resistance changes which apparently have significant baseline drift issues as compared with phase lag responses. Furthermore, the average response time is larger than 100 seconds. In principle, the channel resistance decreases after the exposure to the p-type dopant molecules as the device is working in the hole branch of the graphene for all three p-type chemical vapors (water, methanol, and ethanol). After long-term exposures in high concentration vapors, the drop of the charge mobility in the graphene channel becomes significant to pull up the baseline resistance [83]. On the other

hand, the phase lag responses are reversible upon the nitrogen purge process at room temperature as the phase lag response is immune to the strong adsorption gas reactions. For the three tested vapors, the amplitudes of DC resistance responses become saturated when the vapor concentrations are larger than 60% while the phase lag detections can still operate with up to 90% of water or methanol; and 80% of ethanol.

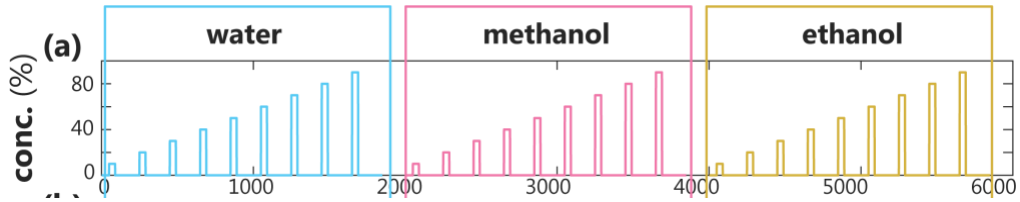

Figure 0.7 Schematic concentration for the phase sensing for multiple cycles of gas exposure for water, methanol, ethanol with concentrations from 10 to 90%, respectively.

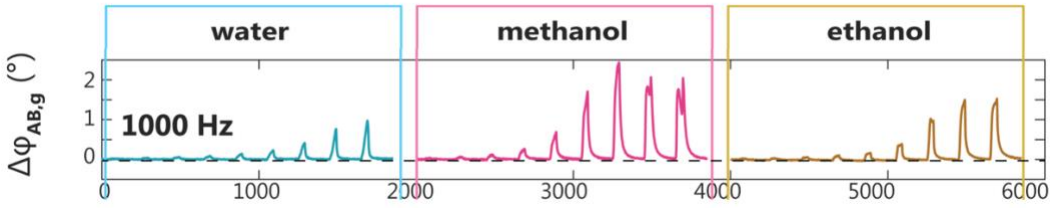

Figure 0.8 Experimental results for the phase sensing for multiple cycles of gas exposure at 1 kHz for water, methanol, ethanol with concentrations from 10 to 90%, respectively

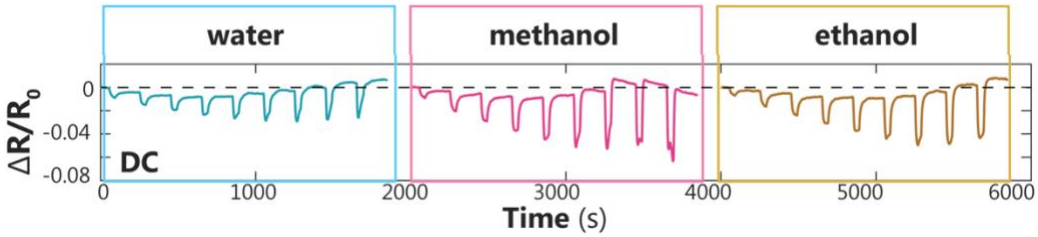

Figure 0.9 Experimental results for the phase sensing for multiple cycles of gas exposure at DC for water, methanol, ethanol with concentrations from 10 to 90%, respectively

The dynamic responses of phase lag upon exposures to water, methanol and ethanol vapors are recorded in Figures 6.10 – 6.12, respectively, at exemplary frequencies of 50Hz, 100Hz, 500Hz and 1000Hz. It is observed that the amplitude of the phase lag change decreases for water vapor as the frequency increases, while the recovery responses at different frequencies have no big differences at around 10-20 seconds (Figure 6.13). For methanol and ethanol, the amplitude of the phase lag change decreases and the recovery time reduces as the frequency increases in general. Specifically, the recovery time for 90% ethanol decreases from 57 to 19 seconds as the frequency increases from 50 to 1000Hz. These results imply that the recovery time can be reduced by using high frequency AC phase lag tests.

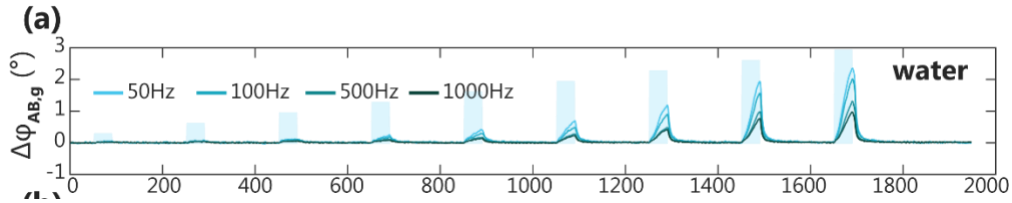

Figure 0.10 Experimental results for the phase sensing for multiple cycles of water for concentrations from 10 to 90%.

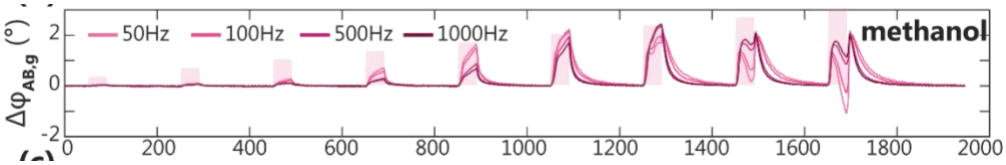

Figure 0.11 Figure 6.11 Experimental results for the phase sensing for multiple cycles of methanol for concentrations from 10 to 90%

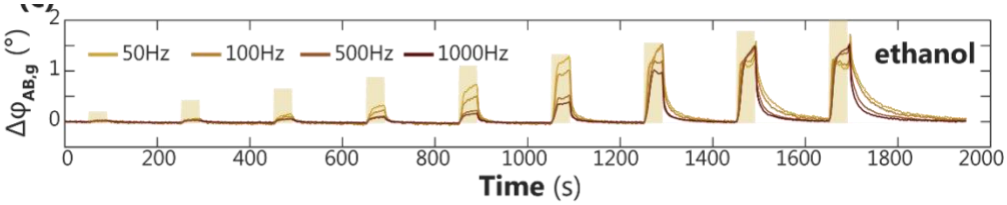

Figure 0.12 Experimental results for the phase sensing for multiple cycles of ethanol for concentrations from 10 to 90%.

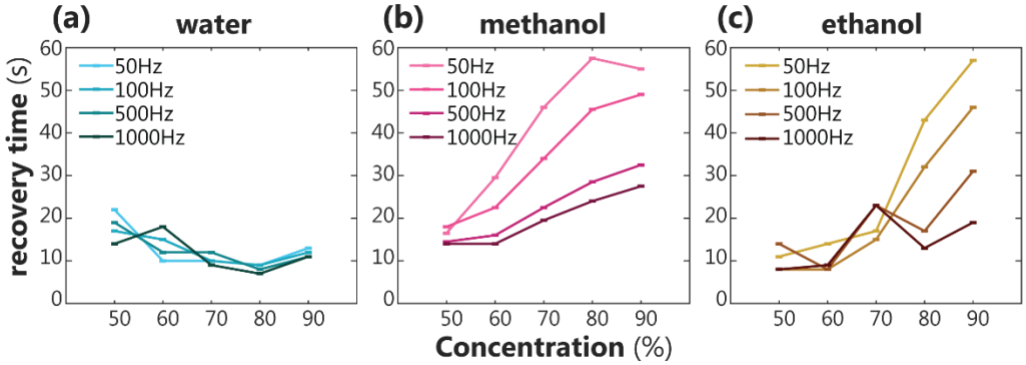

Figure 0.13 Recovery time comparison of gas exposure on a graphene transistor for water (a), methanol (b) and ethanol (c), respectively.

Representative sensing results of AC phase lag spectra upon exposures to three chemical vapors are recorded in the frequency versus time plot, including data for 60% (Figure 6.14) and 90% (Figure 6.15) gas concentrations of water, methanol, and ethanol, respectively. In these tests, the chemical vapors are injected to the system and N_2 purge processes are conducted 50 seconds, and 90 seconds, respectively, after the start of the recording process. These phase lag spectra clearly highlight three important features. First, the recovery speed of the AC sensing scheme at high frequency is faster than those at low frequency as the dark blue color regions (no phase change) reappear faster during the nitrogen purge process. The nitrogen purge process helps the recovery by cleaning the graphene surface, while weakly adsorbed gases (a short distance away from the graphene surface) can be removed easier than strongly adsorbed gases (close to the graphene surface). The

conventional DC sensing signals are dominated by the desorption reaction for gases close to the graphene surface that is slow at room temperature. Second, the signal strength of the AC sensing scheme is smaller at high input frequency as the responsive gases are a short distance away from graphene surface. This can be considered as a trade-off for the fast recovery speed by using the AC sensing scheme as it is more sensitive to the weakly adsorbed gases. Third, negative phase changes may occur under high concentrations of gases as observed in the case of 90% methanol under low frequency sensing. The negative values are not plotted in Figure 6.15 and are represented as zero phase change (color bar) but the trend is clearly observed. This is believed to be the accumulation of gas molecules at a short distance above graphene surface near saturated conditions that are difficult to be cleaned. This phenomenon can greatly damage the recovery speed as shown at the low frequency range while the recovery speed at high frequency range (such as1000 Hz) still maintains within 20 seconds in our testing results. Furthermore, it is potentially reasonable that different gas can induce different adsorption processes on the graphene surface such that the phase change results can be used as a feature to selectively sense the gas types. The slope of the phase change data could also correlate to the dynamic details of the adsorption process. For example, the characteristics of phase change at different frequencies can be differentiated visually while specific machine learning or big data analysis tools could be applied in the works for better and comprehensive identifications.

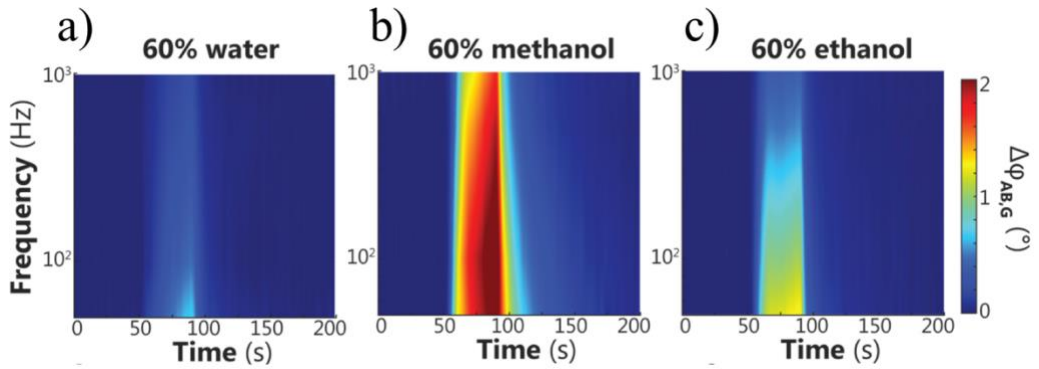

Figure 0.14 The frequency vs time phase spectra for different gases with 60% concentration sensing in one cycle for (a) water, (b) methanol, (c) ethanol.

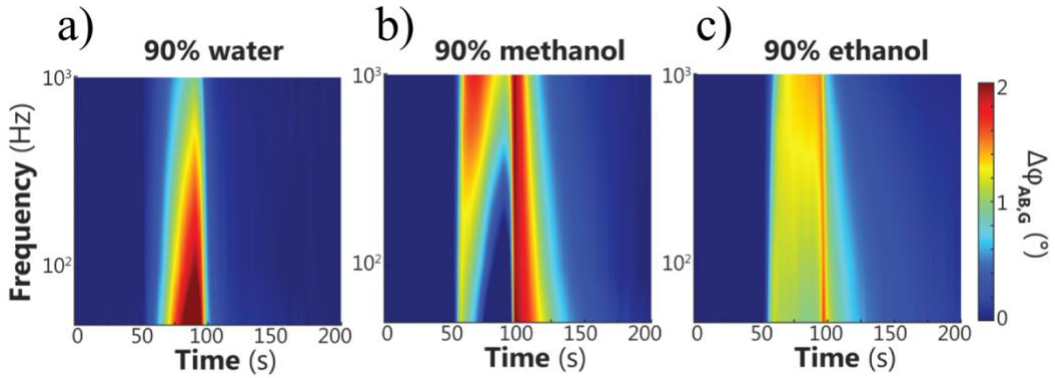

Figure 0.15 The frequency vs time phase spectra for different gases with 90% concentration sensing in one cycle for (a) water, (b) methanol, (c) ethanol.

1.28 Discussion

To explain the sensing results, we have developed a first-principle analytical model to describe the adsorption process of the gas molecule onto the graphene surface along with the charge transfer process [84]. The relationship between the phase lag and the RC time constant of the model is derived. Specifically, this model uses an effective distance between the adsorbed gas molecule and graphene surface to determine the values of R and C and the phase lag associated with the distance between gas molecules and graphene surface reflects the adsorption strength.

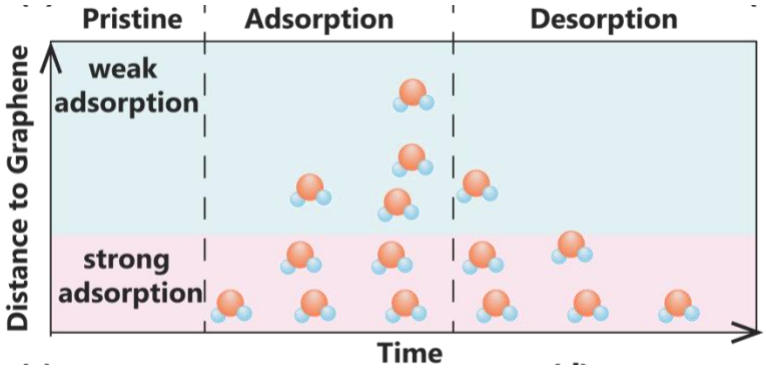

Figure 0.16 The time order of the approaching process of gas molecules on graphene

In this model, the approaching process of the gas molecule onto the graphene surface is illustrated in Figure 6.16 with the RC model shown in Figure 6.3. The carriers in the channel will flow back and forth under the modulation by the applied AC gate voltage [85]. The capacitor C has a phase lag between the channel resistance R_{AB} and the gate voltage V_g and it is defined as: $\varphi_{AB,g} \sim \varphi(\omega\tau)$. Analytically, an adsorption process with a large time constant would induce a smaller amplitude of phase lag in the RC model. The strength of adsorption process is distinguished by the parameter d which represents the distance between the gas molecule and graphene surface. The resistance is modeled as a tunneling resistance $R \sim \exp(A\psi^{0.5}d)$ [86], where A is a constant with the value of $1.025 A^{-1} eV^{-0.5}$, and ψ is the difference in electron affinity between the gas and graphene. The capacitance can be expressed as $C \sim \log(1+r_{mo}/d)$ [87] using the infinite conducting plate model, where r_{mo} is the diameter of an individual gas molecule. Thus, the time constant of the charge transfer process between graphene and adsorbed gas molecules can be analyzed. For weakly adsorbed gases which have small time constants during the gas adsorption process, a large phase lag induced in R_{AB} is expected. This explains the fast recovery time of the phase responses for weakly adsorbed molecules. Specifically, the phase responses at high frequency are used to target/sense gas molecules in a short distance (as compared to those very close) to the graphene surface.

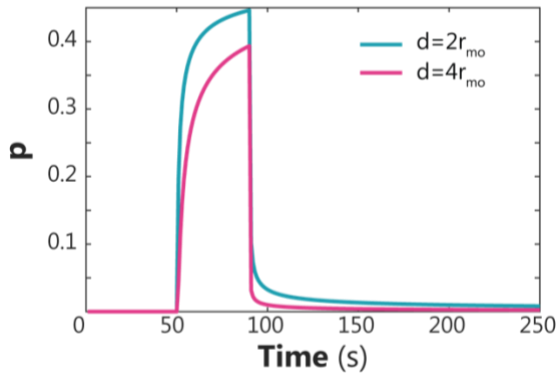

Figure 0.17 Sticking probability vs. time of gas molecules on the graphene surface.

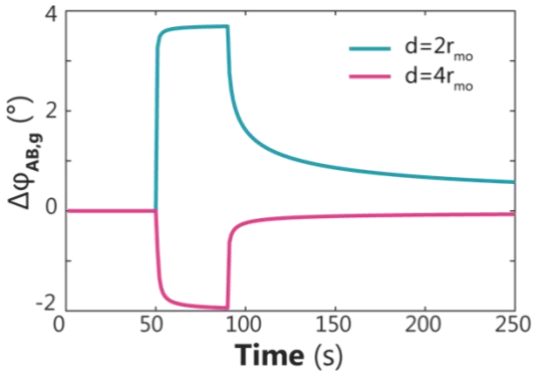

Figure 0.18 Phase change vs. time for weak (purple line) and strong (blue line) gas adsorptions.

To simulate the transient responses, we first calculate the induced phase change from molecules weighted by the sticking probability, then evaluate the integral responses of all adsorbed molecules by accumulating over the relevant range of d<30 r_{mo}. The profile of sticking probability of gas molecules on graphene surface agrees with the molecular number density distribution along the direction perpendicular to graphene given by the molecular dynamics (MD) method analysis [88]. For simplicity, error functions were used to express the probability in the adsorption and desorption periods as $p_a(t) = 0.5\text{-}0.5\text{erfc}(\alpha_a d t^{-0.5} r_{mo}^{-1})$ and $p_b(t) = 0.5\text{erfc}(\alpha_d d t^{-0.5} r_{mo}^{-1})$, respectively, where t is time and $\alpha_{a,d}$ are the fitting constants. Two representative profiles of the sticking probability and their phase lag responses are plotted in Figure 6.17**,** respectively. Here, d/r_{mo}=2 is used to represent the strongly adsorbed gases very close to the graphene surface which are expected to have strong adsorption and weak desorption properties, while d/r_{mo}=4 (or larger) is used to represent the weakly adsorbed gases in a short distance away from the graphene surface which are expected to have slow adsorption and fast desorption properties. The representative responses of the sticking probability p in Figure 6.17 show strong and fast responses during the adsorption process for gases close to the graphene surface (d/r_{mo}=2) while during the desorption process, the gases at a large distance away to the graphene surface (d/r_{mo}=4) have faster responses during the desorption process. Furthermore, the small dip in the phase lag testing in the adsorption process can be predicted by the model. Analytically, the initial protuberance of the phase lag results during the adsorption process for a short

distance away from the graphene surface can be attributed to the large accumulations of gas molecules to result in the slow desorption process. This behavior is simulated numerically as shown in Figure 6.18 for the case of $d/r_{mo}=4$ curve. Nevertheless, the recovery speed for the $d/r_{mo}=4$ curve is much faster than that for the case of the $d/r_{mo}=2$ curve as shown. These characteristics agree well with the experimental results in Fig. 6.15. However, it is noted that the proposed model only provides qualitative insights to explain the phase lag responses and advanced transport models should be developed with accurate properties for different gases to quantitatively fit the test results.

1.29 Conclusion

In summary, we utilized the phase sensing approach to sense chemical vapors based on CVD-processed, monolayer graphene FETs, and the recovery speed of the phase-based sensing approach is much faster than those of conventional DC resistance sensing schemes at room temperature. The superior performances of reversibility (low baseline drift) and fast recovery have been observed in different gas types (water, methanol, and ethanol) of different concentrations at room temperature. It is found that the recovery time can be shortened by using high input frequency sensing. Finally, an analytical model is developed to qualitatively explain the measurement results with good agreements.

Bandwidth Enhanced Method for Noise Sensing on Graphene Gas Sensor

In this chapter, we introduce the noise based gas sensing scheme based on graphene transistors. The noise sensing signal provides several benefits over the conventional DC resistance based sensing, including the fast sensing speed and the sensing selectivity via the power spectrum density (PSD). However, such technique cannot be readily applied to the CVD based graphene sample due to large intrinsic noise associated with the defects. Motivated by this, we proposed the bandwidth enhanced rejection for defects associated noise power from the graphene noise signals, and optimized the sensing speed and sensing linearity on CVD graphene transistors. We organized this chapter in the following manner: the introduction of the origin of the gas adsorption/desorption associated noise on graphene, the Matlab modeling and simulation of the corresponding noise power density, and the experimental validations. This bandwidth enhanced method and the results here could open up a new frontier of CVD graphene FET based gas sensor for accelerating sensing speed and enhancing the sensor fidelity in practical applications and fundamental researches.

1.30 Introduction

Low-frequency noise, also called Flicker noise or 1/f noise, is a common type of noise in semiconductor devices, normally characterized by a power spectral density (PSD) inversely proportional to the frequency. The low-frequency noise power spectral density in the graphene field effect transistor (GFET) exhibits a M-shape or V-shape carrier concentration (or gate-biased) dependence due to the fluctuation of the adsorption and desorption processes of carriers in the conducting graphene channel through tunneling events, which are sensitive to the Fermi level position of graphene [89-91]. The specific characteristics of PSD from graphene is quite different in comparison to those from devices based on other materials [92-105]. The dominant low-frequency noise in GFET is often high, which can limit analog, mixed-signal, radio frequency systems for the sensor performances [106]. Therefore, it is important to understand the low-frequency noise mechanism and find methods to reduce the noise level, such as the use of suspended channels [107], graded thickness in graphene contacts [108], processing protocol to avoid aqueous chemistry [109], and screening trapped charges via few-layer graphene channels [110].

Previously, low-frequency noises on graphene-based gas sensors have been utilized as potential sensing parameters for graphene gas sensors for improved sensitivity, selectivity, fidelity and recovery speed as compared to time-domain resistive sensing parameters. For example, L. B. Kish et al. proposed the fluctuation-enhanced chemical sensing scheme by capturing the characteristic micro-fluctuations to realize an electronic nose/tongue [111-113]. A. A. Balandin et al. showed different gas chemicals can produce distinguishable effects on the low-

frequency noise spectra of graphene [114-118]. K. R. Amin et al. reported a chemical vapor sensor based on the measurement of low-frequency resistance fluctuations of GFET devices with high sensitivity, specificity, fidelity, and fast response time [119,120]. S. Dana et al. found gas-selective signal amplification in fluctuation-based GFET sensors [121]. It is worth noting that these aforementioned reports are all based on mechanically exfoliated graphene FETs. Gas sensors made of CVD graphene normally suffer from defects and disorders during the fabrication processes, including cavities on graphene from the CVD growth process, contaminations of the graphene from the substrate, and dangling bonds at the edge of graphene from the etching process. These defects can bond strongly with gas molecules [122] and it is important to study and characterize the gas sensing results of low-frequency noise spectra based on GFETs made of CVD graphene.

Here, we report the gas sensing results using low-frequency fluctuation signals based on CVD-grown graphene. A theoretical model is proposed to explain the resistance fluctuation on CVD graphene by integrating three kinds of noise from intrinsic trap-states, extrinsic trap-states, and defects. We measure the low-frequency noise power spectral density of CVD GFET in nitrogen and other chemical vapors at room temperature. Large change of the low-frequency noise energy after the injection of chemical vapors can be observed. However, the characteristic Lorentz bulge in the 1/f noise (1-1000 Hz) as reported previously in the mechanically- exfoliated graphene FET gas sensors can't be clearly identified in our CVD graphene FET gas sensors. On the other hand, we show that CVD GFET gas sensor using resistance fluctuations as the sensing parameter could have fast response, high sensitivity, and good linearity.

1.31 Modeling the gas sensing based on low-frequency noise

GFET gas sensors are well known operate based on the change of channel resistance due to the surface charge transfer events. As shown in Fig. 7.1, a gas molecule becomes a positively charged impurity after donating electrons from its molecular orbital to graphene in the gas adsorption process. The charged impurity can scatter the carriers in the long-range manner or short-range manner, which is called intrinsic trap-states. Under the graphene channel, there are mutual charge transfers between graphene and SiO_2, which is called extrinsic trap-states. The changing number of electrons leads to the slight fluctuation of the resistance of graphene, which can be plotted as the resistance change in the time-domain plot and can be shown as the power spectral density in the frequency-domain plot as a noise which is often reversely proportional to frequency as shown.

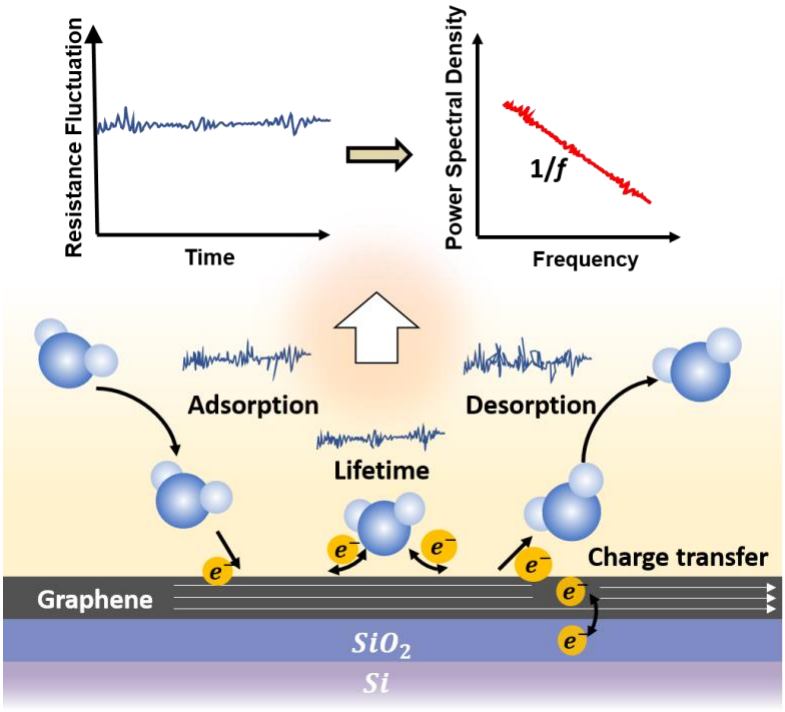

Figure 0.1 Schematic of the origins of gas-induced noises on graphene.

The low-frequency electronic noise on CVD graphene is modeled by the combination of three kinds of noise in this work. Intrinsic trap-states caused by charge transfer process between graphene and SiO_2 have different time constants with relations to a set of bulges. The accumulation of the bulges forms the intrinsic noise. Considering the density distribution of lifetimes: $g(\tau_N) = [\tau_N ln\frac{\tau_2}{\tau_1}]^{-1}$, intrinsic noise can be described by the McWhorter model, which uses the carrier-number-fluctuation approach [123-125]:

$$S_N(\omega) = 4\delta N \int_{\tau_1}^{\tau_2} g(\tau_N) \frac{\tau_N}{1 + (\omega\tau_N)^2} d\tau_N \qquad (7.1)$$

where τ_1 and τ_2 are the limits of a logarithmically wide timescale; $\omega = 2\pi f$ is an angular frequency; and δN is the fluctuation of charge carriers. Extrinsic trap-states caused by the charge transfers between gas molecules and graphene include the adsorption, lifetime and desorption processes form a characteristic bulge [136]. Figure 7.2 shows the schematic diagram of a single methanol molecule experiencing adsorption, lifetime and desorption process to cause the graphene resistance fluctuations, where τ_{ads} is the time for the adsorption process; τ_{life} is the time for the lifetime; and τ_{des} is the time for the desorption process. This characteristic bulge will become more obvious by multiplying it with frequency f [128]. The position of this bulge is usually determined by the slowest process in the charge transfer event, which is the desorption process in this case [126]. The variety of time constants are determined by the energy needed for different gas molecules and a specific desorption process can be estimated [127] by using:

$$\tau = \nu^{-1} e^{\frac{E_D}{RT}} \qquad (7.2)$$

where υ is the value of the frequency of adsorbed gas molecule; E_D is the activation energy; R is the gas constant; and T is temperature. The charge transfer process results in a fluctuation in the resistance, R, of the graphene channel. Here, we use resistance to normalize our simulation model. Electric conductivity can be calculated by $\sigma = ne\mu$ [128], where n is the carrier concentration; e is the number of the electrons transferred; μ is the mobility of charge carriers of graphene. The number of electrons transferred can be obtained from previous experiments [129,130] and the number is found to be very small such that we ignore the change it brings to n and μ. Resistivity ρ is the reverse of electric conductivity and the resistance is given by $R = \rho l/S$ and the resistance fluctuation δR is derived as:

$$\delta R = \frac{\delta N}{n^2 \times e \times \mu \times \frac{W}{L}} \tag{7.3}$$

where δN is the number fluctuation in gas molecules interacting with graphene. The Langmuir model is employed to roughly estimate the fractional coverage [131]. The fractional coverage, θ, to the concentration of gas, c, is related by means of activation adsorption energy of gas, as $\theta = \left[\frac{\beta c}{1+\beta c}\right]$ with $\beta = \exp(-\frac{E_a}{RT})$[132]. The resistance fluctuation of all interacting gas molecules is very complex as shown in Figure 7.3**,** which is obtained with $\delta N = \theta S$ for 1000 methanol molecules where the number of gas molecules is related to the concentration of gas. The noise from the total extrinsic trap-states of gas has a bulge characteristic in medium frequency domain (10 to 10000 Hz) as observed in Figure 7.4.

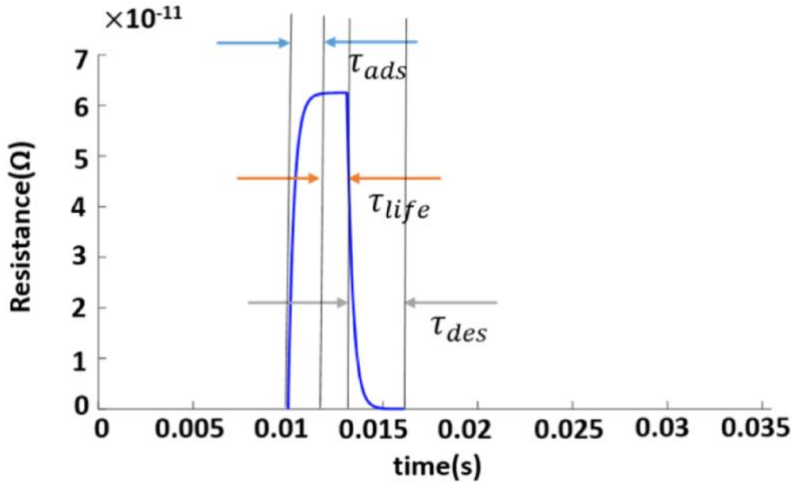

Figure 0.2 Transient resistance of a single gas adsorption event

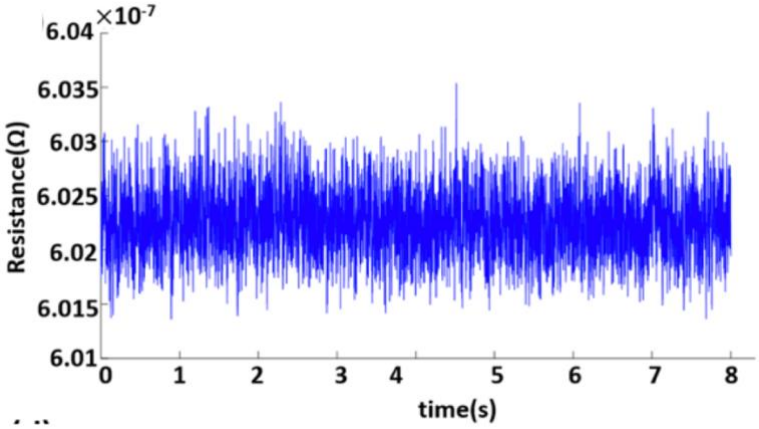

Figure 0.3 Transient resistance of 1000 random gas adsorption events

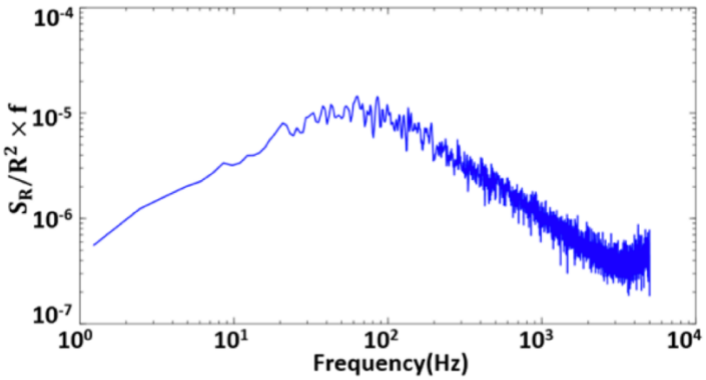

Figure 0.4 Power spectrum density (PSD) of a single gas adsorption event.

The defects are modeled based on the specifics of CVD graphene, such as vacancy, impurity, and topological defects [133,134]. The energy needed for charge transfer between the gas molecules and surface with defects is generally larger than those of areas without defects, such that it is more difficult for gas molecules to interact with graphene [135,136]. From equation (2), longer time is needed for processes with larger energy. Due to the slow interaction processes, the time constant coming from defects, which can also be related to a set of bulges, only show up in extremely low frequencies. Therefore, the white noise of the low-frequency noise is omitted in our model. In high frequency domains, white noise occupies the key positions and makes the PSD results noisy and difficult to retrieve useful information. The low-frequency noise model of CVD graphene composed of intrinsic noise, extrinsic noise; and defects noise is simulated and plotted such with methanol under different concentrations as shown in Figure 7.5.

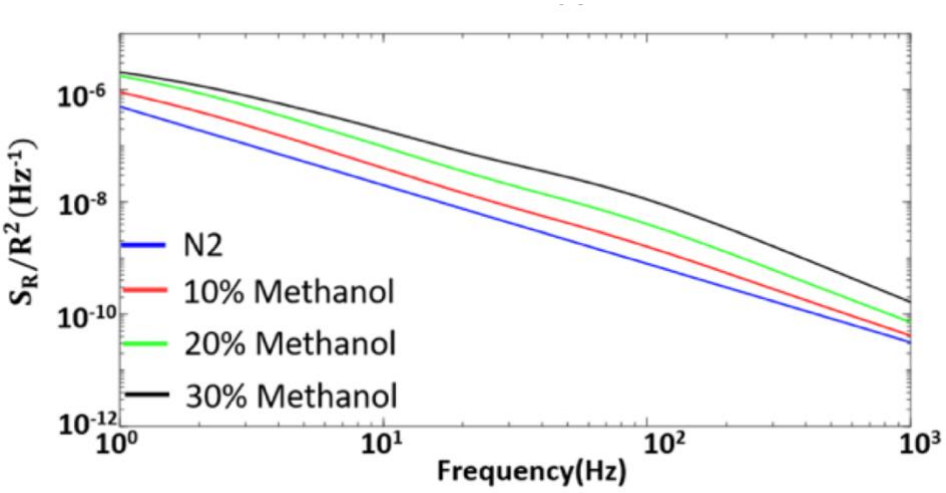

Figure 0.5 Power spectrum density (PSD) of measured gas adsorption on graphene.

1.32 Experiment

A four-point probes method was used to avoid the effect of contact resistance in the measurements of the graphene resistance. A standard low-frequency alternating-current (AC) with lock-in measurement technique was employed to fetch the source-drain voltage fluctuation data of a CVD grown graphene FET sensor. The AC technique can simultaneously measure both sensor resistance fluctuations and background noise compared with the direct current (DC) lock-in method. The instrument control and gas measurement process were automatically executed by a MATLAB program. The low-frequency noise measurement setup for the AC lock-in measurement techniques is shown in Figure 7.6. The time constant of the lock-in amplifier was set to 30 micro seconds, which determines a measurement bandwidth of 5.3 kHz. The sampling rate of the data acquisition (DAQ) card was set to 40kHz considering the Nyquist sample theorem. Frequency of the source (V_{sd}) was kept higher than the measurement bandwidth and was set to 6kHz. The source-drain current I_{DS} was biased to 1 µA which is sufficiently small to avoid the current induced effects such as electro-migration with a carrier frequency significantly higher than the upper cutoff frequency of the noise measurement bandwidth. The stream mode of the data acquisition card was employed to realize the high-capacity data acquisition, transmission and high-efficiency storage. High purity nitrogen (>99.998%) was utilized with mass flow controllers to control the total flow rate and the vapor concentration into the chamber. The dry nitrogen was divided into two parts. One part was saturated with chemical vapor by pumping into liquid chemicals (ethanol and methanol). Another part with dry nitrogen was then mixed with the first part to achieve the desired concentration.

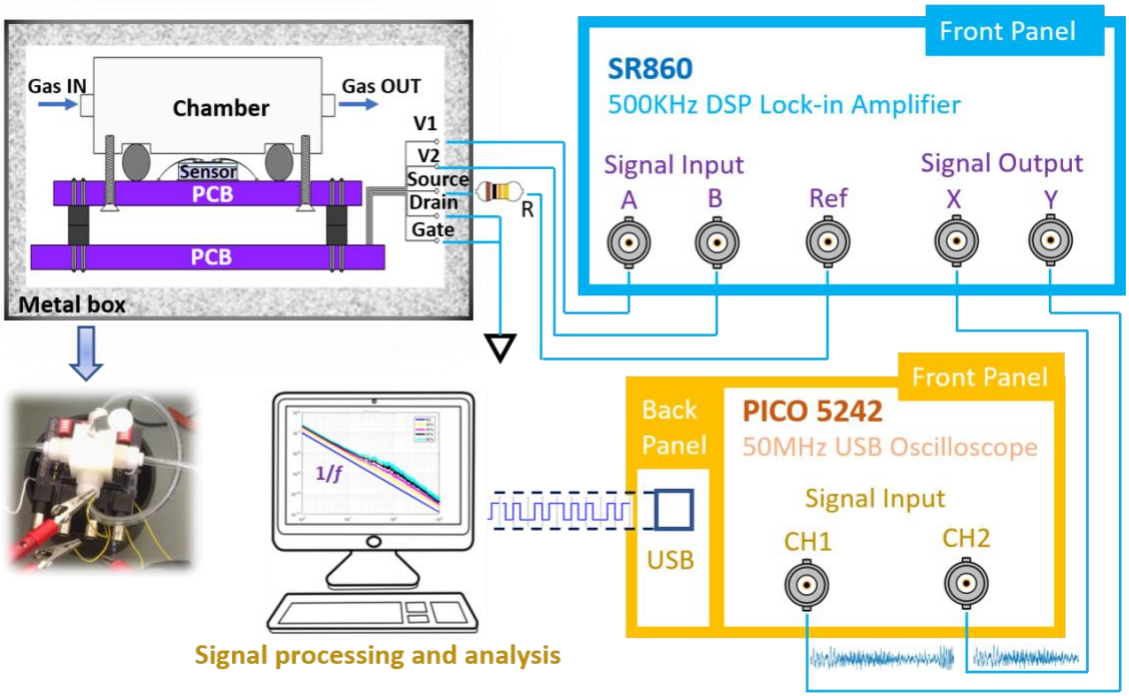

Figure 0.6 Schematic setup of the noise measurement on graphene.

1.33 Results

The measurement system was enclosed in an aluminum box to lower the electrical interferences coming from the environment. However, the measurement result is still very noisy because of the pollution of complex environmental noises (Figure 7.7). Therefore, several comprehensive digital signal processing (DSP) methods are employed, including multistage-decimation, 1-D stationary wavelet transform (SWT) method with 3-level harr wavelet and the Welch's averaged periodogram method with Blackman-Harris window to retrieve the effective power spectral density (PSD) (Figure 7.8) under complex background noises. After that, the PSD plots become much cleaner and most noisy spectrum coming from the environment are eliminated except the power frequency spectrum (60Hz and its odd times frequencies) from the power lines. Figure 7.8 shows a typical noise spectral density $S_V/V^2 \propto 1/f^\gamma$ with experimental parameter γ=1.21.

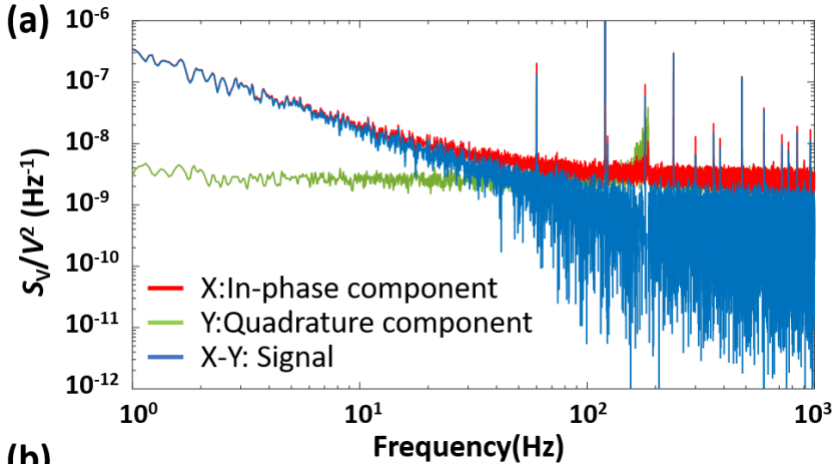

Figure 0.7 Noise PSD measured before signal processing. (need to remove (a) & (b))

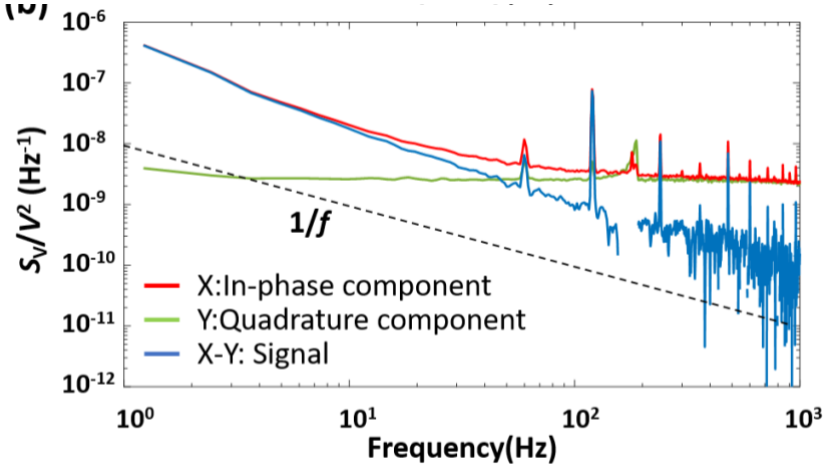

Figure 0.8 Noise PSD measured after signal processing.

The experimental data of the noise spectra under the exposure to different vapors (methanol and ethanol) have been obtained and the comparisons between the experiment and simulation results are conducted. Figure 7.9 and Figure 7.11 are the simulation and experimental results of noise power spectral density in different vapor concentrations of methanol and ethanol between 1-1000 Hz, respectively. As we magnify the low frequency domain between 1-100 Hz (Figure 7.10 and Figure 7.12), our model match relatively well with the experimental result. However, the high frequency regions don't have a good match because the model doesn't include the white noise.

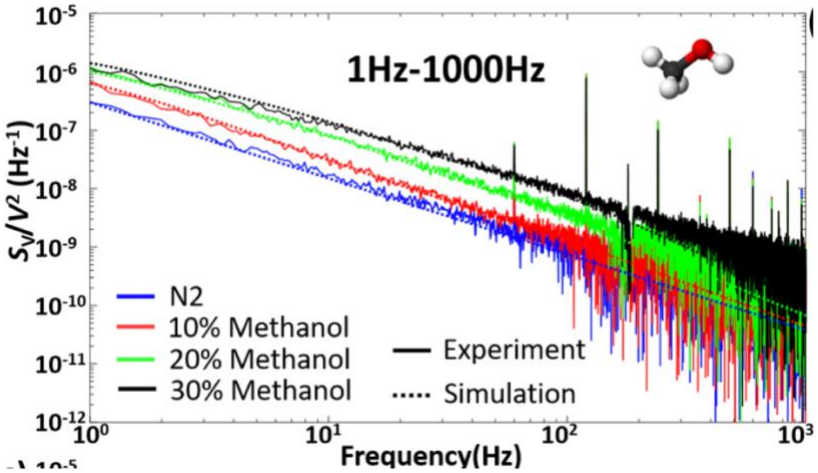

Figure 0.9 PSD of methanol adsorption on graphene

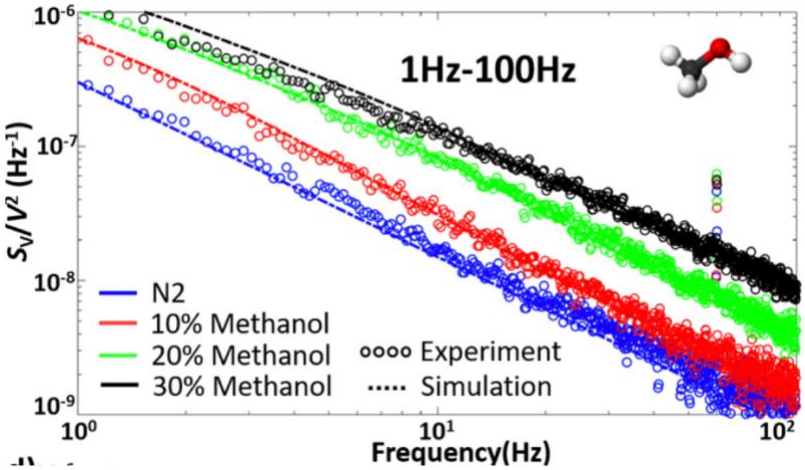

Figure 0.10 PSD of methanol adsorption on graphene with bandwidth (1Hz-100Hz).

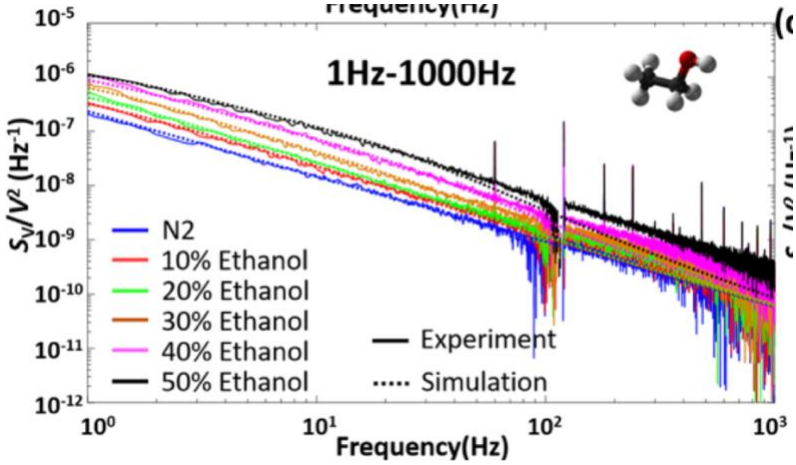

Figure 0.11 PSD of ethanol adsorption on graphene.

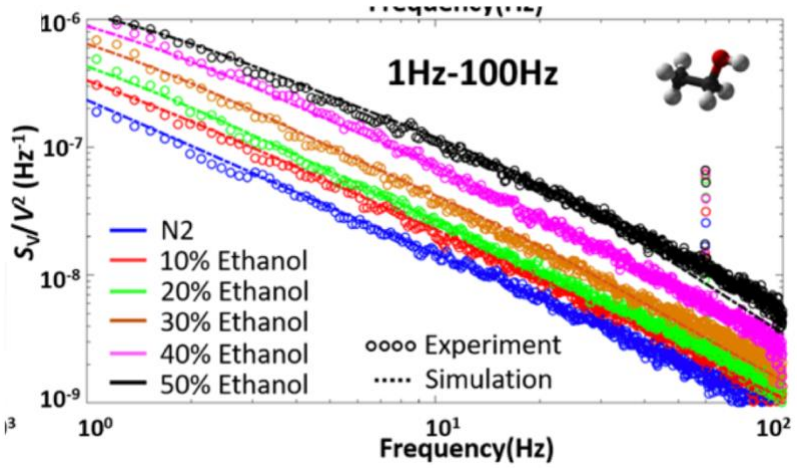

Figure 0.12 PSD of ethanol adsorption on graphene with bandwidth (1Hz-100Hz)

The normalized energy of resistance fluctuation $E_n(t)$ can be calculated by integrating the measured power spectral density $S_V(\omega)$ over the data acquisition bandwidth as:

$$E_n(t) = \frac{1}{V^2}\int_{\omega_1}^{\omega_2} S_V(\omega)d\omega \tag{7.4}$$

Here, ω_1 is the lower frequency decided by the data sample rate and sample number, and ω_2 is the upper frequency given by the DAQ acquisition rate. To efficiently utilize the information of low-frequency noises of the sensor, the responses of methanol vapor have been measured at various concentrations and the corresponding changes in the channel resistance R and noise energy E_n are shown in Figure 7.13(a) and Figure 7.13(b) respectively. Four different features have been identified. First, the dynamic response speed of the low-frequency noise energy E_n (several seconds) is faster than that of the DC resistance signals (more than 100 seconds). Here, the dynamic response is defined as 90 percent of the stable state was maintained. Second, the channel resistance signal features a very slow baseline recovery speed and large baseline drift due to strongly adsorbed sensing gas residuals on the defect-rich graphene surface [100-102]. In comparison, the change of noise energy can achieve a fast recovery and minimal baseline drift. Third, the sensing sensitivity of noise energy is about 60% of the original value, which is much higher than the change of resistance value at about 0.4% of the original value. Finally, the linear relationship between the gas concentration and resistance is poor while the linear relationship between the gas concentration and noise energy is strong as shown. These results suggest that the low-frequency noise information could be feasible as a promising parameter to achieve high sensitivity, strong linearity and fast response sensing as compared with the channel resistance parameter for the CVD GFET gas sensors.

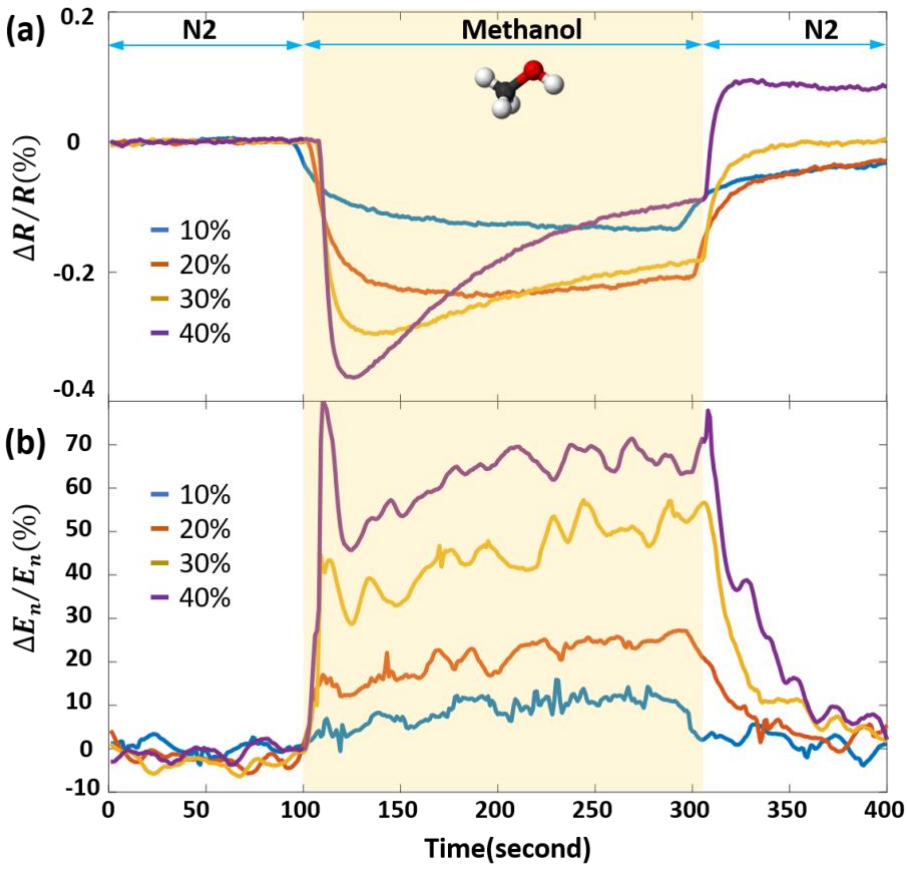

Figure 0.13 Sensing results when exposed to methanol with different concentrations: (a) DC resistance change and (b) noise change.

1.34 Discussion of Noise Origin in CVD Graphene

Mechanically exfoliated graphene FETs have been shown for gas sensing by means of the low-frequency fluctuation of resistance with rather complicated and costly processes. CVD graphene has much better potential for mass production processes as it is less expensive to produce but its characteristics of low-frequency resistance fluctuation in the form of FETs has not been explored. Here, the change of the noise spectra of CVD graphene is investigated. It is found that the low frequency part of spectra has good sensitivity because the noise level changes with respect to the gas concentration but the bulge is not as obvious as that of mechanically exfoliated graphene. The main reason may originate from the CVD fabrication process which produces cavities and defects on graphene [137,138]. Another reason may come from the process of lithography and etching which can result in additional defects. For devices made of mechanically-exfoliated graphene, the noise is mainly composed of two kinds of noises: intrinsic trap-states which result in 1/f noise (Figure 7.14) and extrinsic trap-states (Figure 7.15) which result in the characteristic bulge.

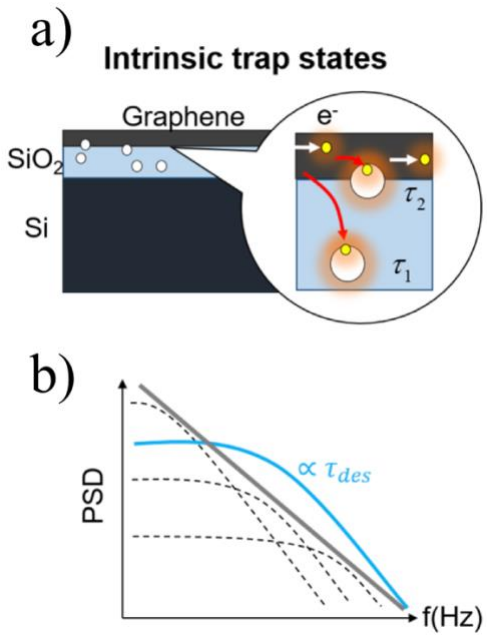

Figure 0.14 Schematic and noise PSD of the intrinsic graphene: (a) schematic of the trap states, and (b) PSD of the defect dominated scenario

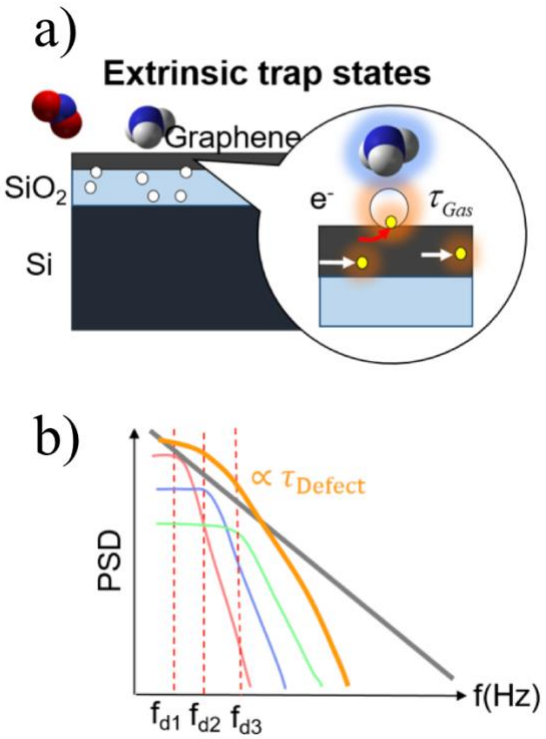

Figure 0.15 Schematic and noise PSD of the extrinsic source on graphene: (a) schematic of extrinsic trap states and (b) PSD of the extrinsic defect dominated scenario

Furthermore, the noise multiplied by frequency plots for devices made of mechanically-exfoliated graphene can show obvious bulges in the frequency

domain [125]. For devices based on CVD graphene, the existence of defects can be observed in scanning electron microscope (Figure 7.16). The defect noise exists only in the low frequency regions, making the characteristic bulge less obvious to be observed (Figure 7.17). Since the level of extrinsic trap-states bulge rises with the increase of concentration in the medium frequency domain, we can still observe the level variations. For the gas whose characteristic bulge does not coincide with the defect noise, the gas sensing of CVD graphene can still be obtained in the characteristic bulge frequency domain. From Fig.7.13, we showed some main advantages using the characteristic bulge frequency domain for analysis, such as high sensitivity, strong linearity and fast response as compared with the channel resistance on the CVD GFET. Based on these results, we believe that specific frequency noise information of CVD graphene is a promising parameter to achieve great performances for gas sensing.

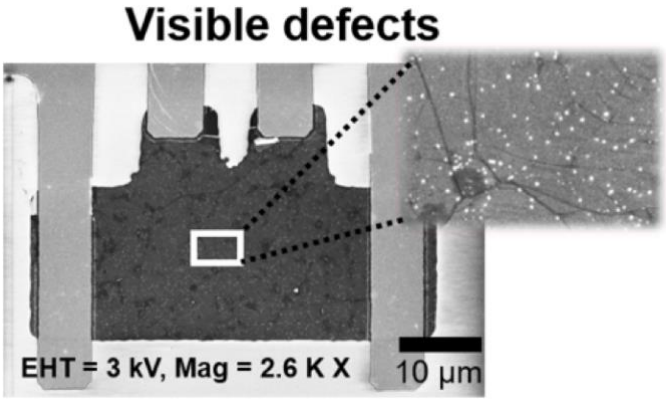

Figure 0.16 The visible defects of CVD graphene.

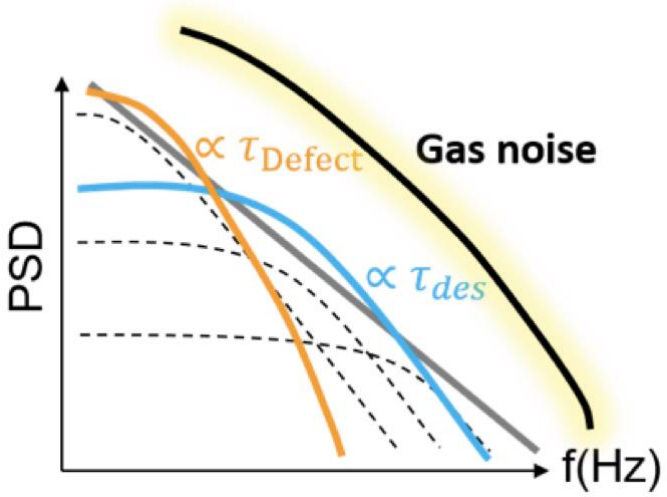

Figure 0.17 Schematic and noise PSD of the defect + intrinsic graphene.

1.35 Conclusion

In conclusion, we demonstrated the low-frequency noise gas sensing results coming from CVD graphene FETs. We used alternating-current lock-in measurement techniques and adopted advanced signal processing method include, 1-D stationary wavelet transform method harr wavelet and the Welch's averaged periodogram method with Blackman-Harris window to achieve the low-frequency noise in complex experimental environments. Based on this method, we found that the low-frequency fluctuations of gas sensor exposure to ethanol, methanol, and water vapors can have 1/f noise dependence with large changes in the frequency domain. At the same time, the gas molecules adsorption-desorption model is in good agreement with the experimental results. However, the characteristic Lorentz bulge in 1/f noise (1-1000 Hz) as reported previously in mechanically-exfoliated graphene FET gas sensors did not show up in our experimental results

Emerging Structure of Graphene FET

In this chapter, we proposed two types of new structures to deploy the graphene transistor into the emerging applications. Motivated by the flexible electronics and wearable sensor applications, we first introduced the fabrication process for an all-polymer based graphene transistors through the flexible transfer technique on polyimide, and provided the device characterization as well as the gas sensing results for the graphene sensor on the flexible substrate. Additionally, in section 8.2, we introduced the direct-write, self-aligned transistor fabrication process for dual-gate graphene FET, and provided the electrical parameter characterization as well as the finite element analysis for the cylindrical shaped gate dielectrics. These new fabrication processes developed in this chapter can potentially open up unconventional applications scenarios for graphene transistors in the areas of chemical sensing and mass production.

1.36 Graphene FET Gas Sensor on A Flexible Substrate

1.36.1 Introduction

Here we demonstrate a gas sensor utilizing graphene as the sensing material, as shown in Figure 8.1, and implement it on a flexible polyimide substrate. By monitoring the channel current under a fixed V_{DS} and specific V_G, the real-time doping effect from ammonia to graphene could be detected as the gas sensing mechanism. Figure 8.2 shows the cross-section schematic of the flexible gas sensor, and the inset shows the as-fabricated 9x9 GFET array on a flexible substrate. In this chapter, the characteristics of the GFET on both rigid and flexible substrates with polymer gate dielectrics have been experimentally characterized. The sensing responses under different gas concentrations and gate voltage biases have been recorded. Furthermore, observation of time-variant doping of graphene in FET sensors after their exposures to ammonia has been monitored as a potentially new sensing scheme.

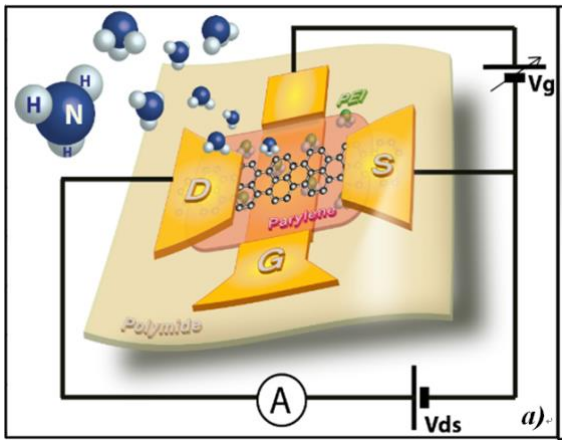

Figure 0.1 Schematic of flexible gas sensor based on graphene.

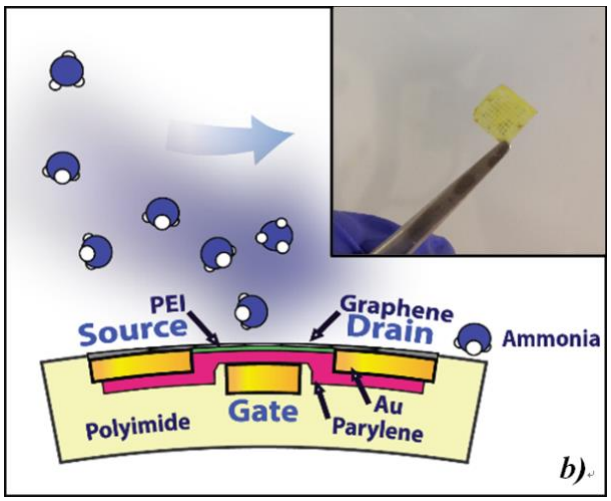

Figure 0.2 Cross-section view of the all-polymer graphene gas sensor.

1.36.2 Fabrication Process

Firstly, the high quality single layer graphene sheet is synthesized via chemical vapor deposition (CVD) on a copper foil under 1000°C and transferred onto a thermally grown 285nm-thick SiO_2 on a p-doped silicon wafer as described in our previous work [139]. The quality of the graphene sheet is verified using Raman spectroscopy. Figure 8.3a illustrates the graphene substrate before the fabrication process. The source and drain electrodes are deposited and patterned by Ti/Au (2nm/50nm) e-beam evaporation using a shadow mask (Figure 8.3b). Then a 5um×5um graphene channel is patterned and etched by a 50W oxygen plasma process for 7s using the standard optical lithography process (Figure 8.3c). The whole device is spin-coated with a 1um-thick, 50% w.t. PEI solution using H_2O as the solvent (Figure 8.3d). Due to the physisorption, a thin layer of PEI is left on the graphene sheet after the DI water rinse, and the residual PEI is utilized as the n-type dopant for the graphene sheet (Figure 8.3e). A layer of 170nm-thick Parylene-C is then deposited using MVD (Special Coating System PDS2010) after a Gamma-

MPS coating process (Figure 8.3f) and then the parylene is patterned by a 100W oxygen plasma process for 60s using the standard optical lithography (Figure 8.3g). The top gate (TG) is patterned by the Cr/Au (2nm/50nm) e-beam evaporation process using a shadow mask and the p-doped silicon functions as the back gate (BG) (Figure 8.3h). Afterwards, a 40um-thick polyimide (HD Systems, PI-2574) layer is spin-coated and cured at 180°C (Figure 8.3i). Finally, the flexible structure is released by using the 10:1 buffered oxide etch (BHF) solution (Figure 8.3j). It is worth noting that a hydrophobic surface is required for a uniform parylene MVD deposition, such that the Gamma-MPS treatment is necessary after the PEI deposition process as PEI layer alters the surface contact angle from 85° of pristine graphene to 15°, as shown in Figure 8.4.

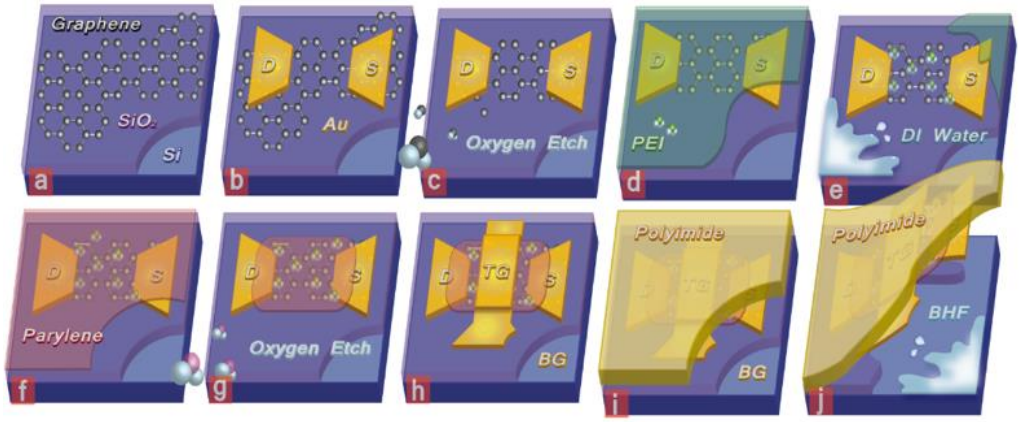

Figure 0.3 Process flow for the flexible sensor transfer onto polyimide.

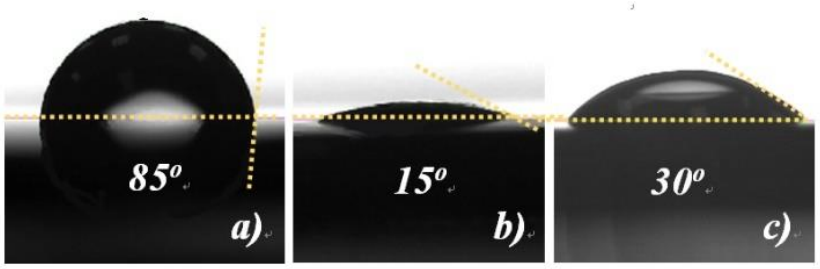

Figure 0.4 Contact angle of the graphene (a) PEI treated (b) and Gamma-MPS treated (c) surface.

Figure 8.5a and Figure 8.5b show the optical microscopic pictures of a 3x3 device array before/after the transfer process from the rigid wafer onto a flexible plastic substrate, respectively and Figure 8.5c and Figure 8.5d shows enlarged views. After transferred onto the flexible substrate, graphene is directly exposed to the environment for sensing and the gate electrode is embedded in the polyimide substrate. The flexible transistor is made contact to the breadboard via conductive paste and fixed in the gas chamber. Not all GFETs could be successfully transferred onto the polyimide substrate, and the major reason for failure is the delamination of metal contact pads as shown in the upper left corner of Figure 4b.

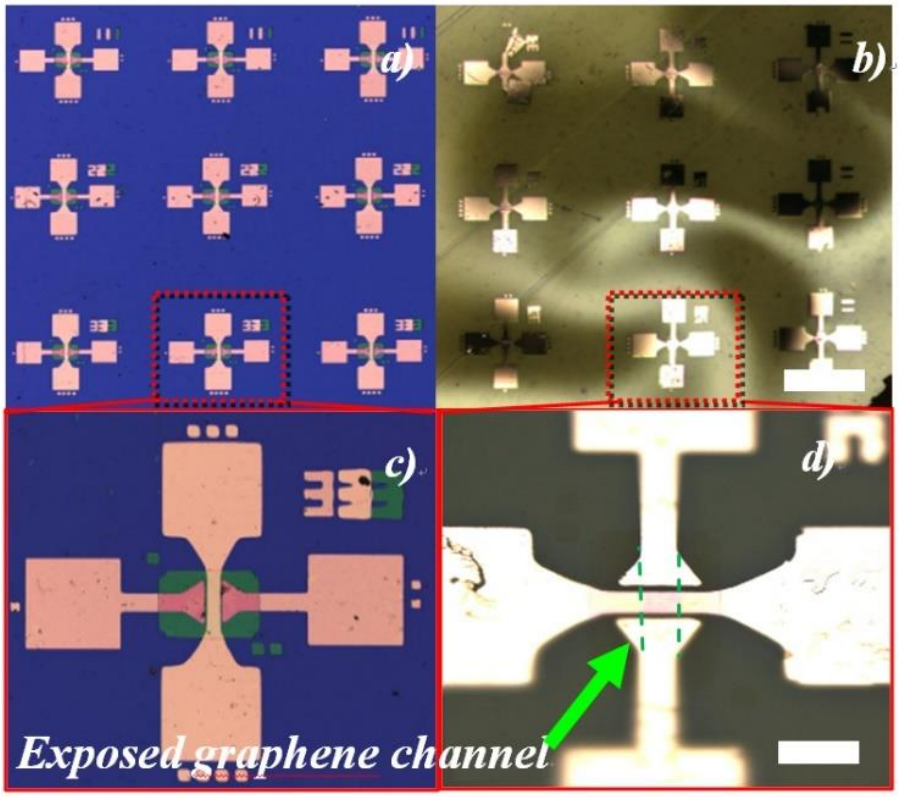

Figure 0.5 Fabrication results of the flexible graphene transistor array (a) before transfer and (b) after transfer, with the enlarged view in (c) and (d).

Figure 8.6 shows the schematic of the gas sensor testing system. The flexible gas sensor is sealed in the chamber, and nitrogen is purged, and followed by a pumping down process to 10^{-3} torr. Afterwards, the target gas is introduced into the chamber by opening the control valve (V_2 in Figure 8.6). The amount of gas concentration inside the chamber is monitored by the pressure gauge. The source drain voltage of the GFET is fixed at V_{DS}=0.1V throughout the experiment, and the channel current I_{DS} is sampled twice per second using Agilent digital multimeter 34401A.

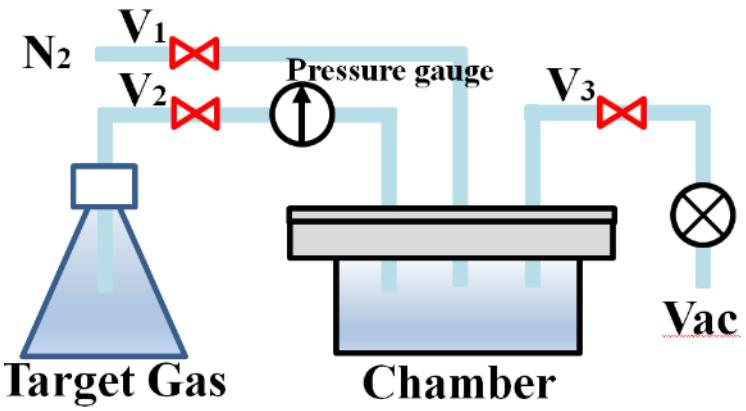

Figure 0.6 Gas testing setup of the flexible gas sensor.

1.36.3 Results

Experimentally, GFETs under dual-gate operations are characterized on solid substrate before the transfer process. Figure 8.7 shows the I_{DS}-V_{TG} curves (source-drain current versus top gate voltage) of a GFET under various V_{BG}. The majority carriers in graphene on the non-overlapping area (see inset in Figure 8.7) between the top gate and source/drain electrodes are mainly controlled by the back gate bias, and weakly controlled by the top gate bias due to the weak fringing field effect. The graphene channel directly under the top gate is controlled by both of the top and back gate biases. Specifically, electrons are attracted to the graphene channel under positive bias and holes are attracted to the graphene channel under negative gate bias. Experimentally, under V_{BG}=50V, the majority carriers in the non-overlapping, overlapping, and non-overlapping graphene channel, (left to right in the inset of Figure 8.7) are electrons when the top gate voltage, V_{TG} changes from -10V to 90V. On the other hand, if V_{BG} is -50V, the majority carriers in the aforementioned regions switch to holes, electrons, and holes as V_{TG} changes from -10V to 90V. Therefore, it is possible to form a p-n-p junction in the graphene channel under the right biases of V_{TG} and V_{BG} and double local maximum resistances can be identified is in the I_{DS}-V_{TG} curves in Figure 8.7, similar to the previous report [140].

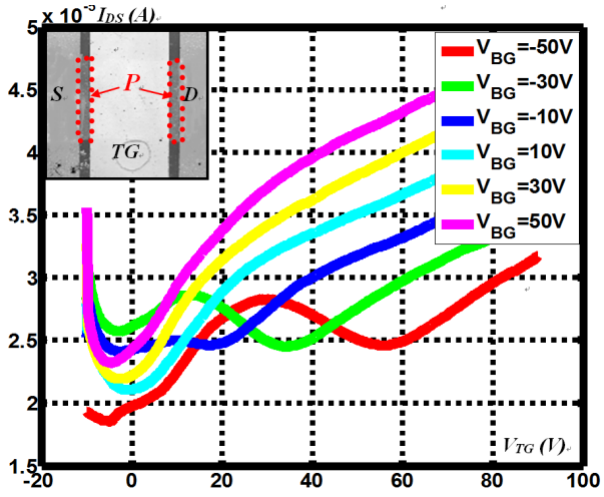

Figure 0.7 Dual gate ~ channel current characterization of the flexible graphene FET.

The I_{DS}-V_{DS} and I_{DS}-V_G curves of a flexible GFET under different gate voltage are measured and shown in Figure 8.8a and Figure 8.8b, respectively. In Figure 8.8a, a crossover of two curves (V_G=20V, V_G=0V) is observed after V_{DS}>3V. This is because the majority carrier of the graphene channel switches from a suppression of holes to an accumulation of electrons as V_{DS} increases to alter the voltage distribution of graphene channel and flips the major carrier type. In Figure 8.8b, the hysteresis phenomenon is observed with forward and backward sweeping of the gate voltage at 1V/s, which has been known as the charge transfer process and a thermal annealing process of GFET at 300°C in N_2 has been demonstrated to eliminate this effect [141]. The Dirac Points changes from 0V to 15V as V_G sweeps forward and backward, respectively. Furthermore, under the n-type doping from the residual thin PEI layer, the maximum Dirac Point of the graphene channel is shifted from 80V of pristine graphene to 2.3V. A Dirac Point near zero helps the device operation to bias the GFET into either p-type or n-type region with low voltages without breaking down the gate dielectrics.

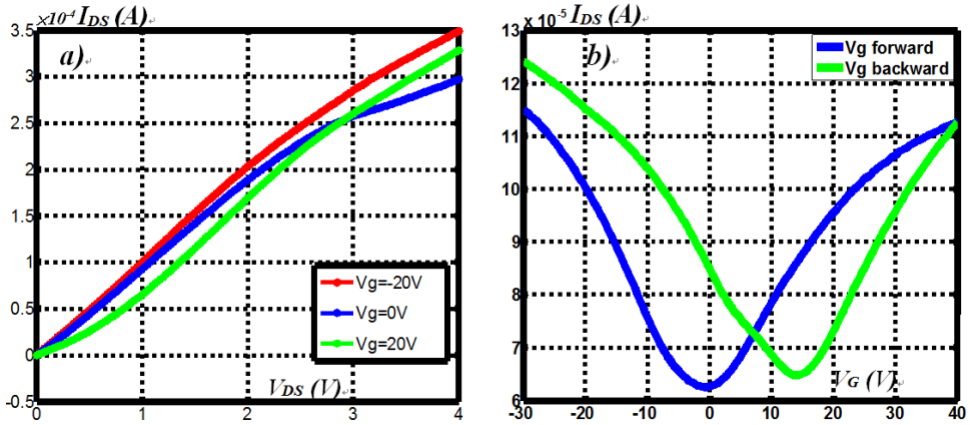

Figure 0.8 (a) channel resistance characterization and (b) the hysteresis effect of gate sweeping.

The sensing behavior is tested using the setup introduced above. The channel resistance of the flexible gas sensor responds to different concentrations of ammonia as shown in Figure 8.9, where the nitrogen purge process is used at each green arrow to remove ammonia under room temperature. The GFET is biased with V_G=-15V and V_{DS}=0.1V, and the majority carriers in the graphene channel are holes. During the adsorption phase, each ammonia molecule transfers one electron to the graphene channel, which decreases the major carrier density and increases the channel resistance. During desorption phase, nitrogen is purged into the chamber, and nearly half of the molecules can be detached from graphene surface quickly, while the rest of them follow a desorption process with a larger time constant. The sensitivity of the flexible graphene gas sensor is measured as 0.00428ppm^{-1}, which is calculated by using the term $\Delta R/R_0$, where ΔR is the difference between graphene channel resistance with and without the absorption of ammonia, and R_0 is the original graphene channel resistance without ammonia.

We also examine the gas sensor response under different gate voltages. Figure 8.10 illustrates the response of a flexible GFET gas sensor when exposed to 3500ppm of ammonia under different gate voltages.

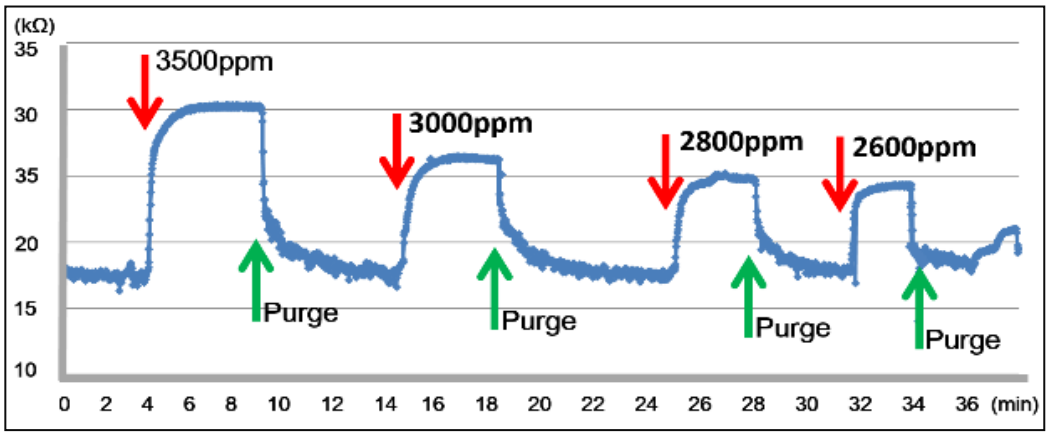

Figure 0.9 Gas (ammonia) sensing performance of the flexible graphene sensor.

1.36.4 Discussion

As shown in each figure, the intersection points between the R_{DS}-V_G curves and the vertical green line (working gate voltage) determine the channel resistance. As the R_{DS}-V_G curve shifts from the blue to red curve during the ammonia doping process, changes in the channel resistance (R_{DS}) are recorded and they behave differently under different gate voltages. For example, in Figure 8.10a, the graphene channel is biased with V_G=10V and the transition of channel resistance starts from the intersection of the blue and green line (blue point); follows the black vector on the blue line; and settles to a lower channel resistance at the red point. In Figures 8.10b and Figure 8.10c, the black vector increases initially to pass the Dirac Point, then settles at a higher and lower magnitude as compared to the initial resistance, respectively. It is noted that passing the Dirac Point results in a resistance peak in the corresponding R_{DS}-time measurement plots, and provides direct observation of n-type doping of graphene passing through the Dirac Point shift in real time. Figure 8.10d shows that under a negative gate voltage V_G=-15V, the channel resistance increased with time during the measurements in the R_{DS}-time curve.

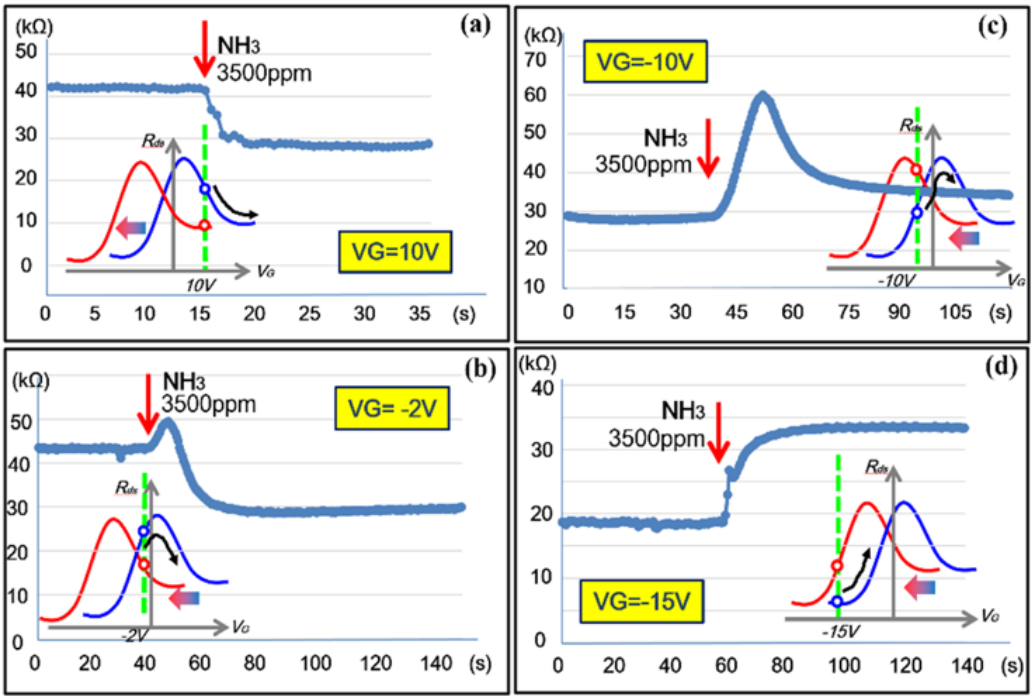

Figure 0.10 The gas sensing performance of graphene at gate voltage of (a) 10V, (b) -2V, (c) -10V and (d) -15V.

1.36.5 Conclusion

We have successfully demonstrated a flexible GFET gas sensor with a sensitivity of 0.00428ppm^{-1} for sensing the ammonia. Organic materials, including gate dielectric (170nm-thick parylene C layer), channel dopant (PEI), and substrate (40μm-thick polyimide) are used to construct the flexible GFETs. Experimental sensing measurements show fast adsorption/desorption process of ammonia purged at room temperature under various gas concentrations. The doping effects of ammonia molecule to graphene channel are further investigated in four different working regimes and the R_{DS}-time curves agree well with the analyses. Under a specific gate voltage bias, a peak of channel resistance appears in the transient response before R_{DS} settles at the final value, providing a direct observation of the transition of major carrier type at the Dirac Point due to the ammonia doping. Novel gas sensing application utilizing this phenomenon is under further investigation. This process is scalable for possible mass production of graphene based flexible sensors.

1.37 Direct Writing Electrospinning Technique for Graphene FET

1.37.1 Introduction

In recent years, graphene-based field effect transistors (GFET) have been reported to achieve devices with high cut off frequency, high on-off ratio [142] for applications in amplifiers and RF mixer [143,144]. However, most of these previous works used UV or e-beam lithography processes to define the graphene transistors. These rather complex processes could cause extra spaces between the

gate and source/drain regions, resulting in additional channel resistance [145]. Furthermore, the deposition of the inorganic gate dielectrics often requires surface functionalization with high temperature treatments, leading to undesired damages of graphene lattice [146]. Here, we propose a self-aligned, direct-write graphene transistor structure as illustrated in Figure 8.11a to alleviate these challenges by directly writing organic gate dielectrics on graphene and patterning source/drain and gate electrodes by way of self-alignment in Figure 8.11b.

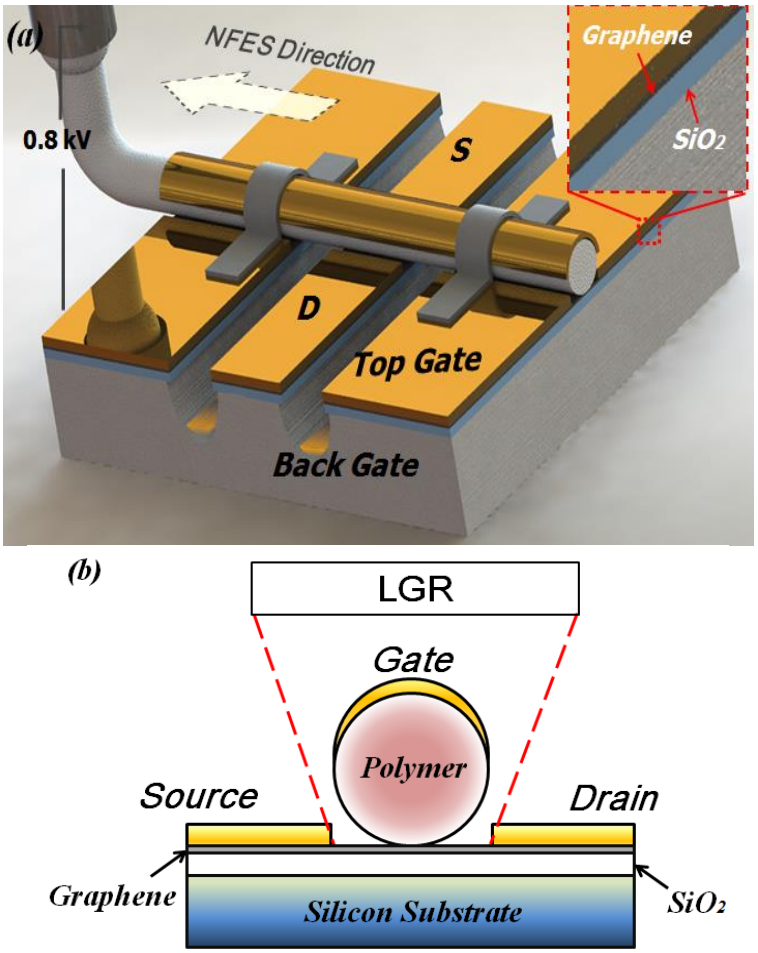

Figure 0.11, (a) Schematic of "direct-write" concept of patterning the gate dielectric for graphene FET. (b) Cross-sectional view of the "self-aligned" process for the top gate deposition.

1.37.2 Fabrication Process

The device fabrication process is illustrated in Figure 8.12. A 285nm-thick silicon dioxide layer was thermally grown on a p-type silicon wafer and a single layer graphene (grown separately using the CVD method) was transferred onto the substrate [147,148]. The quality of the single layer graphene is verified using Raman spectroscopy [149]. The device/contact areas were patterned (Figure 8.12a) and etched in oxygen plasma (50 Watts for 5 seconds) to remove graphene (Figure 8.12b). A dry-etched process (350 Watts for 1 mins in C_4F_8 plasma) was followed

to remove the oxide layer (Figure 8.12c). An isotropic, timed XeF_2 etching process was then used to remove part of the silicon to create undercuts of about 1μm (Figure 8.12d). This process provided good isolations between electrodes. In the prototype devices, a polyvinylidene fluoride (PVDF 20 wt%) fiber of 0.8μm in diameter was electrospun by means of near-field electrospinning under a voltage of 0.8 kV (Figure 8.12e). A blank metal deposition was followed with 2nm-thick chrome/10 nm-thick gold layer by e-beam evaporation (Figure 8.12f). Silver paste was then applied to the top-gate for electrical connection.

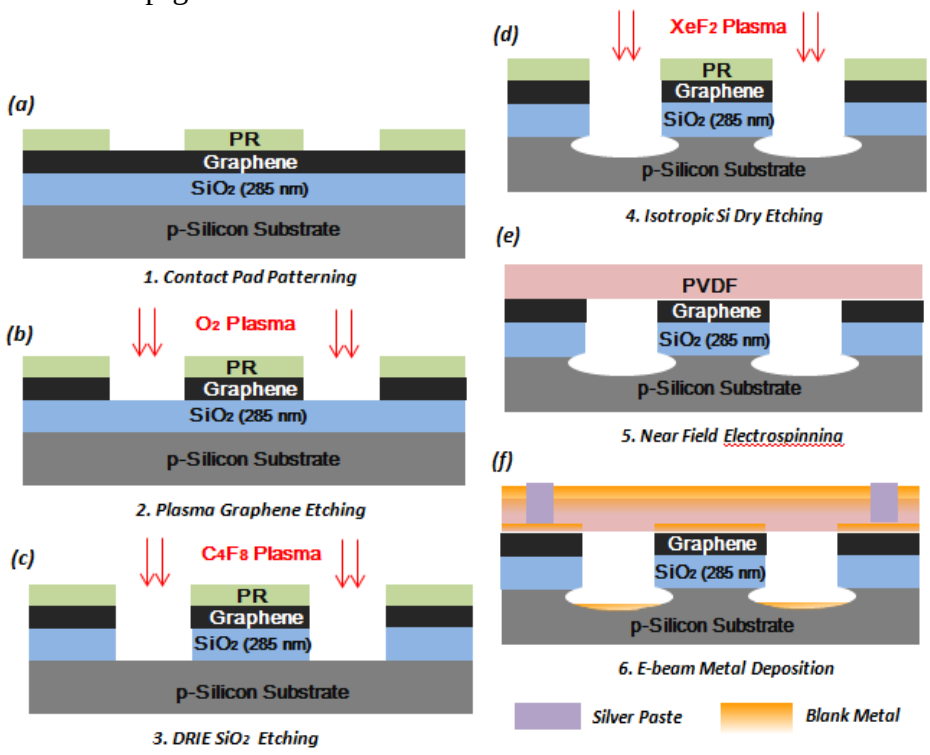

Figure 0.12 The fabrication process flow

1.37.3 Fabrication Results

Figure 8.13a shows the top view optical photo of the device after the near-field electrospinning process. Five possible electrode areas can be identified in this figure, including S (source), D (drain), TG#1 (top gate #1), TG#2 (top gate #2) and BG (back gate). The width of the graphene channel has also been defined in this process and two different widths, 10μm for *SAMPLE #1* and 100μm for *SAMPLE #2*, have been designed in the prototype devices. The length of the channel is the same as the diameter of the fiber which is 800 nm for the prototype devices. The timed isotropic silicon dry etching can create an undercut beneath the silicon dioxide layer. As such, some portions of the oxide film at the etching edges will be suspended after the etching process. Due to the possible residual stress effect, the suspended oxide layer has resulted in some natural curvature/optical effect as shown in Figure 8.13b. This undercut is designed to prevent electrical connection

between the silicon substrate (back gate) and the contact electrodes after the blank metal deposition process.

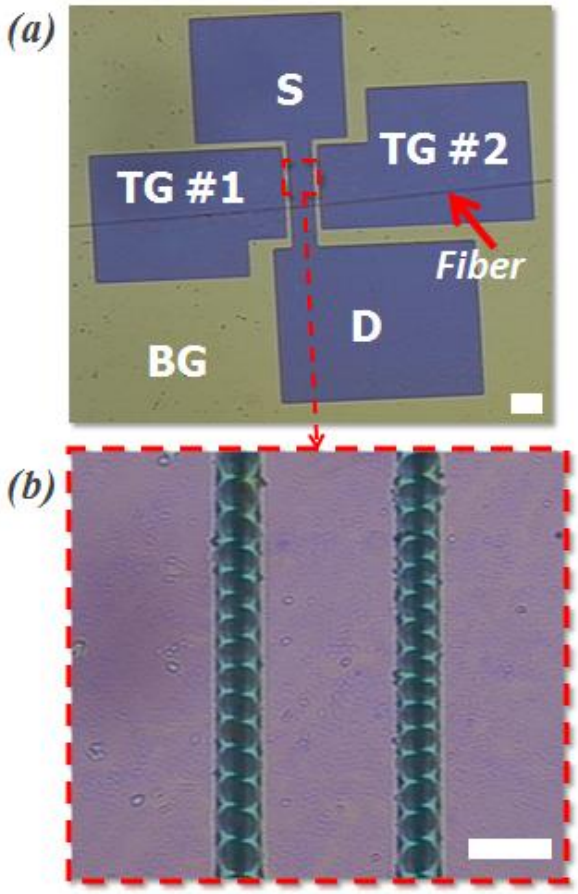

Figure 0.13 Optical microscope of the as-fabricated graphene transistor: (a) the optical image of the device (scale bar 100um) and (b) the zoom in view (scale bar 20um).

A good adhesion force between the polymer fibers and graphene substrate helped the fiber to stick to the substrate. However, after the gold deposition process, the adhesion force became weaker but the silver paste at both ends of the fiber seemed to provide good mechanical supports during the experiments without any fiber rotation or movement. Figure 8.14a shows the SEM image of the electrospun fiber lying across the contact pads from the *SAMPLE#2* and the isolation trenches separating the individual electrode regions can be clearly observed. A close-up SEM image is shown in Figure 8.14b where the trench has a design width of 4μm. The trench distance is designed to be as small as possible such that the mechanical strength of the polymer fiber can support itself to go across the gap. It is found that the gap distance can be as large as 10μm without affecting the rigidity of the polymer fiber to across the trench. The image shows clearly that the electrospun fiber has successfully defined the source and drain regions for a self-aligned graphene channel transistor. Furthermore, the suspended oxide/graphene layer close to the trench area has shown some slight curvature which is also observed in

the optical photo in Figure 8.13b. The metal layer on the top of the graphene area seems to be smooth while it is a bit rough on top of the polymer fiber.

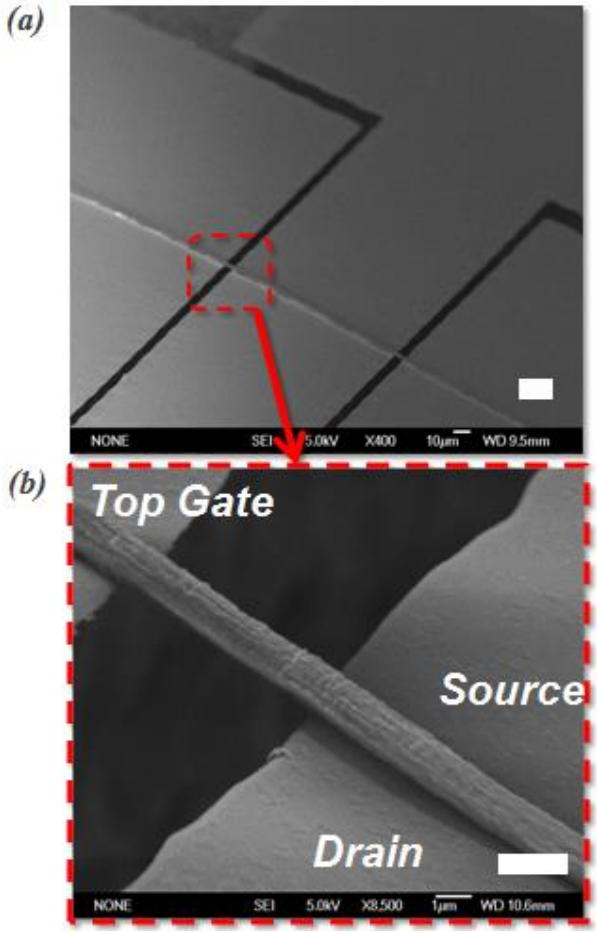

Figure 0.14 SEM picture of the single fiber on top of graphene (a) scale bar 10um and (b) zoom in view with scale bar 1um

1.37.4 Electrical Characterization

Experimentally, the I_{DS}-V_{DS} curve under different back gate voltage is measured and shown in Figure 8.15. The top gate is grounded through the measurement as shown in the inset. The linear response of each branch indicated a quasi-constant graphene channel resistance under each back gate voltage and ohmic contact between the gold electrode and graphene layer under V_{DS}<0.1V. No obvious channel current saturation is observed under V_{DS} as high as 1V. The slope of the curve reaches the local minimum when V_{BG}=-2V and shows a carrier mobility of 5056 cm^2/Vs given a typical carrier density of $n=10^{12}$ cm^{-2} at the Dirac Point. Figure 8.16 illustrates the I_{DS}-V_{GATE} transport characteristics of both top gate and back gate. As expected, the I_{DS}-V_{GATE} responses show the ambipolar symmetric behavior and reach the minimum current at the Dirac Point. Three regions (I, II, III) can be identified according to the Dirac Points of the two characteristic curves. As the $|V_{GATE}-V_{DIRAC}|$ increases, the electron concentration in the region I of top gate and region

I, II of back gate increases, as well as the holes concentration in the region II, III of top gate and region I of the back gate, resulting a V-shape trace. Compared to the back gate, the top gate has a smaller channel current at the Dirac Points. This could be the result of different LGR (local graphene region) between the dual gate operations. During the back gate operation, the whole distance between source and drain can be considered as active LGR. For the top gate operation, the effective LGR could be smaller than the default value of LGR as illustrated in Figure 8.12 due to circular geometric effects. This could lead the LGR of top gate to be smaller than that of the back gate as suggested by the experimental results in Figure 8.16.

The total carrier density inside the graphene channel can be approximated by [150]:

$$n_{total} = \sqrt{n_0^2 + n[V_{GATE}]^2} \tag{8.1}$$

where $n[V_{GATE}]$ is the gate induced channel carrier density and n_0 is the residual impurities which lead to a non-zero channel current at the Dirac Point. The gate induced carrier density can be further expressed by $n[V_{GATE}]=C_{GATE}(V_{GATE}-V_{DIRAC})$, where C_{total} is the total gate capacitance. The inset in Figure 8.15b indicates the serial relationship between C_{TG} (top gate dielectric capacitance), C_q (graphene channel quantum capacitance) and C_{BG} (back gate dielectric capacitance) during the operation. The gate capacitance equals to the serial of gate dielectric capacitance and a quantum capacitance which is ignored here for simplicity.

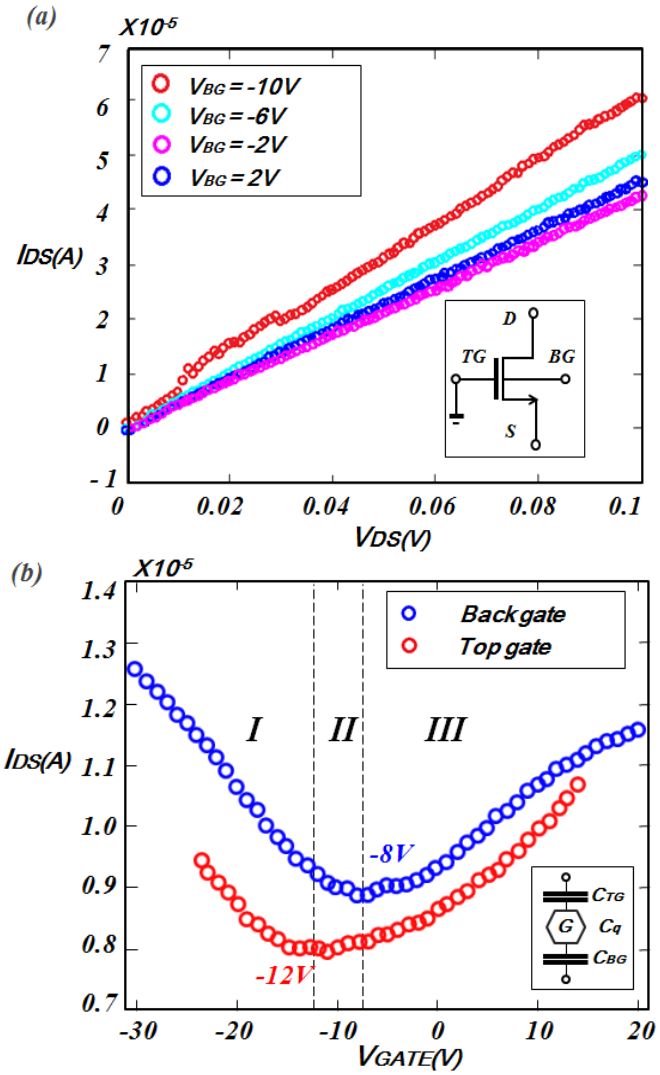

Figure 0.15(a) Graphene channel resistance characterization; (b) Dual gate operation of the "direct-write" + "self-aligned" graphene transistor.

1.37.5 Discussion

The horizontal shift of Dirac Point is observed in Figure 8.15b. This is because the residual impurities from the air could have doped the graphene as n-type [151], thus a negative gate voltage is required to neutralize the residual carrier Q_{res} to reach the Dirac Point. As $Q_{res}=C_{GATE}V_{GATE}$, a ratio of C_{TG}/C_{BG} will result in a similar ratio of $V_{DIRAC,BG}/ V_{DIRAC,TG}$. As shown in Figure 16, the COMSOL simulation of the top gate dielectric capacitance gives the electrical potential distribution between the hemi-cylindrical gold terminal and grounded graphene channel. An electrical potential of 1V is applied on the gold shell and a terminal charge of -6.79×10^{-16} C is calculated from the simulation results under $\varepsilon_r\approx1$ for air and $\varepsilon_r\approx7.9$ for PVDF. The calculated effective C_{TG} is 8.48×10^{-9} F/cm^2. The back gate capacitance, C_{BG} can be calculated as $\varepsilon_r\varepsilon_0/d_{SiO2}$, where d_{SiO2} is the thickness of the oxide layer. If one use ε_r as 3.9 for SiO_2, C_{BG} is calculates as 1.21×10^{-8} F/cm^2 and the ratio of C_{TG}/C_{BG} is

0.70 which corresponds well to the ratio of $V_{DIRAC,BG}/V_{DIRAC,TG}$, which is 0.66 in this case.

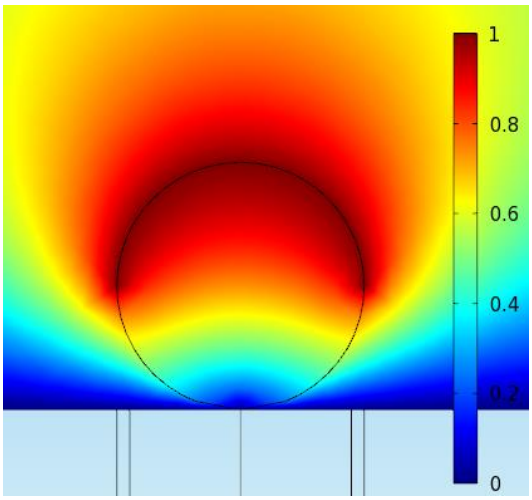

Figure 0.16 The cross-sectional view of the electrical field in the cylindrical dielectric using COMSOL.

1.37.6 Conclusion

Direct-write polymer fibers to construct self-aligned top gate graphene channel FET has been successfully demonstrated. The near-field electrospinning method was used to generate arbitrary pattern of PVDF fibers as the mask and the polymer fiber was used as the gate dielectrics for graphene channel FETs. Both conductance (I_{DS}/V_{DS}) and transconductance (I_{DS}/V_{GATE}) of the graphene FET have been measured and a carrier mobility of 5056 cm^2/Vs has been derived. Both vertical and horizontal shifts of the Dirac Points have been observed from the top and back gate operation results, and this could be the results of different LGR and different effective gate dielectric capacitance, respectively. In summary, a lithography-free process has been successfully developed to fabricate graphene FETs with submicron channel length as well as self-aligned source/drain regions. This simple, fast, and effective process could provide new opportunities for further mass production of graphene based electronics

Conclusion and Future Directions

The gas sensing techniques based on graphene FETs in this thesis provide ultrasensitive, miniaturized and low power platforms for potential gas sensing applications. This research area has drawn a lot of attentions and interests from both the scientific community and the sensor industry. With the core challenges of graphene gas sensing being the selectivity and recovery speed, this thesis focuses on proposing new methods and concepts to address these issues.

For improving the gas selectivity, we proposed three major approaches: noise, linear factor, and scattering strength. In this thesis, the core concept behind the proposed selective sensing methods is to characterize the multi-molecule adsorption events by the averaged single molecule adsorption event, such that the measurement results can deliver characteristic insights at the single molecule level. This is because each gas molecule absorbed on graphene has unique amount of charge. In particular, both the linear factor concept introduced in Chapter 3 and scattering strength concept introduced in Chapter 4 studied the number of "charges" carried by each gas molecule adsorbed on graphene. For the noise PSD method, the specific quantity we probed is related to the concentration of molecule as well as the desorption energy. We believe the accurate and practical measurements of these physicochemical properties (i.e. mass, charge and electron affinity) at averaged single molecule level can unlock the potential of achieving selective gas sensing at ambient temperature.

On the other hand, we improved the recovery speed of graphene FET through the phase sensing method. We leveraged the unique sensing property of the phase signal to avoid the signal component of the defect-induced sluggish responses, and selectively project the sensing plane away from the graphene surface. This method is effective in boosting the recovery speed because the fundamental dilemma of slow recovery speed lies in the defect-rich surface of CVD graphene. We demonstrated experimentally that such method significantly improves the recover speed of graphene FET into tens of seconds – more than 10 times of reduction as compared to previous works.

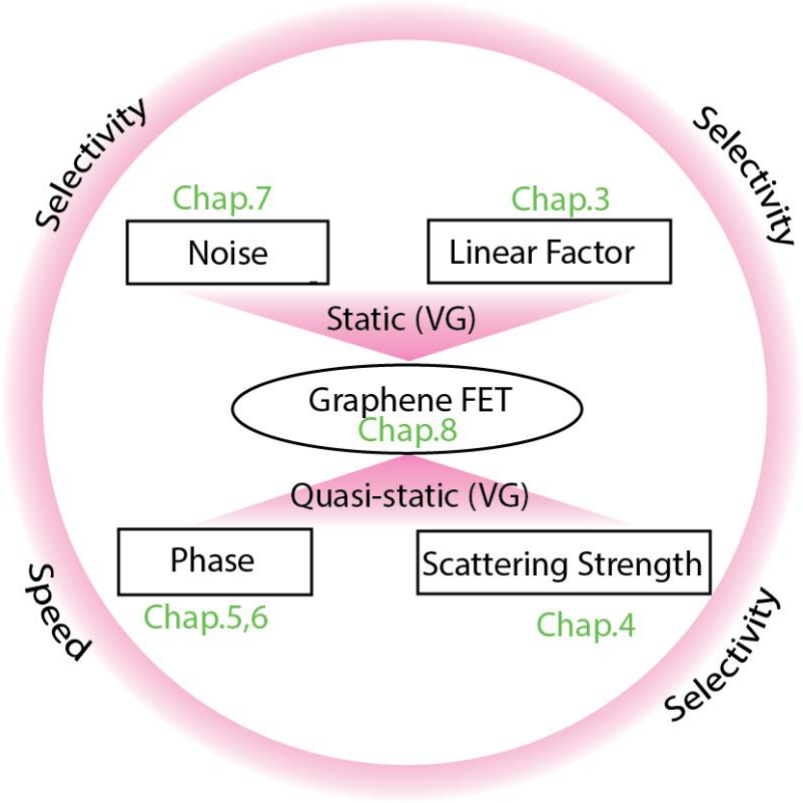

Figure 0.1 Summary of the thesis

As summarized in Figure 9.1, the experimental procedures of the electrical measurements in this thesis can be generally divided into two major approaches of gate modulation: static gate voltage and quasi-static gate voltage. In static gate voltage, we applied the DC gate voltage on the graphene FET, and explored the noise PSD method and linear factor concept to enhance the gas selectivity. On the other hand, we proposed the quasi-static method with AC+DC gate voltage biased on graphene FET, and studied the scattering strength and the phase of charge transfers for boosted selectivity and recovery speed, respectively. As the static method requires less power supply and is simple in signal process, it fits well for the application where the power and size of the sensor is limited.

In summary, this research lays the foundation for potential industrial applications of graphene FET in (a) advanced gas sensing capability with various applications, (b) new ways to achieve gas selectivity and fast responses with the assistance of microelectronics and MEMS. The results shown in this thesis could open a new area in the gas sensing by means of electric tuning of ultra-sensitive 2D films. We expect this field to continually attract researchers from materials, microelectronics, MEMS, and nanotechnology to advance the innovative sensing systems and materials based on research results from this project for now and future years.

1.38 Future directions

The future work of this thesis may move into the following three directions: (1) combing advanced graphene sensing techniques with sensitizer for improved performance; (2) combining advanced graphene sensing techniques with machine learning to form robust recognition system for gas mixture detection; and (3) developing wafer level fabrication and packaging process for graphene FET gas sensor.

For the first future direction, we want to answer the question if the fundamental sensing process of graphene can be promoted by adding another layer of sensitizer. For example, we have demonstrated the pre-compensation method using the gas adsorbents on graphene for eliminating the defect-induced adsorption in Chapter 4, and the results inspired us to explore more methods to compensate graphene to achieve the gas adsorption on graphene with fast and selective responses.

For the second future direction, we aim at improving the sensing selectivity by adding another layer of recognition for graphene FET using machine learning techniques. We are inspired by the mammal olfaction system, which is a three-layer neuron network with hundreds of odorant receptors, and we want to verify if such system can be mimicked by the combination of graphene FETs and neuron network. The marriage of the tunable, cross-reactive and sensitive graphene FET and neuron network may bring up new opportunities in advanced gas sensing system.

For the third future direction, we want to show that the graphene FETs can be made by large scale manufacturing process with possible direct integration to the standard microelectronics for low manufacturing costs. At the moment, we plan to develop the integration process by using a 0.35 um CMOS (Complementary Metal Oxide Semiconductor) standard process that has been running continuously in our microfabrication lab at UC-Berkeley as the foundation for microelectronics. We expect to face engineering challenges for the integration process and certain modifications and alternations will likely to occur to implement the concept. However, we are confident about the basic concept as some of the commercially available accelerometers have been based on similar process flows with post-CMOS processes and process steps after the graphene deposition have already been validated in our prototype fabrication results.

Bibliography

[1] Geim, Andre K., and Konstantin S. Novoselov. "The rise of graphene." Nature materials 6.3 (2007): 183-191.

[2] Bhimanapati, G. R., et al. (2015). "Recent Advances in Two-Dimensional Materials beyond Graphene." ACS Nano 9(12): 11509-11539.

[3] F. Schedin et al., “Detection of individual gas molecules adsorbed on graphene.,” Nat. Mater., vol. 6, no. 9, pp. 652–655, 2007.

[4] Hwang, E. H., S. Adam, and S. Das Sarma. "Transport in chemically doped graphene in the presence of adsorbed molecules." Physical Review B 76.19 (2007): 195421.

[5] I.-S. Kang, H.-M. So, G.-S. Bang, J.-H. Kwak, J.-O. Lee, and C. Won Ahn, “Recovery improvement of graphene-based gas sensors functionalized with nanoscale heterojunctions,” Appl. Phys. Lett., vol. 101, no. 12, p. 123504, Sep. 2012.

[6] B. Kumar et al., “The Role of external defects in chemical sensing of graphene field-effect transistors,” Nano Lett., vol. 13, no. 5, pp. 1962–1968, 2013.

[7] K. R. Nemade and S. A. Waghuley, “Role of defects concentration on optical and carbon dioxide gas sensing properties of Sb2O3/graphene composites,” Opt. Mater. (Amst)., vol. 36, no. 3, pp. 712–716, 2014.

[8] Ko, G., et al. "Graphene-based nitrogen dioxide gas sensors." Current Applied Physics 10.4 (2010): 1002-1004.

[9] Choi, Hongkyw, et al. "Flexible and transparent gas molecule sensor integrated with sensing and heating graphene layers." Small 10.18 (2014): 3685-3691.

[10] G. Peng, U. Tisch, O. Adams, M. Hakim, N. Shehada, Y. Y. Broza, S. Billan, R. Abdah-Bortnyak, A. Kuten, and H. Haick, “Diagnosing lung cancer in exhaled breath using gold nanoparticles.,” Nat. Nanotechnol., vol. 4, no. 10, pp. 669–673, 2009.

[11] Moser, Joel, Amelia Barreiro, and Adrian Bachtold. "Current-induced cleaning of graphene." Applied Physics Letters 91.16 (2007): 163513.

[12] J.-H. Chen, C. Jang, S. Adam, M. S. Fuhrer, E. D. Williams, and M. Ishigami, “Charged-impurity scattering in graphene,” Nature Physics, vol. 4, no. 5. pp. 377–381, 2008.

[13] P. R. Bueno, F. Fabregat-Santiago, and J. J. Davis, “Elucidating Capacitance and Resistance Terms in Confined Electroactive Molecular Layers,” Anal. Chem., vol. 85, no. 1, pp. 411–417, Jan. 2013.

[14] Y.-J. Yu, Y. Zhao, S. Ryu, L. E. Brus, K. S. Kim, and P. Kim, “Tuning the graphene work function by electric field effect.” Nano Lett., vol. 9, no. 10, pp. 3430–4, 2009.

[15] G. Binnig, H. Rohrer, C. Gerber, and E. Weibel, “Surface Studies by Scanning Tunneling Microscopy,” Phys. Rev. Lett., vol. 49, no. 1, pp. 57–61, Jul. 1982.

[16] Y. Liu, S. Lin and L. Lin, "A Versatile Gas Sensor with Selectivity Using a Single Graphene Transistor," 18th International Conference on Solid-State

Sensors, Actuators and Microsystems Transducers 2015, pp. 961-964, Anchorage Alaska, June 2015.
[17] Y. Liu, H. Liu, Y. Chu, Y. Cui, T. Hayasaka, L. Nguyen, V. Dasika, and L. Lin, “Defect Induced Gas Adsorption on Graphene Transistors”, submitted
[18] Y. Liu, H. Liu, T. Hayasaka, Y. Cui, X. Li, K. Hu, L. Lin, V. Dasika and L. Nguyen, "A Phase Sensitive Measurement Technique for Boosted Response Speed of Graphene FET Gas Sensor," 2017 IEEE 67th Electronic Components and Technology Conference, Orlando, Florida, USA.
[19] Y. Liu, J. Yu, Y. Chui, T. Hayasaka, H. Lui, X. Li and Liwei Lin, "An AC Sensing Scheme for Minimal Baseline Drift and Fast Recovery on Graphene FET Gas Sensor," 19th International Conference on Solid-State Sensors, Actuators and Microsystems Transducers 2017, pp. 230-233, Kaohsiung, Taiwan, June 2017.
[20] Y. Cui, Y. Liu, J. Yu, T. Hayasaka, X. Li, W. Cai, H. Liu, and Liwei Lin, "Low-Frequency Electronic Noises in CVD Graphene Gas Sensors," 19th International Conference on Solid-State Sensors, Actuators and Microsystems Transducers 2017, pp. 246-249, Kaohsiung, Taiwan, June 2017..
[21] Y. Liu, J. Chang, and L. Lin, "A Flexible Graphene FET Gas Sensor Using Polymer as Gate Dielectrics," Proceedings of 27th IEEE Micro Electro Mechanical Systems Conference, pp. 230-233, San Francisco, Jan. 2014.
[22] Y. Liu, J. Chang, H. Yang, S. Lin, S. Akhbari, Q. Zhou, K. Heo and L. Lin "Self-Aligned, Direct-Write Graphene Channel FETs," Proceedings of the 17th International Conference on Solid-State Sensors, Actuators and Microsystems," pp. 1119-1122, Barcelona, Spain, June 2013.
[23] https://en.wikipedia.org/wiki/Mass_spectrometry
[24] S. C. Terry, J. H. Jerman, and J. B. Angell, “A gas chromatographic air analyzer fabricated on a silicon wafer,” IEEE Trans. Electron Devices, vol. ED-26, pp. 1880–1886, 1979.
[25] R. R. Reston and E. S. JR. Kolesar, “Silicon-micromachined gas chromatography system used to separate and detect ammonia and nitrogen dioxide. Part I: design, fabrication, and integration of the gas chromatography system,” Journal of Microelectromechanical Systems, vol. 3, no. 4, pp. 134–146, 1994.
[26] J.-B. Sanchez, F. Berger, M. Fromm, and M.-H. Nadal, “Use of a chromatographic column to improve the selectivity of the SnO2 gas sensors: first approach towards a miniaturised device and selective with hydrogen fluoride vapours,” Sensors and Actuators B, vol. 106, no. 2, pp. 823–831, 2005.
[27] M. Agah, and K. D. Wise, “Low-Mass PECVD Oxynitride Gas Chromatographic Columns,” Journal of Microelectromechanical Systems, Vol. 16, pp. 853-860, 2007
[28] A. D. Radadia, R. I. Masel, M. A. Shannon, J. P. Jerrell, and K. R. Cadwallade, “Micromachined GC Columns for Fast Separation of Organophosphonate and Organosulfur Compounds,” Anal. Chem., Vol. 80, pp. 4087–4094, 2008.

[29] Z. Ouyang, and R. G. Cooks, “Miniature Mass Spectrometers,” Annual Rev. Anal. Chem. Vol. 2, pp.187-214, 2009.
[30] U. Lange and V. M. Mirsky, “Integrated electrochemical transistor as a fast recoverable gas sensor,” Anal. Chim. Acta, vol. 687, no. 1, pp. 7–11, 2011.
[31] S. Raible, D. Briand, J. Kappler, and N. F. De Rooij, “Wafer Level Packaging of Micromachined Gas Sensors,” IEEE Sens. J., vol. 6, no. 5, pp. 746–748, 2006.
[32] J. Y. Wong and R. L. Anderson, Non-Dispersive Infrared Gas Measurement. Lulu.com, 2012.
[33] https://en.wikipedia.org/wiki/Electronic_nose
[34] A. D. Wilson, and M. Baietto, “Applications and Advances in Electronic-Nose Technologies,” Sensors, Vol. 9, pp. 5099–5148, 2009.
[35] http://www.celebritydiagnosis.com/2014/07/new-kind-pet-scan-detecting-ovarian-cancer/
[36] S. M. Scott, D. James, and Z. Ali, “Data Analysis for Electronic Nose Systems,” Microchim Acta, Vol. 156, pp. 183–207, 2007.
[37] R. Dutta, E.L. Hines, J.W. Gardner, K.R. Kashwan, and M. Bhuyan, “Tea Quality Prediction Using a Tin Oxide-based Electronic Nose: an Artificial Intelligence Approach,” Sensors and Actuators B 94, pp. 228–237, 2003.
[38] N. E. Barbri, A. Amari, M. Vinaixa, B. Bouchikhi, X. Correig, E. Llobet, “Building of a Metal Oxide Gas Sensor-based Electronic Nose to Assess the Freshness of Sardines under Sold Storage,” Sensors and Actuators B, Vol. 128, pp. 235–244, 2007.
[39] Amalia Berna, “Metal Oxide Sensors for Electronic Noses and Their Application to Food Analysis,” Sensors, Vol. 10, pp. 3882-3910, 2010.
[40] P.-C. Chen, G. Shen, and C. Zhou, “Chemical Sensors and Electronic Noses Based on 1-D Metal Oxide Nanostructures,” IEEE Transactions on Nanotechnology, Vol. 7, pp. 668-632, 2008.
[41] K. Arshak E. Moore G.M. Lyons J. Harris and S. Clifford, “A review of gas sensors employed in electronic nose applications,” Sensor Review, Vol. 24, pp. 181–198, 2004.
[42] N. Barsan and U. Weimar, “Conduction Model of Metal Oxide Gas Sensors,” Journal of Electroceramics, Vol. 7, pp. 143–167, 2001.
[43] C. Wang, L. Yin, L. Zhang, D. Xiang and R. Gao, “Metal Oxide Gas Sensors: Sensitivity and Influencing Factors,” Sensors, Vol. 10, pp.2088-2106, 2010.
[44] H. Q. Liu, "Polymeric nanowire chemical sensor," Nano Letters, vol. 4, pp. 671-675, 2004.
[45] P. R. Nair and M. A. Alam, "Performance limits of nanobiosensors," Applied Physics Letters, vol. 88, 2006.
[46] K. S. Novoselov, "Electric field effect in atomically thin carbon films," Science, vol. 306, pp. 666-9, 2004.
[47] K. S. Novoselov, "Two-dimensional gas of massless Dirac fermions in graphene," Nature, vol. 438, pp. 197-200, Nov 10 2005.
[48] Y. Zhang, "Experimental observation of the quantum Hall effect and Berry's phase in graphene," Nature, vol. 438, pp. 201-4, 2005.
[49] K. S. Novoselov, "Two-dimensional atomic crystals," Proceedings of the

National Academy of Sciences of the United States of America, vol. 102, pp. 10451-10453, 2005.
[50] A. K. Geim and K. S. Novoselov, "The rise of graphene," Nature Materials, vol. 6, pp. 183-191, 2007.
[51] R. F. Service, "MATERIALS SCIENCE Carbon Sheets an Atom Thick Give Rise to Graphene Dreams," Science, vol. 324, pp. 875-877, May 15 2009.
[52] P. Dutta and P. M. Horn, "Low-Frequency Fluctuations in Solids - 1-F Noise," Reviews of Modern Physics, vol. 53, pp. 497-516, 1981.
[51] W. Yuan, "Graphene-based gas sensors", Journal of Material Chemistry A, 2013, 1, 10078-10091
[52] F. Schedin, "Detection of individual gas molecules absorbed on graphene", Nature Materials, 2007, 6, pp. 652 - 655
[53] Y. Liu, "A Flexible Graphene FET Gas Sensor Using Polymer as Gate Dielectrics", 2014 IEEE 27th International Conference on Micro Electro Mechanical Systems (MEMS), pp.230-233, San Francisco, Jan. 2013.
[54] M. Qazi, T. Vogt, G. Koley, "Two-dimensional signatures for molecular identification", Applied Physcis Letters 92, 103120, 2008
[55] S. Rumyantsev, G. Liu, A. Baladin, "Selective Gas Sensing with A Single Pristine Graphene Transistor", Nano Lett. 12, 2294-2298, 2012
[56] S. Adam, "A Self-consistent theory of graphene transport", Proceedings of the National Academy of Sciences of the United States of Americal, 2007, vol. 104 No.47, 18392-18397
[57] J. Chen, "Charged-impurity scattering in graphene", Nature Physics, 4(2008) pp.377-381
[58] F. Xia, "The origins and limits of metal-graphene junction resistance", Nature Nanotechnology, 6(2011) pp.179-184
[59] H. E. Romero et al., "Adsorption of ammonia on graphene," Nanotechnology, vol. 20, no. 24, p. 245501, 2009.
[60]T. O. Wehling et al., "Molecular doping of graphene," Nano Lett., vol. 8, no. 1, pp. 173–177, 2008.
[61] Y.-J. Yu, Y. Zhao, S. Ryu, L. E. Brus, K. S. Kim, and P. Kim, "Tuning the Graphene Work Function by Electric Field Effect," Nano Lett., vol. 9, no. 10, pp. 3430–3434, Oct. 2009.
[62] S. Adam, E. H. Hwang, V. M. Galitski, and S. Das Sarma, "A self-consistent theory for graphene transport.," Proc. Natl. Acad. Sci. U. S. A., vol. 104, no. 47, pp. 18392–18397, 2007.
[63] S. Das Sarma, S. Adam, E. H. Hwang, and E. Rossi, "Electronic transport in two-dimensional graphene," Rev. Mod. Phys., vol. 83, no. 2, pp. 407–470, 2011.
[64] M. Muruganathan, J. Sun, T. Imamura, and H. Mizuta, "Electrically Tunable van der Waals Interaction in Graphene-Molecule Complex," Nano Lett., vol. 15, no. 12, pp. 8176–8180, 2015.
[65] H. Liu, Y. Liu, and D. Zhu, "Chemical doping of graphene," J. Mater. Chem., vol. 21, no. 10, p. 3335, 2011.
[66] J. Xia, F. Chen, J. Li, and N. Tao, "Measurement of the quantum capacitance of graphene.," Nat. Nanotechnol., vol. 4, no. 8, pp. 505–509, 2009.

[67] E. H. Hwang, S. Adam, and S. Das Sarma, “Transport in chemically doped graphene in the presence of adsorbed molecules,” Phys. Rev. B, vol. 76, no. 19, p. 195421, Nov. 2007.
[68] J.-H. Chen, C. Jang, S. Adam, M. S. Fuhrer, E. D. Williams, and M. Ishigami, “Charged-impurity scattering in graphene,” Nature Physics, vol. 4, no. 5. pp. 377–381, 2008.
[69] S.-Z. Liang, G. Chen, A. R. Harutyunyan, and J. O. Sofo, “Screening of charged impurities as a possible mechanism for conductance change in graphene gas sensing,” Phys. Rev. B, vol. 90, no. 11, p. 115410, Sep. 2014.
[70] H. H. Pu, S. H. Rhim, M. Gajdardziksa-Josifovska, C. J. Hirschmugl, M. Weinert, and J. H. Chen, “A statistical thermodynamics model for monolayer gas adsorption on graphene-based materials: implications for gas sensing applications,” RSC Adv., vol. 4, no. 88, pp. 47481–47487, 2014.
[71] H. Pinto, R. Jones, J. P. Goss, and P. R. Briddon, “Mechanisms of doping graphene,” Phys. status solidi, vol. 207, no. 9, pp. 2131–2136, Sep. 2010.
[72] W. Chen, D. Qi, X. Gao, and A. T. S. Wee, “Surface transfer doping of semiconductors,” Prog. Surf. Sci., vol. 84, no. 9–10, pp. 279–321, 2009.
[73] T. Ando, “Screening effect and impurity scattering in monolayer graphene,” J. Phys. Soc. Japan, vol. 75, no. 7, pp. 1–7, 2006.
[74] G. Paasch and S. Scheinert, “Charge carrier density of organics with Gaussian density of states: Analytical approximation for the Gauss–Fermi integral,” J. Appl. Phys., vol. 107, no. 10, p. 104501, May 2010.
[75] P. A. Denis and F. Iribarne, “Comparative study of defect reactivity in graphene,” J. Phys. Chem. C, vol. 117, no. 37, pp. 19048–19055, Sep. 2013.
[76] R. Lv et al., “Ultrasensitive gas detection of large-area boron-doped graphene,” Proc. Natl. Acad. Sci. U. S. A., vol. 112, no. 47, pp. 14527–32, Nov. 2015.
[77] P. L. Levesque et al., “Probing charge transfer at surfaces using graphene transistors,” Nano Lett., vol. 11, no. 1, pp. 132–137, 2011.
[78] P. R. Bueno, F. Fabregat-Santiago, and J. J. Davis, “Elucidating capacitance and resistance terms in confined electroactive molecular layers,” Anal. Chem., vol. 85, no. 1, pp. 411–417, Jan. 2013.
[79] J.-H. Chen, C. Jang, S. Adam, M. S. Fuhrer, E. D. Williams, and M. Ishigami, “Charged-impurity scattering in graphene,” Nature Physics, vol. 4, no. 5. pp. 377–381, 2008.
[80] Y. Liu, S. Lin, and L. Lin, “A versatile gas sensor with selectivity using a single graphene transistor,” in the 18th International Conference on Solid-State Sensors, Actuators and Microsystems, TRANSDUCERS 2015, 2015, pp. 961–964.
[81] S. Adam, E. H. Hwang, V. M. Galitski, and S. Das Sarma, “A self-consistent theory for graphene transport,” Proc. Natl. Acad. Sci. U. S. A., vol. 104, no. 47, pp. 18392–18397, 2007
[82] J. Moser, A. Barreiro, A. Bachtold, Current-induced cleaning of graphene, Applied Physics Letters, 91(2007) 163513.
[83] J.H. Chen, C. Jang, S. Adam, M.S. Fuhrer, E.D. Williams, M. Ishigami, Charged-impurity scattering in graphene, Nat Phys, 4(2008) 377-81.

[84] P.R. Bueno, F. Fabregat-Santiago, J.J. Davis, Elucidating capacitance and resistance terms in confined electroactive molecular layers, Analytical chemistry, 85(2012) 411-7.
[85] Y.-J. Yu, Y. Zhao, S. Ryu, L.E. Brus, K.S. Kim, P. Kim, Tuning the graphene work function by electric field effect, Nano letters, 9(2009) 3430-4.
[86] G. Binnig, H. Rohrer, C. Gerber, E. Weibel, Surface studies by scanning tunneling microscopy, Physical review letters, 49(1982) 57.
[87] J.M. Crowley, Simple expressions for force and capacitance for a conductive sphere near a conductive wall, Proceedings of the ESA Annual Meeting on Electrostatics2008, p. 1.
[88] C. Sun, B. Bai, Gas diffusion on graphene surfaces, Physical Chemistry Chemical Physics, 19(2017) 3894-902.
[89] A. Pal, A. Bol, A. Ghosh, Large low-frequency resistance noise in chemical vapor deposited graphene, Applied Physics Letters. 97 (2010) 133504. doi:10.1063/1.3493655.
[100] Qinghui Shao, Guanxiong Liu, D. Teweldebrhan, A. Balandin, S. Rumyantsev, M. Shur et al., Flicker Noise in Bilayer Graphene Transistors, IEEE Electron Device Letters. 30 (2009) 288-290. doi:10.1109/led.2008.2011929.
[101] G. Liu, W. Stillman, S. Rumyantsev, Q. Shao, M. Shur, A. Balandin, Low-frequency electronic noise in the double-gate single-layer graphene transistors, Applied Physics Letters. 95 (2009) 033103. doi:10.1063/1.3180707.
[102] K. Bedner, V. Guzenko, A. Tarasov, M. Wipf, R. Stoop, S. Rigante et al., Investigation of the dominant 1/f noise source in silicon nanowire sensors, Sensors And Actuators B: Chemical. 191 (2014) 270-275. doi:10.1016/j.snb.2013.09.112.
[103] U. Cindemir, M. Trawka, J. Smulko, C. Granqvist, L. Österlund, G. Niklasson, Fluctuation-enhanced and conductometric gas sensing with nanocrystalline NiO thin films: A comparison, Sensors And Actuators B: Chemical. 242 (2017) 132-139. doi:10.1016/j.snb.2016.11.015.
[104] G. Liu, S. Rumyantsev, M. Bloodgood, T. Salguero, M. Shur, A. Balandin, Low-Frequency Electronic Noise in Quasi-1D TaSe3 van der Waals Nanowires, Nano Letters. 17 (2017) 377-383. doi:10.1021/acs.nanolett.6b04334.
[105] C. Jakobson, M. Feinsod, Y. Nemirovsky, Low frequency noise and drift in Ion Sensitive Field Effect Transistors, Sensors And Actuators B: Chemical. 68 (2000) 134-139. doi:10.1016/s0925-4005(00)00473-1.
[106] S. Peng, Z. Jin, D. Zhang, J. Shi, D. Mao, S. Wang et al., Carrier-Number-Fluctuation Induced Ultralow 1/f Noise Level in Top-Gated Graphene Field Effect Transistor, ACS Applied Materials & Interfaces. 9 (2017) 6661-6665. doi:10.1021/acsami.6b15862.
[107] Z. Cheng, Q. Li, Z. Li, Q. Zhou, Y. Fang, Suspended Graphene Sensors with Improved Signal and Reduced Noise, Nano Letters. 10 (2010) 1864-1868. doi:10.1021/nl100633g.
[108] G. Liu, S. Rumyantsev, M. Shur, A. Balandin, Graphene thickness-graded

transistors with reduced electronic noise, Applied Physics Letters. 100 (2012) 033103. doi:10.1063/1.3676277.
[109] H. Arnold, V. Sangwan, S. Schmucker, C. Cress, K. Luck, A. Friedman et al., Reducing flicker noise in chemical vapor deposition graphene field-effect transistors, Applied Physics Letters. 108 (2016) 073108. doi:10.1063/1.4942468.
[110] Y. Lin, P. Avouris, Strong Suppression of Electrical Noise in Bilayer Graphene Nanodevices, Nano Letters. 8 (2008) 2119-2125. doi:10.1021/nl080241l.
[111] L. Kish, R. Vajtai, C. Granqvist, Extracting information from noise spectra of chemical sensors: single sensor electronic noses and tongues, Sensors And Actuators B: Chemical. 71 (2000) 55-59. doi:10.1016/s0925-4005(00)00586-4.
[112] B. Ayhan, C. Kwan, J. Zhou, L. Kish, K. Benkstein, P. Rogers et al., Fluctuation enhanced sensing (FES) with a nanostructured, semiconducting metal oxide film for gas detection and classification, Sensors And Actuators B: Chemical. 188 (2013) 651-660. doi:10.1016/j.snb.2013.07.056.
[113] Ederth, J. Smulko, L. Kish, P. Heszler, C. Granqvist, Comparison of classical and fluctuation-enhanced gas sensing with PdxWO3 nanoparticle films, Sensors And Actuators B: Chemical. 113 (2006) 310-315. doi:10.1016/j.snb.2005.03.009.
[114] S. Rumyantsev, M. Shur, G. Liu, A. Balandin, Low frequency noise in 2D materials: Graphene and MoS2, 2017 International Conference On Noise And Fluctuations (ICNF). (2017). doi:10.1109/icnf.2017.7985949.
[115] A. Balandin, Low-frequency 1/f noise in graphene devices, Nature Nanotechnology. 8 (2013) 549-555. doi:10.1038/nnano.2013.144. 8和25重
[116] G. Liu, S. Rumyantsev, C. Jiang, M. Shur, A. Balandin, Selective Gas Sensing With h -BN Capped MoS2 Heterostructure Thin-Film Transistors, IEEE Electron Device Letters. 36 (2015) 1202-1204. doi:10.1109/led.2015.2481388.
[117] S. Rumyantsev, G. Liu, R. Potyrailo, A. Balandin, M. Shur, Selective Sensing of Individual Gases Using Graphene Devices, IEEE Sensors Journal. 13 (2013) 2818-2822. doi:10.1109/jsen.2013.2251627.
[118] S. Rumyantsev, G. Liu, M. Shur, R. Potyrailo, A. Balandin, Selective Gas Sensing with a Single Pristine Graphene Transistor, Nano Letters. 12 (2012) 2294-2298. doi:10.1021/nl3001293.
[119] K. Amin, A. Bid, Effect of ambient on the resistance fluctuations of graphene, Applied Physics Letters. 106 (2015) 183105. doi:10.1063/1.4919793.
[120] K. Amin, A. Bid, High-Performance Sensors Based on Resistance Fluctuations of Single-Layer-Graphene Transistors, ACS Applied Materials & Interfaces. 7 (2015) 19825-19830. doi:10.1021/acsami.5b05922.
[121] S. Dana, M. Varma, Gas-Selective Signal Amplification in Fluctuation-Based Graphene FET Sensors, IEEE Sensors Journal. 16 (2016) 6533-6536. doi:10.1109/jsen.2016.2585739.
[122] J. Chen, C. Jang, S. Adam, M. Fuhrer, E. Williams, M. Ishigami, Charged-impurity scattering in graphene, Nature Physics. 4 (2008) 377-381.

doi:10.1038/nphys935.
[123] L. Vandamme, F. Hooge, On the additivity of generation-recombination spectra Part 3: The McWhorter model for 1/f noise in MOSFETs, Physica B: Condensed Matter. 357 (2005) 507-524. doi:10.1016/j.physb.2004.09.106.
[124] P. Karnatak, T. Paul, S. Islam, A. Ghosh, 1 / f noise in van der Waals materials and hybrids, Advances In Physics: X. 2 (2017) 428-449. doi:10.1080/23746149.2017.1314192.
[125] S. Rumyantsev, G. Liu, W. Stillman, M. Shur, A. Balandin, Electrical and noise characteristics of graphene field-effect transistors: ambient effects, noise sources and physical mechanisms, Journal Of Physics: Condensed Matter. 22 (2010) 395302. doi:10.1088/0953-8984/22/39/395302.
[126] The 15th International Conference on Solid-State Sensors: Actuators and Microsystems, IEEE Electron Device Letters. 30 (2009) 203-203. doi:10.1109/led.2009.2013300.
[127] M. Gautam, A. Jayatissa, Adsorption kinetics of ammonia sensing by graphene films decorated with platinum nanoparticles, Journal Of Applied Physics. 111 (2012) 094317. doi:10.1063/1.4714552.
[128] F. Schedin, A. Geim, S. Morozov, E. Hill, P. Blake, M. Katsnelson et al., Detection of individual gas molecules adsorbed on graphene, Nature Materials. 6 (2007) 652-655. doi:10.1038/nmat1967.
[129] R. Smith, J. Matthiesen, B. Kay, Desorption Kinetics of Methanol, Ethanol, and Water from Graphene, The Journal Of Physical Chemistry A. 118 (2014) 8242-8250. doi:10.1021/jp501038z.
[130] E. Schröder, Methanol Adsorption on Graphene, Journal Of Nanomaterials. 2013 (2013) 1-6. doi:10.1155/2013/871706.
[131] H. Romero, P. Joshi, A. Gupta, H. Gutierrez, M. Cole, S. Tadigadapa et al., Adsorption of ammonia on graphene, Nanotechnology. 20 (2009) 245501. doi:10.1088/0957-4484/20/24/245501.
[132] M. Gautam, A. Jayatissa, Adsorption kinetics of ammonia sensing by graphene films decorated with platinum nanoparticles, Journal Of Applied Physics. 111 (2012) 094317. doi:10.1063/1.4714552.
[133] L. Vicarelli, S. Heerema, C. Dekker, H. Zandbergen, Controlling Defects in Graphene for Optimizing the Electrical Properties of Graphene Nanodevices, ACS Nano. 9 (2015) 3428-3435. doi:10.1021/acsnano.5b01762.
[134] K. Yoon, A. Rahnamoun, J. Swett, V. Iberi, D. Cullen, I. Vlassiouk et al., Atomistic-Scale Simulations of Defect Formation in Graphene under Noble Gas Ion Irradiation, ACS Nano. 10 (2016) 8376-8384. doi:10.1021/acsnano.6b03036.
[135] J. Chen, W. Cullen, C. Jang, M. Fuhrer, E. Williams, Defect Scattering in Graphene, Physical Review Letters. 102 (2009). doi:10.1103/physrevlett.102.236805.
[136] Z. Cheng, Q. Li, Z. Li, Q. Zhou, Y. Fang, Suspended Graphene Sensors with Improved Signal and Reduced Noise, Nano Letters. 10 (2010) 1864-1868. doi:10.1021/nl100633g.
[137] B. Kumar, K. Min, M. Bashirzadeh, A. Farimani, M. Bae, D. Estrada et al., The Role of External Defects in Chemical Sensing of Graphene Field-Effect

Transistors, Nano Letters. 13 (2013) 1962-1968. doi:10.1021/nl304734g.
[138] K. Nemade, S. Waghuley, Role of defects concentration on optical and carbon dioxide gas sensing properties of Sb2O3/graphene composites, Optical Materials. 36 (2014) 712-716. doi:10.1016/j.optmat.2013.11.024.
[139] J. Chang, Y. Liu, and L. Lin, "Direct-write n- and p-type graphene channel FETs", 2013 IEEE 26th International Conference on Micro Electro Mechanical Systems (MEMS), pp.201,204, 20-24 Jan. 2013.
[140] R. Gorbachev, "Conductance of p-n-p Graphene Structures with "Air-Bridge" Top Gates" Nano Lett., 2008, 8 (7), pp 1995–1999
[141] H. Wang, "Hysteresis of Electronic Transport in Graphene Transistors", ACS Nano, 2010, 4 (12), pp 7221–7228
[142] F. Xia, D. B. Farmer, Y. M. Lin, and P. Avouris, "Graphene field-effect transistors with high on/off current ratio and large transport band gap at room temperature," Nano Lett, vol. 10, pp. 715-8, Feb 10, 2010.
[143] X. Yang, "Triple-Mode Single-Transistor Graphene Amplifier and Its Applications", ACS Nano, 4 (10), 5532-5538, 2010.
[144] H.Wang, A. Hsu, J. Wu,J. Kong, and T. Palacios, "Graphene-Based Ambipolar RF Mixers," Electron Device Letters, IEEE , vol.31, no.9, pp.906,908, Sept. 2010.
[145] AF Young, P Kim, "Quantum interference and Klein tunneling in graphene heterojunctions" Nature Physics, VOL 5, 222-226, 2009.
[146] M. Friedemann, M. Woszczyna, and F. Versatile "Sputtering technology for Al2O3 gate insulators on graphene" Sci. Technol. Adv. Mater. 13, 025007, 2012.
[147] D. Sun, C. Chang, S. Li, and L. Lin, "Near-Field Electrospinning," Nano Lett, vol. 6, pp. 839-842, 2006/04/01, 2006.
[148] Liang et.al."Toward Clean and Crackless Transfer of Graphene", ACS Nano, 5 (11), pp 9144–9153, 2011.
[149] J. Chang, Y. Liu, and L. Lin, "Direct-write n- and p-type graphene channel FETs," 2013 IEEE 26th International Conference on Micro Electro Mechanical Systems (MEMS), pp.201,204, 20-24 Jan. 2013.
[150] S. Kim, J. Nah, I. Jo, D. Shahrjerdi, L. Colombo, Z. Yao, E. Tutuc, and S. Banerjee, "Realization of a High Mobility Dual-gated Graphene Field Effect Transistor with Al2O3 Dielectric", Appl. Phys. Lett. 94, 062107, 2009.
[151] H. Tsuyuki, S. Sakamoto, and M. Tomiya, "Electron Transfer on Impurity doped Graphene Nanoribbon" J. Phys.: Conf. Ser. 402, 012016, 2012.